

2-19-2021 9:30 AM

## Experimental simulation of a density-driven downburst translating within a turbulent boundary layer

Shivani Ashitkumar Jariwala, *The University of Western Ontario*

Supervisor: Savory, Eric, *The University of Western Ontario*

A thesis submitted in partial fulfillment of the requirements for the Master of Engineering Science degree in Mechanical and Materials Engineering

© Shivani Ashitkumar Jariwala 2021

Follow this and additional works at: <https://ir.lib.uwo.ca/etd>



Part of the [Other Mechanical Engineering Commons](#)

---

### Recommended Citation

Jariwala, Shivani Ashitkumar, "Experimental simulation of a density-driven downburst translating within a turbulent boundary layer" (2021). *Electronic Thesis and Dissertation Repository*. 7656.  
<https://ir.lib.uwo.ca/etd/7656>

This Dissertation/Thesis is brought to you for free and open access by Scholarship@Western. It has been accepted for inclusion in Electronic Thesis and Dissertation Repository by an authorized administrator of Scholarship@Western. For more information, please contact [wlsadmin@uwo.ca](mailto:wlsadmin@uwo.ca).

## Abstract

Downburst outflows emerging from thunderstorm producing clouds are contained within the atmosphere where the outflow interacts with the preexisting atmospheric boundary layer (*ABL*). This novel study employs a realistic approach for experimental simulation of downbursts by translating the downburst source within a scaled *ABL* within a hydraulic flume system that produces open channel flow. The density-driven model approach is used, involving an iris operated cylinder release mechanism translating inside the *ABL* generated over a restrictive fetch using passive turbulence generating devices at model scales of 1:5500 and 1:10,000. The velocity vector fields across a vertical plane revealed asymmetrical outflows generated from the complex interaction of the downburst outflow with the *ABL*. Also, peak velocities as high as 26.2 *m/s* at full-scale were observed at the downstream side of the outflow after touchdown. A lower cylinder release height and higher *ABL* flow speed generated larger magnitudes of peak velocity at the downstream end of the outflow.

## Keywords

Density-driven downbursts, Travelling downbursts, Downburst *ABL* interaction, Microbursts, Atmospheric boundary layer, passive turbulence generating devices, Particle image velocimetry, Hydraulic flume, Open channel flow

## Summary for Lay Audience

A downburst is a natural phenomenon occurring within the atmosphere wherein a heavy mass of air column descends from clouds during a thunderstorm which after reaching ground causes destructive near ground winds. The wind flow observed in the atmosphere and near ground is a part of a stratified(layered) boundary layer occurring over Earth's surface where the wind speed increases starting from earth's surface to the atmosphere, and since the downburst producing cloud is surrounded by winds the cloud translates with nearly the same speed as the atmospheric winds around it. Hence, it can be conceptualized that as the downbursts starts falling from its parent cloud the wind flowing around it will force the downflow to move in one prominent direction causing the downburst outflow to grow in the direction same as that of the surrounding winds. This realistic concept of downburst is applied in the present study by generating this event at a smaller scale experimentally by first creating the wind profile observed in the atmosphere known as atmospheric boundary layer (*ABL*) in an open-channel flow system. The wind speeds are computed using Particle image velocimetry (*PIV*) technique which involves tracking of suspended particles in the flow by illuminating them using lasers. The downburst is modelled using two fluids of different densities, where the dense fluid resembles the dense air mass from the cloud and the lighter fluid resembles the atmospheric air and is used to generate the *ABL*. The dense fluid is filled inside a cylinder mechanism with iris gates at the top and bottom walls which are opened to initiate the downburst event and translated inside the generated *ABL* at a certain height. The outcomes of this study are 1) the downburst outflow moving in the same direction as the background wind generated stronger wind speeds 2) the interaction of the downburst outflow with *ABL* created asymmetrical outflows 3) increasing the background wind speed maximized the peak winds observed in the downburst near ground 4) comparison of two release heights revealed the smaller release height generated stronger winds.

## Impact of COVID-19 pandemic on this research study

This research study was affected by the COVID-19 pandemic and provincial lockdowns in Ontario. Because of sudden campus closures the ongoing experimental work came to a halt. The experimental data that was collected served half of the scope of the research study, and a significant part of the scope was not able to be worked on experimentally.

## Acknowledgments

Firstly, I would like to express my sincere gratitude to my supervisor Dr. Eric Savory, who has been very supportive throughout the completion of the thesis with his patience, valuable knowledge, and constant encouragement throughout the course of my MEng. Program. I would also like to thank my thesis advisory committee member Dr. Chao Zhang.

I would also like to acknowledge the support, I received from my colleagues in the Advanced Fluid Mechanics Group. They have been very supportive throughout my research progression and always been available for discussion. I am also grateful to Kyle Graat and Dwaipayan Sarkar who have helped me in running the experiments in lab. I would like to thank Kyle Graat for all the help and feedback on the analysis part of the downburst section of this thesis.

I would also like to thank Ron Struke and Trent Steensma from the electronics shop and Dan Sweiger from the UMS for their insight and help at different stages of this project.

I would also like to acknowledge the financial support I received from the department of Mechanical and Materials Engineering at Western University and Natural Sciences Engineering Research council discovery (NSERC) grants. I would also like to appreciate the support I received from the Society of Graduate Students (SOGS) at Western.

I am grateful to my parents Anjali Jariwala and Asit Jariwala who always have been inspiring and supporting me at all times, and their cheerful approach towards life has helped me in staying motivated while overcoming challenges. I would like to express my deepest gratitude to my brother Kedar Jariwala for believing in me and constantly motivating me. I would also like to express my deepest gratitude to my grandmother Aruna Bhavsar, my grandaunt Subhadra Bhavsar, and to all my relatives for their exceptional love and care. Without everyone's mental support and constant encouragement, it would not have been possible for me to finish this work.

# Table of Contents

Abstract .....	i
Summary for Lay Audience.....	ii
Impact of COVID-19 pandemic on this research study.....	iii
Acknowledgments.....	iv
Table of Contents .....	v
List of Tables .....	viii
List of Figures .....	ix
List of Appendices .....	xiii
Nomenclature .....	xiv
Chapter 1 .....	1
1 Introduction .....	1
1.1 Atmospheric boundary layer.....	4
1.2 Motivation.....	7
1.3 Objectives .....	9
1.4 Methodology .....	9
1.5 Scope.....	10
1.6 Thesis Organization .....	10
1.7 Summary .....	11
Chapter 2.....	12
2 Literature Review .....	12
2.1 Field Studies.....	12
2.2 Impinging jet (IJ) model .....	17
2.3 Full cloud model .....	21

2.4	Cooling source (CS) model.....	22
2.5	Density-driven model.....	23
2.6	Conclusions and Motivations.....	28
Chapter 3.....		29
3	Experimental Methodology.....	29
3.1	Density-driven downburst model.....	29
3.2	Selection of dense and ambient fluid.....	29
3.3	Hydraulic flume .....	31
3.4	Release cylinder .....	33
3.5	Traverse system .....	35
3.6	Generation of atmospheric boundary layer at model scale:.....	35
3.7	Experimental parameters .....	39
3.8	Experimental procedure .....	40
3.9	Particle Image velocimetry (PIV) .....	41
3.10	Summary .....	47
Chapter 4.....		48
4	Results and discussions .....	48
4.1	Simulation of atmospheric boundary layer in hydraulic flume .....	48
4.1.1	Boundary layer characteristics .....	48
4.1.2	Turbulence characteristics .....	51
4.1.3	Comparison with full-scale data .....	57
4.2	Travelling downburst.....	62
4.2.1	Velocity vector fields of travelling downbursts.....	62
4.2.2	Vorticity fields of the travelling downbursts outflows .....	68
4.2.3	Peak Velocity characteristics .....	74

4.2.4	Comparison of the peak radial velocities at the downstream side (DS): ..	76
4.2.5	Comparison of the peak radial velocities at the upstream side (US): .....	77
4.2.6	Comparison with stationary downburst release experiment .....	80
4.2.7	Peak wind speeds at full-scale and comparison with previous studies and field data.....	82
4.3	Summary:.....	86
Chapter 5	.....	87
5	Conclusions and recommendations.....	87
5.1	Conclusions.....	87
5.2	Contributions.....	88
5.3	Limitations and Challenges.....	88
5.4	Future Recommendations: .....	89
References	.....	90
Appendices	.....	99
Curriculum Vitae	.....	109



## List of Tables

Table 2-1 Characteristics of Microbursts recorded in <i>JAWS</i> (adapted from Hjelmfelt, 1988) .....	14
Table 3-1 Physical properties of the ambient and dense solution pair .....	30
Table 3-2 Details of experimental runs for boundary layer case for <i>ABL</i> flows. ....	39
Table 3-3 Details of experimental runs for downburst release experiments .....	39
Table 3-4 Fluid mechanical properties for various <i>PIV</i> seeding particles .....	41
Table 4-1 Boundary layer characteristics for the <i>ABL</i> simulation.....	49
Table 4-2 Aerodynamic roughness parameters obtained by fitting procedure using the log-law equation.....	50
Table 4-3 Comparison of the roughness parameters at full-scale obtained by using the selected model-scale factors. ....	59
Table 4-4 Outflow parameters at touchdown depicting the effect of the flow variables on the downburst column.....	66
Table 4-5 Peak radial velocity characteristics for travelling downburst.....	75
Table 4-6 Peak radial velocity characteristics for travelling downburst compared against the stationary downburst event .....	81
Table 4-7 Full scale values of Lundgren scaling parameters representing the travelling downburst simulation in present work.....	83

## List of Figures

Figure 1.1 Graphical representation of a downburst forming a vortex ring (adapted from Encyclopædia Britannica, Inc.).....	1
Figure 1.2 (a) sense of air motion indicated by arrows of a dry microburst over southern Kansas on May 31, 1994 captured from NOAA P-3 aircraft. (b) a downburst event in Oklahoma City, Oklahoma on July 26, 1978 producing horizontal vortex. (adapted from Bluestein 2013). .....	2
Figure 1.3 Atmospheric boundary layer profiles (a) wind velocity profile; (b) wind direction profile (adapted from Taylor, 1914). .....	5
Figure 1.4 Deviation of flight path of an aircraft due to the influence of downburst outflow (adapted from <a href="http://www.weather.gov">www.weather.gov</a> ). .....	7
Figure 1.5 Failure of power transmission tower in Argentina due to HIW events. (adapted Dempsey & White, 1996). .....	8
Figure 2.1 Evolution of a downburst recorded by the JAWS field study (adapted from Wilson <i>et al.</i> , 1984; Hjelmfelt, 1988) .....	13
Figure 2.2 Schematic of parameters defining a downburst outflow (adapted from Hjelmfelt, 1988). .....	14
Figure 2.3 Velocity field of a traveling downburst recorded by Doppler radar during <i>NIMROD</i> project. (a) doppler velocities of a travelling downburst gust (b) vertical velocity distribution of the outflow decreasing gradually with altitude (adapted from Fujita, 1981). .....	15
Figure 2.4 Microburst outflow simulator using steady jet approach at Wind Simulation and Testing (WiST) lab (adapted from Zhang <i>et al.</i> , 2013). .....	18

Figure 2.5 Velocity profiles for the steady jet model at the location of maximum velocity compared with field study results (adapted from Wood <i>et al.</i> , 2001).....	18
Figure 2.6 Experimental arrangement of density-driven downbursts with dimensional parameters (adapted from Lundgren <i>et al.</i> , 1992, Alahyari and Longmire, 1995). .....	25
Figure 3.1 Schematic diagram of the hydraulic flume system a) 3-D view; b) 2-D view (adapted from Babaei, 2018; published with author's permission) .....	32
Figure 3.2 Downburst release cylinders, a) sectional view of the release cylinder b) closed position; c) open position (adapted from Babaei, 2018; published with author's permission).....	34
Figure 3.3 Traverse system mounted over the flume side walls containing the release cylinder mounting component .....	35
Figure 3.4 Setup of turbulence mixing devices over the flume bed to generate <i>ABL</i> flows. ....	37
Figure 3.5 A schematic of arrangement of the roughness configuration at the inlet of the flume to generate <i>ABL</i> flows.....	38
Figure 3.6 <i>PIV</i> measurement system and the measurement plane displayed in the flume section (A: <i>PIV</i> Laser Unit, B: <i>PIV</i> Camera, C: Laser power units, D: Synchronizer, E: Computer system, F: Laser sheet optics, G: Laser sheet, H: Measurement plane, I: Flume section. ....	43
Figure 3.7 A representation of the sequential <i>PIV</i> data capturing process for n number of samples with $\Delta t$ as the time gap between Frame A and Frame B, and $\Delta t_s$ as the sampling time between subsequent image pair. ....	44
Figure 3.8 a) an overlap (50%) of interrogation spots created by offset (grey gridlines) over the original grid (black gridlines); b) the vectors interpolated at 9 locations by grid offset used to deform the search area in Frame B (adapted from Thielicke <i>et al.</i> , 2014). 46	

Figure 3.9 Surface plot displaying the correlation matrix showing a distinct peak for the displacement in pixels in X and Y direction. ....	46
Figure 4.1 Spatially averaged streamwise turbulence intensities in the flume measurement section .....	52
Figure 4.2 Turbulence intensities in streamwise and vertical direction scaled using outer layer (a &c) and inner layer (b & d) scaling. ....	54
Figure 4.3 Convergence of autocorrelation function for computing the integral time scales. ....	55
Figure 4.4 Comparison of non-dimensional spectral energy plots with full-scale ESDU data (design curve) where the integral length scales are defined by: a) temporal autocorrelation b) fit to ESDU curve. ....	56
Figure 4.5 Variation of spatially averaged integral length scales with wall normal distance. ....	57
Figure 4.6 Mean velocity (a) and turbulence characteristics (b, c, &d) for the upscaled boundary layer compared against ESDU profiles.....	61
Figure 4.7 Schematic showing the orientation of the <i>PIV</i> measurement plane relative to the release cylinder along with the reference origin used for the downburst cases a) For cases DB-1-A/B ; b) For cases DB-2-A/B .....	64
Figure 4.8 Velocity vector fields and contour plots for a) stationary downburst (Graat,2020) b) DB-1-B at $t/T_0 = 5.40$ .....	65
Figure 4.9 Contours of $\lambda_2$ criterion plotted with scaled velocity vectors at touchdown $t/T_0 = 2.43$ for DB-1-A .....	67
Figure 4.10 Definition of the vortex core using local maximum negative value of $\lambda_2$ criterion for DB-1-A .....	70

Figure 4.11 Trajectory of the primary vortex core in spatial domain during its evolution in time at the <i>DS</i> .....	71
Figure 4.12 Temporal evolution of the height of the vortex core ( $y_c$ ) at <i>DS</i> .....	71
Figure 4.13 Trajectory of the primary vortex core in spatial domain during its evolution in time at the <i>US</i> .....	72
Figure 4.14 Temporal evolution of the height of the vortex core ( $y_c$ ) at the <i>US</i> .....	72
Figure 4.15 Evolution of horizontal separation distance between the primary vortex core centers at the <i>DS</i> and <i>US</i> .....	73
Figure 4.16 Peak horizontal velocity profiles for the <i>DS</i> and the <i>US</i> side of the downburst outflow normalized using Lundgren scaling parameters .....	75
Figure 4.17 Instantaneous peak horizontal velocity profiles for the downburst outflows at the downstream side normalized using the maximum values a) distinct runs b) averaged for two runs .....	78
Figure 4.18 Enveloped peak horizontal velocity profiles for the downburst outflows at the downstream side normalized using the maximum values a) distinct runs b) averaged for two runs.....	79
Figure 4.19 Instantaneous peak horizontal velocity profiles for the downburst outflows at the upstream side normalized using the maximum values a) distinct runs b) averaged for two runs.....	80
Figure 4.20 Vertical profile of peak radial velocity employing cylinder diameter scaling .....	84
Figure 4.21 Vertical profile of peak radial velocity normalized by corresponding peak quantities .....	85
Figure 4.22 Radial velocity profiles scaled using Lundgren Scaling parameters and compared against Cooling source model .....	85

## List of Appendices

Appendix A: Design of ABL simulation .....	99
Appendix B: ABL experiments: Convergence of statistics, velocity vector fields, Boundary layer profile .....	102
Appendix C: Experimental uncertainty.....	104
Appendix D: Extraction of roughness parameters by fitting log-law to velocity profiles.....	105
Appendix E: Downburst experiments: Comparison of boundary layer before downburst event, Repeatability of the outflows.....	107

## Nomenclature

$A_0$	Total lot area for the roughness array ( $m^2$ )
$A_p$	Plan area covered by the roughness array ( $m^2$ )
$c_f$	Local skin friction coefficient
$d_0$	Displacement height ( $m$ )
$d_{0f}$	Displacement height at full-scale ( $m$ )
$d_p$	Mean diameter of the seed particles ( $\mu m$ )
$\delta$	Boundary layer thickness ( $m$ )
$\delta^*$	Displacement thickness ( $m$ )
$\Delta\rho$	Absolute density difference between dense and ambient fluid ( $kg/m^3$ )
$\Delta\mu$	Absolute difference between dynamic viscosity of dense and ambient fluid ( $mPa.s$ )
$\Delta n$	Difference in refractive index
$\Delta t$	Time gap between a PIV image pair ( $\mu s$ )
$H$	Shape factor
$H_0$	Release height ( $m$ )
$\kappa$	Von-Kármán constant
$k$	Height of roughness elements ( $m$ )

$L_c$	Length of contraction part of inlet chamber ( $m$ )
$L_u$	Integral length scales in streamwise direction ( $m$ )
$\lambda_p$	Plan area density of the roughness array
$\mu_a$	Dynamic viscosity of ambient fluid (glycerol solution) ( $mPa.s$ )
$\nu$	Kinematic viscosity ( $m^2 / s$ )
$Q_c$	Volume of dense fluid filled in the release cylinder for experiments ( $m^3$ )
$Q_p$	Pump flow rate ( $L/s$ )
$\rho_a$	Density of ambient fluid (glycerol solution) ( $kg/m^3$ )
$\rho_p$	Density of seeding particles ( $g / cm^3$ )
$Re_*$	Roughness Reynolds number
$Re_k$	Roughness Reynolds number based on $u_k$
$Re_\theta$	Momentum thickness Reynolds number
$Re_x$	Reynolds number
$R_0$	Scaling radius for the downburst release experiment ( $m$ )
$S$	Model scale factor
$t$	Time since the release cylinder is fully open ( $s$ )
$t_{td}$	Touchdown time of downburst downdraft ( $s$ )



$t_s$	Sampling time for PIV experiment ( $s$ )
$TI_u$	Turbulence intensity in streamwise direction
$T_0$	Lundgren time scale ( $s$ )
$\theta$	Momentum thickness ( $m$ )
$u, v$	Instantaneous velocity in streamwise ( $x$ ) and normal direction ( $y$ ) ( $m/s$ )
$u', v'$	Fluctuating velocity in streamwise ( $x$ ) and normal direction ( $y$ ) ( $m/s$ )
$u_k$	Velocity at distance 'k' in laminar boundary layer ( $m/s$ )
$u_r$	Radial velocity in $x$ direction ( $m/s$ )
$u_{r,p}$	Peak radial velocity in $x$ direction ( $m/s$ )
$u_*$	Friction velocity ( $m/s$ )
$U$	Mean velocity ( $m/s$ )
$U_a$	Free stream velocity for smooth wall case ( $m/s$ )
$U_{cyl}$	Release cylinder translation speed ( $m/s$ )
$U_g$	Free-settling velocity of the seeding particles ( $m/s$ )
$U_\infty$	Free stream velocity ( $m/s$ )
$V$	Velocity magnitude ( $m/s$ )
$V_0$	Characteristic velocity scale (Lundgren scaling) ( $m/s$ )

$W$	Horizontal distance between downstream and upstream vortex centers ( $m$ )
$x$	Distance from flume inlet ( $m$ )
$x_c$	Distance from cylinder release location ( $m$ )
$x_L$	Distance from the point where contraction chamber starts in the streamwise direction ( $m$ )
$x_p$	$x$ -location of peak velocity from cylinder center at release ( $m$ )
$x_{td}$	Touchdown location referenced at the cylinder release location ( $m$ )
$y$	Distance from bottom wall of flume in normal direction ( $m$ )
$y_c$	Distance from bottom wall of flume in normal direction for downburst events( $m$ )
$y_L$	Distance from the point where contraction chamber starts normal to the streamwise direction ( $m$ )
$y_p$	$y$ -location of peak velocity from bottom wall ( $m$ )
$Y^+ = \frac{yu_*}{\nu}$	Normalized wall normal distance
$z$	Distance from ground at full scale ( $m$ )
$z_0$	Roughness length ( $m$ )
$z_{0f}$	Roughness length at full scale ( $m$ )

## Abbreviations

<i>ABL</i>	Atmospheric Boundary Layer
<i>AGL</i>	Above Ground Level
<i>DCC</i>	Direct Cross Correlation
<i>DFT</i>	Discrete Fourier Transform
<i>DS</i>	Downstream Side
<i>JAWS</i>	Joint Airport Weather Studies
<i>MIST</i>	Microburst and Severe Thunderstorms
<i>NIMROD</i>	Northern Illinois Meteorological Research on Downburst
<i>PAM</i>	Portable Automated Mesonet
<i>PIV</i>	Particle Image Velocimetry
<i>PLIF</i>	Planar Laser Induced Fluorescence
<i>RADAR</i>	Radio Detection and Ranging
<i>US</i>	Upstream Side

## Chapter 1

### 1 Introduction

The phenomenon of a downburst was first identified in 1974 when Fujita observed a strange starburst pattern of fallen trees while conducting an aerial survey of the damage from the tornado events in Beckley, West Virginia, United States (Fujita, 1985). These starburst patterns were distinctly different from the whirling patterns of objects left by the tornado winds. The aerial photographs taken by low-flying Cessna aircraft by Fujita of the damage patterns left by the windstorms in midwestern United States revealed a pattern where a shift from vertical to horizontal direction of the airflow was observed by traces of cornstalk blown in a single direction from the impingement location of the downburst (Fujita, 1985). Such investigations of damage sites from tornado events fueled the interest of Fujita and Srivastava (Fujita and Srivastava, 1977) who conducted the first downburst field program *NIMROD* (Northern Illinois Meteorological Research on Downburst) in 1978 (Fujita, 1985).

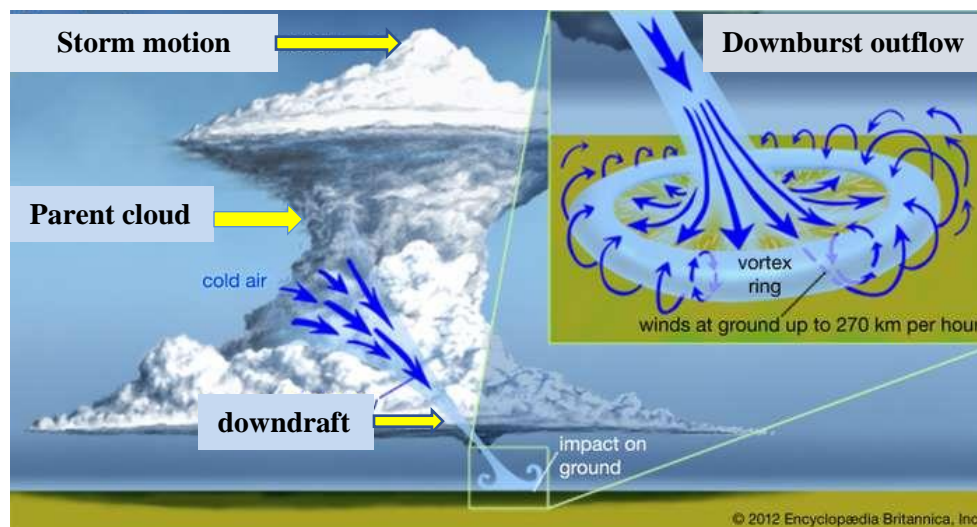


**Figure 1.1 Graphical representation of a downburst forming a vortex ring (adapted from Encyclopædia Britannica, Inc.)**

A downburst was defined by Fujita as “a strong downdraft which induces an outburst of damaging winds on or near the ground” (Fujita, 1985). The event termed a downburst

usually occurs coincidentally with thunderstorms or the formation of cumulonimbus clouds. In a downburst a dense air mass with precipitate matter descends from cumulonimbus clouds which later impinges on the ground and, thereafter, spreads radially across the ground causing very high near ground velocities. These high intensity winds close to the ground are the major cause for destruction of low-rise buildings, airplanes, power transmission lines, and vegetation (Fujita, 1985; Wolfson, 1988). These highly divergent winds can be either straight or curved depending on the parent cloud and environmental conditions (Fujita, 1985). Downbursts are formed due to various microphysical processes taking place in the atmosphere such as rapid evaporation and precipitation (Wakimoto, 1982). Later, the accumulated dense air/precipitate (the former corresponds to dry downbursts and the latter to wet downbursts) accelerates towards the ground due to gravity and causes very high intensity horizontal winds after the impingement of the downdraft takes place. During the descending stage of the downdraft, the formation of baroclinic vortex at the outflow boundary causes shear at the interface (Baroclinicity refers to the changes in density of a fluid with temperature and pressure). As the downdraft hits the ground a dominant vortex ring is formed which rolls out in the radial direction dissipating the momentum contained in it by experiencing shear from the ground surface.

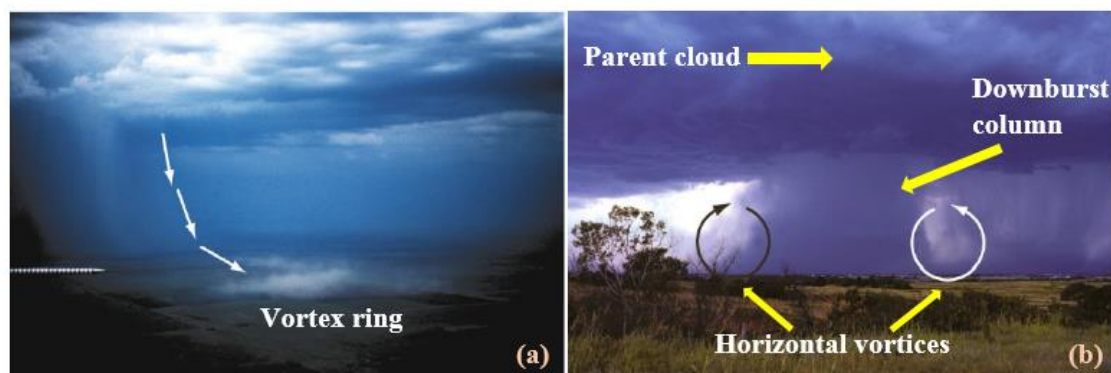


**Figure 1.2 (a) sense of air motion indicated by arrows of a dry microburst over southern Kansas on May 31, 1994 captured from NOAA P-3 aircraft. (b) a downburst event in Oklahoma City, Oklahoma on July 26, 1978 producing horizontal vortex. (adapted from Bluestein 2013).**

Downbursts are associated with high pressure conditions in the thunderstorm producing cloud cells. Rapid evaporation causing continuous updrafts of warm air leads to the formation of a large cumulonimbus cell, which later on forms the cold air mass and precipitation within it that subsequently reaches ground due to the negative buoyancy effect. The vortex structure of a downburst differs from a tornado vortex in many aspects i.e., a) the axis of rotation of the vortex is horizontal in a downburst whereas it is vertical in the latter b) downburst vortex is transient, whereas a tornado vortex is maintained for a long period of time.

Downbursts are characterized depending on the horizontal extent of the outflow as (i) Macrobursts: downburst outflow with its horizontal extent greater than 4km. (ii) Microbursts: downburst outflow with its horizontal extent equal to or less than 4km. The Macroburst often causes damage in similar amounts to tornados (F2 scale) with wind speed of about 60 *m/s* lasting for about 5-30 minutes (Fujita, 1985). The high intensity winds for a strong microburst can be as high as 75 *m/s* although their horizontal scale being smaller than that of a macroburst (Fujita, 1985). After the *NIMROD* and *JAWS* (Joint Airport Weather Studies) was conducted the field data showed evidence of dry microbursts which negated the assumption that precipitation always occurs with downburst. In dry areas the precipitate from the outflow evaporates before it reaches the ground, also high cloud base in dry area aids this process. Downbursts originating from a tornado supercell or a strong mesocyclone results in the airflow pattern having twisting streamlines whereas the irrotational microburst winds causes to form radial streamlines of the high intensity winds (Fujita, 1985).

There also have been other full-scale studies carried out in different parts of the world such as FAA/Lincoln Laboratory operational wealth studies (FLOWS) (Wolfson *et al.*, 1985), Thunderstorm Outflow Experiment (Gast and Schroeder, 2003; Orwig and Schroeder, 2007), the Thunderstorm Wind Project (Choi, 2004) to understand and characterize the nature of the wind structures that these downburst flows produce. Rapid transformation of wet microbursts into strong macroburst has been found in thunderstorms that occurred in 1984 at Memphis, TN, USA (Wolfson *et al.*, 1985).

Velocity profiles measured at the Tuas wind measuring station in 2002 at Singapore reveal that the vertical wind profiles of the thunderstorms are affected by several factors with the ground roughness, storm intensity and the measurement distance from the thunderstorm cell center being the major ones (Choi, 2004). There also has been work done to predict the microburst gust strength (WINDEX, (McCann, 1994)) and the magnitude of the strong short-lived gusts (GUSTEX, Geerts (2001)) occurring in New-South Wales, Australia to avoid the damaging wind effects to the aviation industry.

A downburst event taking place in a quiescent environment would lead to a symmetrical circular footprint of the outflow if observed from the plan view. But, in reality, there is ambient air motion in the atmosphere and the parent cloud translates with a mean wind speed relative to the ground that affects the spread of the downburst outflow and results in an asymmetrical footprint that is elliptical in shape as seen from the plan view (Fujita, 1985). The structure of the downburst outflow depends on the atmospheric boundary layer in that local region. The concept of the atmospheric boundary layer (*ABL*) is introduced in the following section in this chapter for completeness.

## 1.1 Atmospheric boundary layer

The Earth's atmosphere is stratified into several layers based on the temperature. The troposphere is the lowest layer extending up to 10-18 km above the ground (Barry & Chorley, 2010; Encyclopedia Britannica, Inc. (accessed in 2019)). The *ABL* comprises of a very small part of the troposphere close to the ground which experiences the effects from earth's surface and the diurnal thermal effects. The gradient wind at about 500-3000 m from the surface of earth is not affected by ground shear and is governed by the pressure differences present at synoptic scale (ESDU) (1993). Very close to the ground the effects due to ground friction, earth's rotation, temperature gradients, etc. influence the characteristics of the air motion. A boundary layer is formed over a surface as the fluid experiences the friction due to surface roughness causing the fluid to adhere to the roughness length with a zero velocity. As the distance from the ground increases, the velocity profile is seen to increase logarithmically (as represented in equation 1.1) reaching the free stream velocity outside the boundary layer.

$$\frac{u}{u_*} = \frac{1}{\kappa} \ln \left( \frac{z - d_0}{z_o} \right) \quad (1.1)$$

where,  $u$  = wind velocity at height ‘ $h$ ’;  $u_*$  = friction velocity ;  $\kappa$  = Von Karman’s constant;  $z$  = distance above ground;  $z_o$  = aerodynamic roughness length ;  $d_0$  = zero-plane displacement height

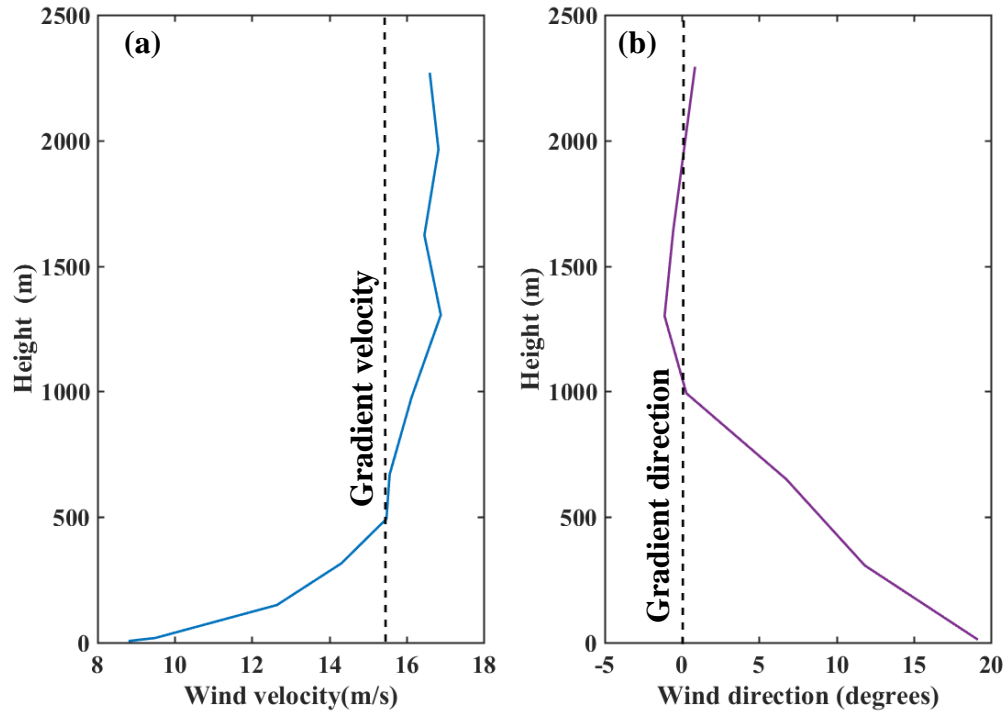


**Figure 1.3 Atmospheric boundary layer profiles (a) wind velocity profile; (b) wind direction profile (adapted from Taylor, 1914).**

The thickness of the *ABL* (500-1000m) is variable depending on the shear conditions at the ground, Coriolis force, and the atmospheric stability (Kaimal & Finnigan, 1994; Counihan, 1975). For wind velocities greater than 10 *m/s* the *ABL* can be considered adiabatic as the turbulence generated by surface shear dominates that produced turbulence from thermal perturbations (Cook, 1977). The *ABL* can be divided into segments depending upon the influence from external factors that affects the wind structure. The surface layer is the lowermost part of the *ABL* (about 50-100 m deep) where the structure of the wind depends on surface friction and vertical temperature



gradients, with the vertical shear stress almost constant and not influenced by the rotation of earth. Moreover, in the region up to the height from about 500-1000 m the wind profile is influenced by rotation of earth (Coriolis force) in addition to the factors affecting the surface layer. (Kaimal & Finnigan, 1994).

In the real downburst event, the thunderstorm cloud is translating with the ambient air motion with the velocity of the order of the gradient wind outside the boundary layer. Before the downburst event commences there is a well-established *ABL* over the terrain with a certain depth. At the start of the downburst event the translating cell of the parent cloud generates the outflow of the dense air mass which descends towards the ground, thus interacting with the existing *ABL*.

In a downburst event the density difference between the precipitate from the parent cloud and the ambient air is the driving force for the phenomenon to occur, and as is discussed in chapter , a similar idea is used for the present work to replicate the event at a model scale. The density difference model of downburst was first implemented using saltwater and water, the former being the dense fluid and the latter the ambient fluid (Lundgren *et al.*, 1992). Later, (Alahyari *et al* 's (Alahyari *et al.*, 1995) research successfully proposed the glycerol (ambient) and potassium phosphate (dense) aqueous solutions as suitable working fluids by matching their refractive indexes and then analyzing the velocity vector field of the downburst outflow using Particle Image Velocimetry (*PIV*) (Alahyari *et al.*, 1995). In all these studies a cylinder release mechanism for holding the dense fluid was designed and its feasibility to simulate downburst event was tested (elaborated further in Chapter2).

## 1.2 Motivation

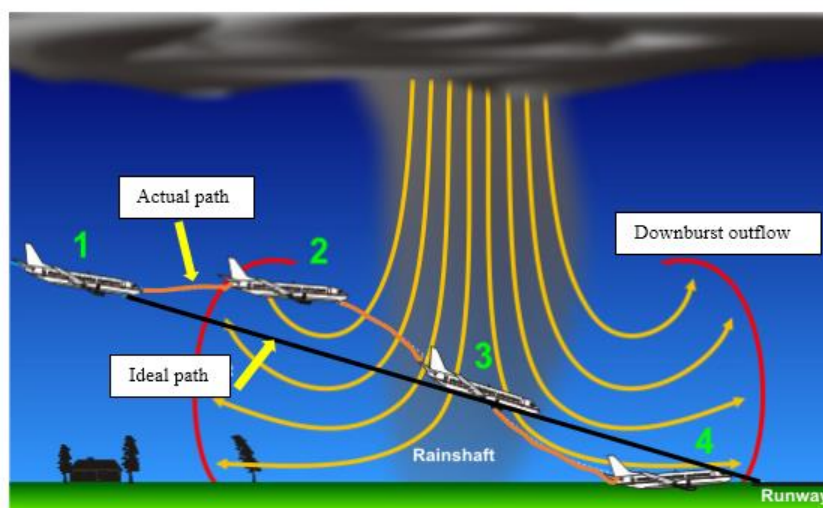


**Figure 1.4 Deviation of flight path of an aircraft due to the influence of downburst outflow (adapted from [www.weather.gov](http://www.weather.gov)).**

Many airplane crash incidents recorded in history are due to downbursts, which went unforeseen by the low-level wind shear alert systems due to the highly transient nature of the event, were brought to the attention of researchers who then studied the cause of these diverging winds (Fujita, 1985). An airplane entering the downburst outflow while trying to maintain its glideslope path when taking off or landing experiences deviations in the lift force depending on its direction of approach inside the downburst outflow (Fujita, 1985). The aircraft crash incidents were the prime reason for the early studies on downburst outflows. However, recent developments in the Microburst Wind Potential Index (*MWPI*) algorithms applied to measurements from remote sensing techniques such as *RADAR* (Radio detection and Ranging), *LIDAR* (Light detection and Ranging), and *GOES* (Geostationary Operational Environmental Satellite) allows forecasting of these events that cause high intensity winds (*HIW*) to prevent aviation hazards by giving prior downburst alerts. (Wolfson *et al.*, 1994; Nechaj *et al.*, 2019; Pryor, 2015).

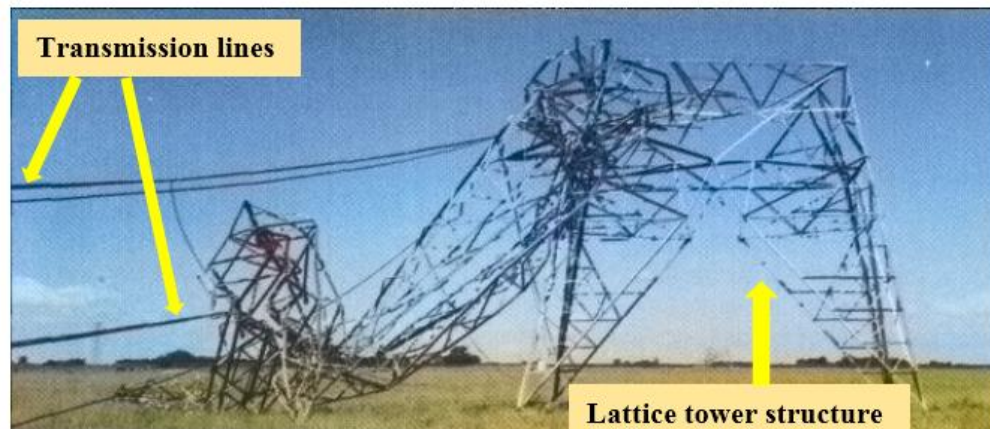


**Figure 1.5 Failure of power transmission tower in Argentine due to HIW events. (adapted Dempsey & White, 1996).**

Downburst winds are a potential hazard to electricity transmission lines and building structures, causing economic and social damage. Events of the failure of electricity transmission towers due to *HIW* produced from downbursts are evident in history such as the failure of transmission towers in Manitoba, Canada (McCarthy & Melsness, 1996), and the failure of 23 transmission towers during a thunderstorm in South Australia (Australian Wind Alliance, 2016). The cause of these failures is that the design codes for such structures that only accommodate the wind loads from synoptic wind events (Savory *et al.*, 2001). Hence, to prevent such catastrophic events more robust design considerations seem imperative which directly rely on the structure and characteristics of the downburst outflow event and, to achieve this, understanding downburst wind profile in a realistic environment sets a precursor. Research studies analyzing the response of transmission line conductors and towers in the downburst wind loads have been conducted to analyze the failure modes of the transmission towers and lines. Savory *et al.* (2001) had paved the way for a more detailed parametric study on transmission towers characterizing the effects of the scale and intensity of the high intensity winds. Aboshosha & Damatty (2015) had found that the maximum contribution of the resonant component is low (in the order of 6%) for the multiple-spanned system at different wind velocities for both downburst and synoptic winds. For the single-spanned system, however, the resonant component shows a relatively high maximum contribution (in the order of 16%) at low wind velocity and a low maximum contribution (in the order of 6%)

at high wind velocity for both downburst and synoptic winds. Elawady *et al.* (2017) carried out the first-aero elastic test to assess the dynamic response of the multi-span transmission line. The test results show that the resonance contribution ranges between 5% and 10% of the peak response for the tower. They also show that the dynamic response of the conductors can reach up to 30% and 12% of the peak response at low and high downburst speeds, respectively. However, these studies were limited to stationary downbursts events and, hence, a more comprehensive study on travelling downburst need to be carried out to evaluate the response of such transmission lines under such circumstances.

The current research, therefore, focuses on implementing the density-driven model to simulate travelling downbursts to understand the structure of downburst outflow and its transient characteristics in realistic ambient conditions.

### 1.3 Objectives

The primary objective of this research work is to:

- Understand the influence of the ambient shear on the outflow of single translating downburst event by analysing its velocity field and comparing it to that of a stationary downburst.

In order to achieve the aforementioned objective, the following tasks were performed:

- i. A sheared boundary layer was generated at model scale simulating the *ABL* flow over a rural/sub-urban terrain within a hydraulic flume.
- ii. A translating downburst event was simulated experimentally, using the density-driven model, within the simulated atmospheric boundary layer.

### 1.4 Methodology

In this section a brief outline of the methodology for the current work is described. A detailed description of the experimental methodology is discussed in Chapter 3. As the current study aims at understanding how the ambient shear affects the translating downburst outflow, the work can be divided in to simulating two separate parts:

- a) Atmospheric boundary layer (sheared terrain): In this work the atmospheric boundary layer at model scale is experimentally simulated within a hydraulic flume apparatus which is a closed-circuit water channel. By using passive turbulence generating elements, fence, and spires and an array of roughness elements, a developed turbulent boundary layer representing a realistic rural/suburban boundary layer is generated over a limited fetch. For measuring the velocity profile, the particle image velocimetry (*PIV*) technique is used in the study.
- b) Translating Downbursts: A novel cylinder release mechanism using iris gates that open swiftly is used to closely replicate the downburst phenomenon. Compared to a full-scale downburst event the diameter of the cylinder represents the diameter of the downburst outflow that spawns from a parent cloud and the height of the cylinder base from the ground plane of the flume fetch can be regarded as the cloud base height. A dense fluid (potassium phosphate aqueous solution) is used to fill the cylinder and, after immersing the cylinder in the ambient fluid (glycerol solution) the cylinder is translated along the flume fetch and the iris gates are opened at the start of data capturing at the measurement location.

## 1.5 Scope

The travelling downburst is experimentally modelled by matching its translational velocity with the mean free stream velocity of the ambient fluid flow. The boundary layer ( $\delta = 5.47\text{cm}/6.75\text{cm}$ ) developed over the flume fetch is determined for the corresponding free stream velocities  $6.65\text{cm/s}$  and  $3.04\text{cm/s}$ , respectively, for the experiments. The height of the downburst outflow after impingement is of comparable extent to the depth of the boundary layer. The events in this study are modelled at a model scale factor of 1:5500 and 1:10,000.

## 1.6 Thesis Organization

This thesis is written in “Monograph” format, the present chapter refers to defining a “downburst” and the “atmospheric boundary layer” and the general idea of the present

research work. In Chapter 2 a detailed literature review on downbursts is presented, along with the research gaps and the purpose of the current work.

Chapter 3 contains the experimental methodology of modelling downbursts using the density-driven approach. This chapter also contains the detailed experimental methods implemented to generate the oncoming boundary layer. The data acquisition, processing and experimental uncertainty related to the *PIV* measurement technique is explained in the chapter.

In Chapter 4 the results and discussion of the experimental work are presented, with the aim of determining how the ambient shear influences the downburst outflow.

Lastly, Chapter 5 consists of the Conclusions and Recommendations for future research which is a summary and contributions from the current work followed by proposed future work.

## 1.7 Summary

The present section summarizes the key items introduced in this chapter. Firstly, the concept of the downburst with respect to density driven flows is introduced. Next, the atmospheric boundary layer is briefly discussed which gives the reader an understanding of the interaction of the density driven downbursts with the *ABL* near to the ground. Downbursts possess a threat to airplanes during take-off and landing operation, and to electricity transmission lines which drives the motivation for the current work. The objectives, methodology and the scope of the current work are briefly discussed in this chapter which gives a preliminary orientation of the discussions presented in the subsequent chapters of the thesis.

The next chapter presents a critical review of the advancements made in the field of density-driven downbursts, along with the synthesis of the previously adopted methodologies to model this kind of flow feature in the atmosphere.

## Chapter 2

### 2 Literature Review

Downbursts are meteorological events causing very high wind shear near to the ground capable of causing damage similar to an F2 scale tornado (Fujita, 1981). As discussed in Chapter 1 (section 1.2), these high intensity winds posing a threat to building structures, power transmission lines etc. have been a challenging research problem for the wind engineering field. The outcome of studies on downbursts can be helpful for modifying building and structure codes that usually lack in accounting for downburst like winds. Hence, the prime motivation is in developing the most accurate and reliable model simulating the downburst event.

This section introduces the different approaches used to study the downburst phenomenon in the literature. It also includes the key features of downbursts flow that were revealed using various simulation methodologies. Firstly, the key findings from the meteorological data from downburst field investigations are presented, followed by the various downburst modelling approaches. A downburst closely resembles a wall jet impinging on a surface (Hjelmfelt, 1987), and this widely used modelling aspect is discussed here with its possible shortcomings. Later, the studies implementing the density-driven approach are discussed since density difference is the actual driving mechanism within a downburst. The credibility of this method is assessed and justified for its use in the present work.

#### 2.1 Field Studies

After the downburst was identified by Fujita in 1974 during an aerial survey, *NIMROD* was the first field program conducted in 1978 in Chicago, Illinois, which used 3 Doppler radars and 27 Portable Automated Mesonet (*PAM*) stations (Fujita, 1985). The aim of this project was to elucidate the understanding of the flow-field of a downburst. The general term downburst was classified, based on the horizontal extent of winds, as “macroburst” and “microburst”. During the *NIMROD* project 64% of the total observed microbursts were wet microbursts (containing precipitate in the outflow) compared to 17% in the

*JAWS* field study which was focused on studying microbursts only (Fujita, 1985). The occurrences of dry or wet microburst were found to be mainly related to the type of climate that exists in the region, where a location with deep and dry boundary layers was most often expected to experience dry downbursts (sometimes with little rain) (Wilson *et al.*, 1983). Later research into the downburst life cycle, based on the *JAWS* data, categorized the downburst based on the intensity of the outflow. The shape of the outflow of a downburst depends on the strength of the ambient flow, where weak environmental flows resulted in an “isolated” downburst, with a symmetric outflow. However, downbursts confined in strong low-level environmental flows generate “embedded” outflows with complex asymmetrical flow fields (Hjelmfelt, 1987).

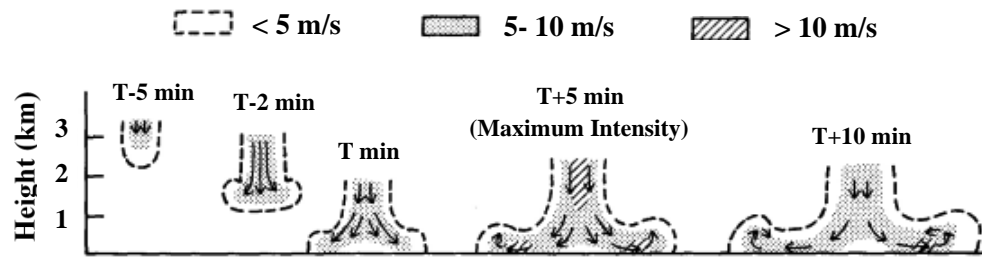


**Figure 2.1 Evolution of a downburst recorded by the JAWS field study (adapted from Wilson *et al.*, 1984; Hjelmfelt, 1988)**

The *JAWS* doppler radar data were further analyzed by researchers to study the structure of the downburst outflow and its evolution. (Wilson *et al.*, 1984; Hjelmfelt, 1988). Figure (2.1) shows that the microburst evolution starts from *T-5 min* where the downdraft is 2 km above the surface, impinging at the surface at time *T min* with a downdraft speed of about 10 m/s. At *T+5* the outflow horizontally spreads over 3.1 km compared to 1.8 km at *T min*, and later at *T+10 min* the flow weakens, spreading to about 6-8 km in area. In addition, it was also observed from the *JAWS* downburst project that, after touching the surface and reaching the maximum intensity, half of the outflows enlarged, whereas some outflows weakened entirely, with few ended up growing into outflows of larger scales (Hjelmfelt, 1988). The *JAWS* study quantitatively defined the dimensional structures of the downburst (parameters defined in figure (2.2) and summarized in table (2.1)).



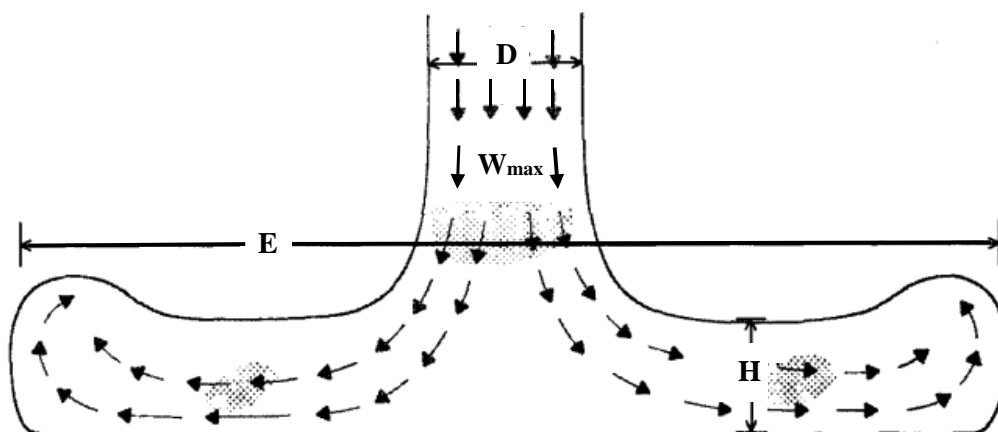


**Figure 2.2 Schematic of parameters defining a downburst outflow (adapted from Hjelmfelt, 1988).**

**Table 2-1 Characteristics of Microbursts recorded in JAWS (adapted from Hjelmfelt, 1988)**

Microburst type (Isolated or Embedded)	Embedded	Isolated	Embedded
Decay Type	Large Scale	weakened	microburst line
$H$ (depth) at maximum outflow intensity (km)	1.1	1.1	0.9
$D$ (Diameter of outflow) (km)	1.2	1.8	1.4
$E$ at maximum outflow intensity (km)	6	6.3	4.8
$W_{max}$ at $z = 1.2\text{km}$ ( $\text{ms}^{-1}$ )	6	14	9
Cloud Base (km AGL)	2.8	4.1	2.8
Surface environmental wind ( $^{\circ}\text{Az}/\text{ms}^{-1}$ )	170/7	360/3	290/6

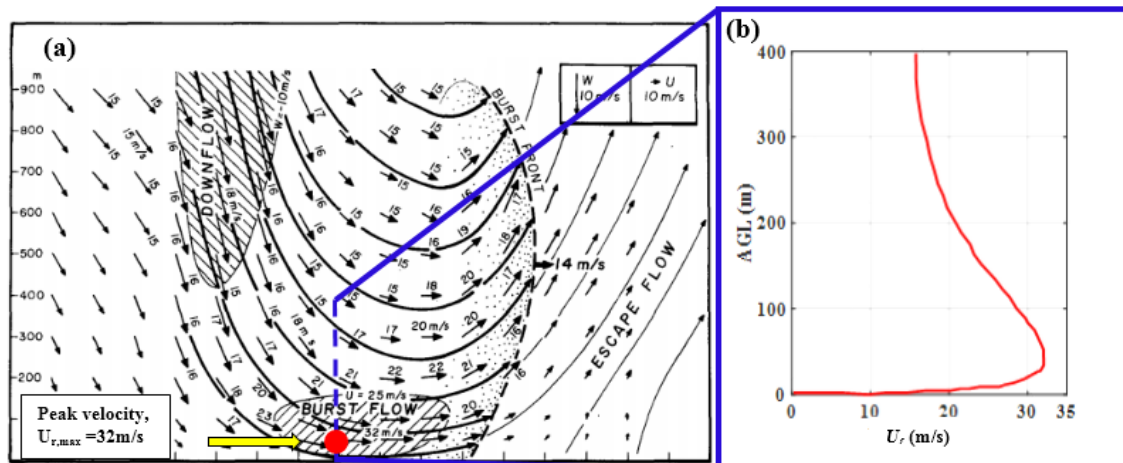


**Figure 2.3 Velocity field of a traveling downburst recorded by Doppler radar during *NIMROD* project. (a) doppler velocities of a travelling downburst gust (b) vertical velocity distribution of the outflow decreasing gradually with altitude (adapted from Fujita, 1981).**

Field observations also provided data quantifying the intensity of downburst events recorded by the measurement network (*RADAR*, *PAM*, Anemometers) during *NIMROD* and *JAWS*. Most of the windspeeds recorded were between 12-14 *m/s* having the highest frequency of occurrence for the windspeed range for both *JAWS* and *NIMROD*. It was found that the frequency of occurrence dropped in an exponential manner for both wet and dry downbursts when the windspeed reached the maximum observed windspeeds (31.3 *m/s* in *NIMROD* and 32.6 *m/s* in *JAWS*). The highest windspeed recorded during a downburst event was at Andrews AFB where an anemometer mounted at 4.9 m AGL recorded a windspeed of 67 *m/s* (Fujita, 1985). A Velocity peak of 32 *m/s* was recorded for an outflow of a travelling downburst by doppler radar during *NIMROD* project (figure (2.3)) (Fujita, 1981). The third notable field study on downburst, post *JAWS* and *NIMROD*, was conducted in Alabama in 1986 called the Microbursts and Severe Thunderstorm (*MIST*) project. The objective was to characterize downburst features in a humid environment (Fujita, 1992). The results obtained from the *MIST* project revealed the higher water content in the parent cloud is responsible for strong downdrafts in such environments. The multiparameter radar measurements from *MIST* showed the importance of frozen condensate in producing such microbursts (Srivastava 1987, Wakimoto and Bringi 1988, Proctor 1989). It was also hypothesized that such downdrafts

are usually located close to the ground that results in intense cold pools of air near the surface. Apart from there were, several other field research programs were conducted simultaneously, for example, the Classify, Locate and Avoid Shear (CLAWS) (McCarthy & Wilson, 1986); the FAA/Lincoln Laboratory operational Weather Studies (*FLAWS*) (Wolfson *et al.*, 1987); and the Convection Initiation and Downburst Experiment (CINDE) (Wilson *et al.*, 1988). Not only in USA, but downbursts have been seen to occur in other parts of the world too. Thunderstorms occurring in Okoyama, Japan (1991) recorded high-speed wind gusts in excess of 51m/s (Ohno *et al.*, 1994), the most severe downburst being the hail precipitated downburst. Similar conclusions were drawn from the downburst event recorded in Beijing, China in 2002 where the strongest downdraft was seen to be primarily produced by hail loading and rain evaporation. Choi (2004) investigated the variation of windspeeds with height during thunderstorms measured at five levels in Singapore and found that the wind profiles during thunderstorms are influenced by the thunderstorm cell center, the intensity of the storm and ground roughness. Geerts (2001) assessed wind events from 10 stations in New South Wales and Australia across data obtained for 33 years and reported minimum and maximum wind speeds of 21m/s and 42m/s, respectively. Rowcroft (2011) presented results based on more than 20 years of data acquired in the coastal areas of Australia and New Zealand, where a thunderstorm outflow has been seen to reach a maximum speed of 90m/s. Durañona *et al.*, (2006), analyzed wind velocity data from 11 extreme non-synoptic events that occurred along the Northern European coasts at various heights above the ground. It was found that the high wind events could behave in different ways depending upon the wind profile velocity with respect to time. Jarvi *et al.*, (2007) investigated thunderstorms that caused forest damage in Southern Finland. The velocities of the horizontal and vertical wind speed gusts were 22m/s and 15m/s. For the downbursts recorded in Livorno, Italy on 1<sup>st</sup> October 2012, the peak windspeeds ranged between 15-18 m/s as recorded by ultrasonic anemometers mounted 20 m above ground (Burlando *et al.*, 2017).

Although the downburst field measurements give important information regarding the evolution of downbursts and its related physical parameters, the measured data is prone to

some inaccuracies. Field studies are always reliant on doppler radar and probe measurements and, therefore, measurement of winds at low altitudes may get restricted due to ground clutter (Wilson *et al.*, 1984). The radial velocities obtained from Doppler data comprises of statistical uncertainties and the vertical component of wind is approximated by upward integration of mass continuity equation (Wilson *et al.*, 1984; Doviak *et al.*, 1976). Capturing events at smaller scale is a challenge with large distances between the measuring stations leading to insufficient temporal and spatial resolution (Eilts & Doviak, 1987). Not only this, but the high operational costs associated with downburst field research programs made researchers keen to employ other methods to study downbursts, namely physical and numerical modelling.

The next section discusses the different downburst simulation methodologies in order to highlight the strength and weakness of each of those methods.

## 2.2 Impinging jet (IJ) model

A downburst can be conceptualized as a circular jet originating from a nozzle impinging against a solid wall, the idea being that a wall jet has a visual resemblance to a downburst outflow. This widely adopted modelling technique became popular due to the simplicity and scalability of the modelling process. The jet flow can be generated easily within a laboratory using a centrifugal blower (Bakke, 1957) or using an apparatus consisting of fans inside a nozzle (Zhang *et al.*, 2013) as shown in Figure (2.4)) The wall jet flow field was first studied analytically by Glauert (1956) where the vertical profiles of the horizontal velocity within the horizontal outflow was investigated for a laminar and turbulent flow. Further experimental studies carried out by Bakke (1957), Bradshaw and Love (1959), Poreh and Cermak (1959), and Poreh *et al.*, (1967) subsequently improved the understanding of the physics governing the vertical and horizontal flow profiles. Hjelmfelt, (1988) for the first time compared the vertical profiles of the horizontal velocity of a laboratory simulated wall jet against the radial profiles of the horizontal velocity captured from the Colorado microbursts (during the JAWS project) and showed that these outflow structures resemble many features of a laboratory wall jet. The use of the IJ model to simulate the thunderstorm downbursts at a model scale was first carried

out by Wood *et al.*, (2001), where a continuous jet of air was forced to impinge on a flat solid surface. A scaling ratio between 1:1300 and 1:13000 were used to model the downbursts. The measured mean velocity profiles for the flat surface agreed well with previously published laboratory and full-scale data (Figure 2.5), but only after the expanding velocity profile had stabilized, beyond approximately 1.5 jet diameters from the center of the impinging jet. These observations were also supported by those of Chay and Letchford, (2002); Zhang *et al.*, (2013).

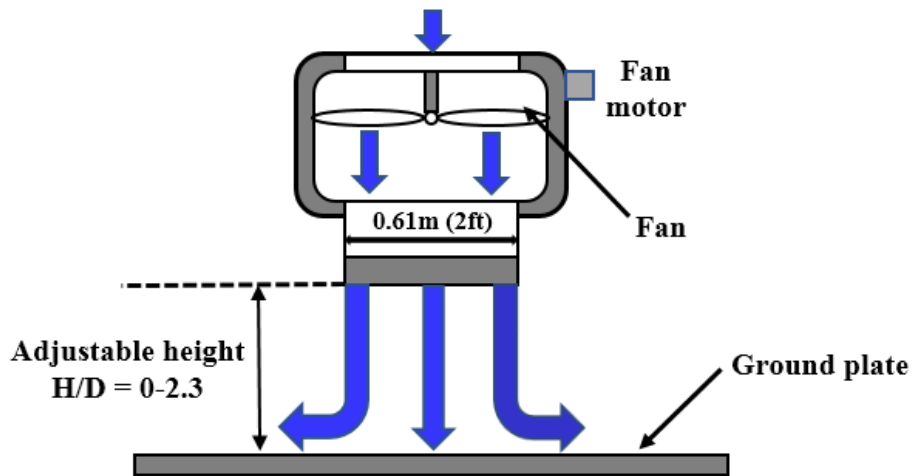


**Figure 2.4 Microburst outflow simulator using steady jet approach at Wind Simulation and Testing (WiST) lab (adapted from Zhang *et al.*, 2013).**

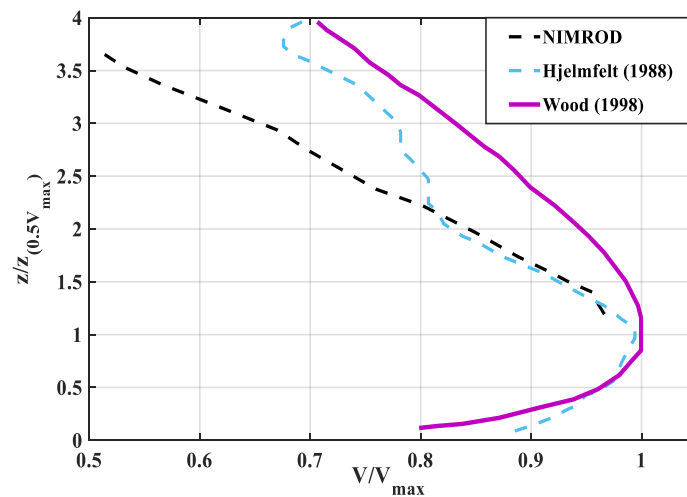


**Figure 2.5 Velocity profiles for the steady jet model at the location of maximum velocity compared with field study results (adapted from Wood *et al.*, 2001).**

Different extensions to the simplified IJ jet model have been made. Letchford and Chay (2002), Chay and Letchford (2002) modelled the effect of storm translation by having a translating jet nozzle apparatus within a wind-tunnel ('moving jet wind-tunnel model'). The apparatus was made to translate with  $1/5^{\text{th}}$  (2 m/s) and  $1/10^{\text{th}}$  (1 m/s) of the speed of the downburst outflow exiting from the nozzle. Mason *et al.*, (2005) used a pulsed wall IJ model to simulate the gust front of a thunderstorm downburst. Pulsing was achieved using an aperture positioned below the jet outlet. Hoxey *et al.*, (2003) outlined a flap controlled impinging jet arrangement, to study the behavior of the downdraft in still air conditions and in a simultaneous wind cross flow. The downburst was generated by manually opening and closing a flap which diverted air into the impinging jet. McConville *et. al.*, (2009) examined three different methods namely fan-control, sheet-control and flap control to generate the time-dependent downburst flow. The flap control mechanism was found to more suitable in predicting the horizontal velocity profiles. The influence of the jet inclination on the steady and the pulsed flow stationery impinging jets were studied by Mason *et al.*, (2005). The pulsed flow acceleration was produced by stretching a thin latex membrane across a support board positioned downstream of the nozzle.

Despite, the fact that numerous experiments involving impinging jet model have produced outflow profiles similar to downbursts, one of the main drawbacks to this approach is that the impinging jets are relatively small when compared to an actual downdraft and are limited by the laboratory scale. Moreover, the impinging jet model is driven by momentum-forcing-source instead of the buoyancy driven source (Wood *et. al.*, 2001). The models do not emphasize on the near-ground flow dynamics which is of interest in a practical scenario. Another drawback of the impinging jet type simulations relates to the transient nature of the downbursts and the drag-induced downflow which cannot be modeled with IJ approaches. The impinging jet model relies entirely upon the unrealistic forcing of an impulse jet which is not present in nature (Mason *et al.*, 2009, Anabor *et al.*, (2011), Vermeire *et al.*, (2011, 2011), Zhang *et al.*, 2013).

Lin and Savory, (2006) provided an alternative technique to the existing IJ model where they argued that the radial outflow from the downbursts can be treated separately to that of the vertical flow associated with the downdraft column. The slot jet concept was therefore employed to simulate only the outflow region of a downburst. An additional wind source was introduced through a slot located at the base the wind-tunnel. Lin *et al.*, (2007) extended this quasi-slot jet approach to investigate the time-dependent features of the outflow with an actuated gate mechanism. However, one of the modelling drawbacks of the slot jet approach is the inability to simulate the interaction of the downburst at the location where it initially strikes the ground, where there are potentially high gust velocities (McConville *et. al.*, 2009).

Numerical modelling of IJ flows employing Computational fluid dynamics (CFD) method have been carried out by many researchers (Selvam & Holmes (1992), Craft *et al.*, (1993), Wood *et. al.*, (2001), Chay *et al.*, (2005), Kim & Hangan (2007), Xu & Hangan (2008), Sengupta & Sarkar (2008), Das *et al.*, (2010), Li *et al.*, (2012)). Selvam and Holmes (1992) used a two-dimensional (2D) Reynolds averaged Navier-Stokes (RANS)  $k-\epsilon$  model to simulate a steady jet of air impinging normally on a ground plane. The density differences and the transient effects were however, ignored in the model. The performance of different two-equation eddy viscosity models in the numerical prediction of turbulent impinging jets were assessed by Craft *et al.*, (1993). The results suggested that a new-wall reflection model (second moment closure) was the most suitable prediction model. A 2-D Reynolds stress model (RSM) was used by Wood *et al.*, (2001) to predict the flow regime over the flat surface and the results showed reasonable agreement with the experiments. Chay *et al.*, (2005) conducted numerical simulation of downburst wind loads using steady RNG (Renormalization group)  $k-\epsilon$  and obtained good agreement with downburst wind-tunnel results. Kim & Hangan (2007) and Das *et al.*, (2010) performed both steady and transient 2-D RANS studies to investigate the macro scale flow dynamics of an impinging jet model, producing reasonable radial-velocity profiles and good primary-vortex representation. Sengupta & Sarkar (2008) carried out numerical simulations using different RANS models (Standard  $k-\epsilon$ , RNG  $k-\epsilon$ , Realizable  $k-\epsilon$ , Shear stress transport (SST- $k-\omega$ ), Reynolds stress model (RSM) and Large eddy

simulation (LES) for studying jet impingement flow characteristics and its effect on the nearby structures. The results predicted from the realizable, RSM and LES have been seen to match the experimental data better. However, the numerical models too suffer from some limitations when applied to the IJ flow. Chay *et al.*, (2006) pointed out that the k- $\epsilon$  model underperformed in predicting the maximum outflow speed and maximum turbulent kinetic energy (TKE) generated at the stagnation region. Myszko and Knowles (1995) found out that the standard k- $\epsilon$  model failed to accurately predict the thickness of the wall jet. Also, the transient features of the IJ flows were not fully explored in a lot of numerical simulations. A limited set of field data and laboratory experimental data available for comparisons gave little confidence to apply the RANS model for extensive investigation of the downburst flow field.

## 2.3 Full cloud model

The shortcomings of the impinging jet model in not being able to simulate the near surface flow accurately gave importance to the numerical modelling of the life-cycle of the downbursts producing cloud by simulating the microphysical thermodynamic processes (formation of rain, hail, precipitation, etc.) termed as the “full-cloud model”. This approach not only enables to examine the nonstationary characteristics of the downbursts, but the near-surface wind features can also be investigated in a greater detail (Hjelmfelt *et al.*, (1989), Proctor, (1987,1987), Srivastava, (1987), Orville *et al.*, (1989); Knupp (1989), Proctor and Bowles, (1992); Proctor, (1993); Straka and Anderson, (1993), Nicholls *et al.*, (1993), Guo *et al.*, (1999); Sun *et al.*, (2004). The results from these studies suggest that the downdraft intensity increases with an increasing lapse rate in temperature. Not only that but the boundary layer humidity and the environmental wind shear has been shown to play key roles in the microphysical processes forcing the downbursts (Knupp, (1989). Straka and Anderson (1993) simulated several thunderstorm producing downbursts using this model and were able to discover that the sublimation of snow played a minor role in the downburst formation, however, Proctor and Bowles (1992) showed that the sublimation was the major cause of negatively buoyant air in forcing strong downbursts initialized with observed atmospheric soundings. However,



most of these studies were based on some idealized assumptions, such as prescribed precipitating particles on the top of a model or an idealized cloud process and, therefore, were not designed to study downburst formation by simulating the whole storm evolution. Undoubtedly these complex modelling approaches has the ability to produce outflows close to real events, yet they deal with the limitations of high computational costs and time which often are not suitable for developing design codes of building structures. This model, therefore, has been more popular in the atmospheric science community rather than the wind-engineering community.

## 2.4 Cooling source (CS) model

In order to reduce the computational costs required to simulate the full-life cycle of the parent cloud producing downbursts, Anderson *et al.*, (1992) introduced an alternative approach where the microphysical processes from the atmospheric full cloud model is replaced by a space and time-dependent cooling source (CS) function imposed at the elevated region of the domain. The CS function was ellipsoidal and was based on the field study conducted during the Cooperative Huntsville Meteorological Experiment (COMHEX; Wolfson and Iacono, 1987). The CS function models the thermodynamic cooling caused by the evaporation of precipitation in the thunderstorm cloud, in order to create a cold mass of air similar to that of cool downdrafts observed in nature. This CS model produces thermal stratification and, hence, density gradients across the domain creating a negatively buoyant flow to that produced during a thunderstorm (Anderson *et al.*, 1992; Vermeire *et al.*, 2011). This approach is more suitable to examine the near-flow ground flow dynamics where temporally varying wind-profiles are critical for wind-resistant design of building structures. Orf *et al.*, (1996) and Orf and Anderson (1999) had adopted this approach to study colliding and translating downbursts referred to as Wisconsin Model Engine (WME). In both cases, it was found that the resultant wind shear patterns pose extreme hazard to the aviation and that the maximum peak velocity exceeded that of those found on single downburst event in quiescent environments. Lin *et al.*, (2007) implemented this approach with the Bryan Cloud Model (CM1, Bryan and Frisch (2002)) to examine stationery and translating outflows for a single isolated

downburst. The results showed that the shape of the vertical profiles of velocity resembles a wall jet profile and the maximum wind speed of a translating downburst occurs much closer to the ground surface than a non-translating downburst. Vermeire *et al.*, (2011) compared the outflow results from the CS model with that of an IJ model. It was found that the IJ model is not accurate particularly for modelling near surface outflow and the buoyancy driven effects. The magnitude of the wind components are over-predicted over the height of the maximum radial velocity. Orf *et al.*, (2012) also suggested that IJ and CS models are not sufficient enough for capturing the spatial and temporal characteristics of the near-surface downburst producing thunderstorm flows in compare to a full 3D cloud model. An axisymmetric model used by Mason *et al.*, (2009) however could be still useful for predicting radial winds around the strongest downburst. Studies carried out by Oreskovic, (2016) showed that the CS simulation results are still scalable with the existing scalable metrics that are applied to the IJ models. However, the CS model still has some limitations. Mason *et al.*, (2009) and Zhang *et al.*, (2013) showed that the CS models are highly dependent on the initial conditions. Mason *et al.*, (2009) showed that the shape of the downdraft forcing function plays a significant role in the vortex development around the descending downdraft and the subsequent surface outflow structure. The height at which CS downdraft is initiated influences the location at which the maximum outflow velocity is observed. The CS model is also difficult to simulate experimentally with sufficient scale limiting its validation. This has led to challenges in conducting wind load tests on scaled laboratory models which are of particular interests to wind engineers. The discussion is concluded by noting the fact that although the CS model is less expensive than the full cloud model, its applicability remains limited due to spatial and temporal complexity of the model along with the lack of understanding the scaling criteria.

## 2.5 Density-driven model

Although the CS model is difficult to simulate experimentally, a similar experimental approach exist which do not necessitate the presence of the thermal gradients to achieve the negative buoyancy effect in the cooling source model. This is called a “two-fluid

approach” or a density driven model which is based on a density difference between two fluids. This is achieved by releasing the fluid with higher density (dense fluid) within the less dense fluid (ambient fluid). The ambient fluid corresponds to the less dense atmospheric ambient air and the dense fluid corresponds to the cold downdraft constituents (dense air, precipitation, hail, etc.), respectively. The governing phenomenon through which the downdraft develops is identical to the downbursts in reality where a parcel of air descending from cumulonimbus clouds forming the outflow experiences baroclinic vortex formation. However, after the downdraft touches the ground the radially spreading outflow can be regarded as a gravity current progressing in horizontal direction (Alahyari, 1995; Babaei, 2018).

This modelling approach was first implemented by Lundgren *et al.*, (1992) where a dense fluid (salt-water solution) held in a small cylindrical container was released by a cylinder at its bottom into the into a fresh water (figure 2.6). A laser induced fluorescence (LIF) technique was used to visualize the flow field (descending vortex ring) of the simulated microburst. The microburst model was trivial in the sense that viscosity and the refractive index of the fluids were not taken into consideration while choosing the lighter and the heavier fluids. Aqueous solutions of glycerol (ambient fluid) and potassium phosphate (dense fluid) having a negligible difference in the refractive indices for the range of density difference were used by Alahyari (1995) allowing optically based flow measurements. The results showed that the leading edge of the falling fluid rolls up into a vortex ring, which after impacting the ground expands radially outwards. The unsteady adverse pressure gradients created near to the surface causes the boundary layer to separate and form secondary roll-up vortices. Interaction of the primary vortex (formed from the vortex rings) and the secondary vortices causes sharp spatial variations in the velocity field nearer to the surface. Perhaps it is important to highlight that there were no differences between the release cylinder mechanisms of Lundgren *et al.*, (1992) and Alahyari and Longmire (1995). Both had used an open-ended plastic cylinder with a thin stretched latex membrane which was released open using a needle inserted through a hollow support rod. This cylinder release mechanism however had some limitations. Firstly, releasing the dense fluid with a piercing needle seemed trivial and may have

issues with repeatability of the experiment if care is not taken while piercing the membrane. Secondly, the solid wall of the release cylinder holding the dense fluid creates a barrier between the two fluids which is absent in natural downbursts. In order to circumvent these issues, Babaei, (2018) designed a novel cylinder release mechanism installing iris gates at the top and the bottom of the cylinder. Motor-driven top and bottom aperture replaced the membrane for initiating the dense fluid release. The solid wall of the cylinder was re-designed with a porosity of 25%. This technique not only improved the repeatability of the events generated but also greatly reduced the wall effect separating the two fluids mimicking the flow nature as in real downburst events. The increased wall porosity caused the outflow to have enhanced mixing, leading to a lower average density of the falling mass causing a 23.2% reduced descent speed compared to a solid wall release cylinder (Babaei, 2018). In general, there is one more limitation to the density-driven approach and that is the limitation to the scale. Lundgren *et al.*, (1992) had a length scale ranging between 1:9000 and 1:45000, and a velocity scale of 1:85. Alahyari and Longmire (1995) had a length scale of 1:25000, and a velocity scale of 1:200, whilst Babaei, (2018) had a length scale of 1:16000 (Graat, 2020).

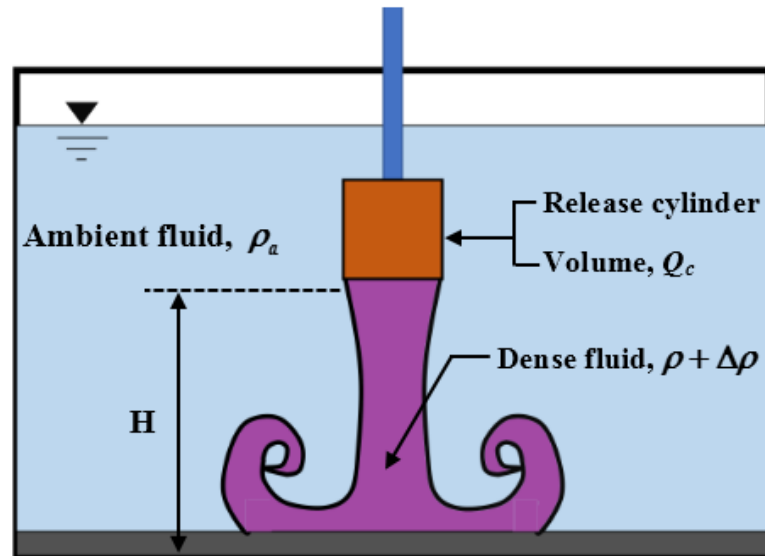


**Figure 2.6 Experimental arrangement of density-driven downbursts with dimensional parameters (adapted from Lundgren *et al.*, 1992, Alahyari and Longmire, 1995).**

The primary scaling parameters of this modelling approach are the equivalent spherical radius ( $R_0$ ) (resembling the downburst radius) and the release height ( $H_0$ ) (resembling the height of the cloud base from ground) (figure 2.6). Development of a scaling law defining the characteristic length and time scales (equation 2.2-2.5) allowed the comparison of full-scale downburst characteristics with the model scale studies (Oreskovic, 2016).

$$R_0 = \left( \frac{3Q}{4\pi} \right)^{\frac{1}{3}} \quad (2.2)$$

$$T_0 = \left( \frac{R_0 \rho}{g \Delta \rho} \right)^{\frac{1}{2}} \quad (2.3)$$

$$V_0 = \frac{R_0}{T_0} \quad (2.4)$$

$$Re_0 = \frac{V_0 R_0}{\nu_a} \quad (2.5)$$

where,  $Re_0$  is the characteristic Reynolds number based the characteristic length and velocity scale (equations (2.2) and (2.4)) and  $\nu_a$  represents the kinematic viscosity of the ambient solution.

Implementing the Laser induced florescence (LIF) technique allows the estimation of the radius of the outflow before and after the touchdown with ground (Lundgren *et al.*, 1992). Lundgren *et al.*, (1992) noticed that the radius of the outflow increased in a linear manner before touchdown, with a maximum rate of radial propagation of  $0.16V_0$ . After touchdown the gust font accelerates to a maximum velocity of  $0.5V_0$  and, then, decelerating to a constant velocity of  $0.2V_0$ . The radius of the microburst gust font is seen to be independent of  $Re_0$  for  $Re_0 > 3000$  (Lundgren *et. al*, 1992). The horizontal velocity after touchdown, however, has been higher ( $2.5V_0$ ) in Alahyari and Longmire (1995) than what is observed in Lundgren *et. al*, (1992) and Babaei, (2018).

Applying the Lundgren scaling law (Lundgren *et al.*, 1992) to different experimental trials with varying density difference and release height ( $H_0$ ) to the results of Babaei, (2018) revealed that this law can effectively collapse the effect of the different geometrical parameters (Babaei, 2018). This is consistent with the results of Lundgren *et al.*, (1992) and Alahyari and Longmire (1995) where the evolution of the flow field was seen to be independent of the initial release height. Alahyari and Longmire (1995) postulated that this occurs due to the height of the initial release being sufficient for the circulation to develop, before the touchdown. All these observations are, therefore, only valid for  $H_0/R_0 > 1.9$  cases where the circulation is nearly well developed before the outflow reaches the ground (Alahyari, 1995; Babaei, 2018).

Babaei *et al.*(2021) also carried out experimental simulation of translating downbursts with newly designed iris gates mechanism with a traversing mechanism descending onto non-zero ambient flow having velocities ranging from  $V_{trans}/V_0 = 0.320-0.675$  where,  $V_{trans}$  represents the translational velocity of the release cylinder. The results from indicate that the presence of the ambient flow does not change the variations of the frontal height in a significant way (refer to figure 3.22(c) in Babaei, (2018). The touchdown time of the travelling downbursts ( $5.20T_0$ ) was less than that of the stationary downburst ( $5.47T_0$ ). With the increase in the velocity of the ambient flow, the leading and the trailing edge of the downburst was seen to advect in the direction of the flow. The radial front speed which propagates in the direction of the ambient flow is not affected by the impact on the ground, whereas the radial front speed in the direction of the ambient flow is affected by the impact on the ground. Since the velocity fields of the release experiments were not measured, the influence of the ambient flow on the radial velocity magnitudes could not be characterized.

The next section identifies the potential gaps in the previous researches concerning the study of downburst and highlights why this study is required to understand the dynamics of translating downburst in the presence of ambient flow.

## 2.6 Conclusions and Motivations

As discussed in the previous sections the impinging jet model lacks the primary driving force for the downburst event and meteorological field studies are high cost and difficult to implement, whereas studies involving cloud models and cooling sources model are computationally expensive. Nevertheless, these approaches provide significant background theory which is useful for carrying out the present work for example 1) Field studies provide data for comparing and validating the experimental and the numerical studies 2) Cooling source models gives information on the physical dimensions of the downburst outflow, specifically the  $H/R_0$  ratios. 2) Density driven models resembles the formation of negatively buoyant air mass within a thunderstorm cloud and, therefore, mimics the primary force behind the vortex generation within a downburst. It also provides a reliable scaling approach required to compare laboratory simulated results against the atmospheric field data. Considering its relative advantages over other approaches, the density-driven model has been adopted in the current study.

It is well known from the field studies, that in nature, downbursts events are part of larger, dynamic thunderstorms and that these storms are translating locally within regional scale weather systems such that ambient winds are present before, during and after any single downburst event. The translating IJ model work has all been done by translating the jet nozzle without the consideration of ambient horizontal wind motion. Moreover, none of the previous studies implementing the density driven model have accounted for significant ambient shear introducing an atmospheric boundary layer formed over a rough terrain. It is therefore imperative that a more comprehensive study addressing these gaps are required to understand the interaction of the downbursts with the ambient flow structure and this, therefore, forms the premise of the current investigation.

The next chapter discusses the experimental facility, along with the description of the release apparatus and measurement methodology that has been adopted to acquire and process the experimental data.

## Chapter 3

### 3 Experimental Methodology

This thesis work includes experimental work segregated in two stages, first, generating a realistic atmospheric boundary layer (*ABL*) within a hydraulic flume and second generating a traveling downburst event within that. The current chapter, therefore, discusses the key aspects used to design the experimental work which involves i) selection of the roughness array to generate the *ABL* flow, ii) and techniques used for simulating the translating downburst event. A Particle image velocimetry (*PIV*) velocity measurement technique has been employed to capture the resultant flow field within the simulated downburst event. The next section discusses the hydraulic flume channel within which the experiments have been carried out.

#### 3.1 Density-driven downburst model

The density-driven model simulating a downburst event incorporates the concept of adapting the density difference between the downburst column and the surrounding atmosphere into the experimental simulations. Hence, a fluid pair (dense and ambient fluid) exhibiting a density difference similar to nature is used, where the dense fluid is held inside a sealed release cylinder immersed into the ambient fluid and later exposing the dense fluid to the ambient by using a quick release cylinder mechanism. The evolution of the density driven model technique to produce downburst like flows is discussed in detail Section 2.5 of Chapter 2.

#### 3.2 Selection of dense and ambient fluid

The dense and the ambient solutions represent the dense downburst constituents and the atmospheric air, respectively. The Boussinesq approximation allows replacement of the gaseous matter in real atmospheric events with liquid solutions and hence this approximation further enables to focus on the relative density difference between the solutions rather than the absolute difference (Alahyari, 1995; Babaei, 2018). The aqueous solutions of glycerol and potassium dihydrogen phosphate are selected as the ambient and



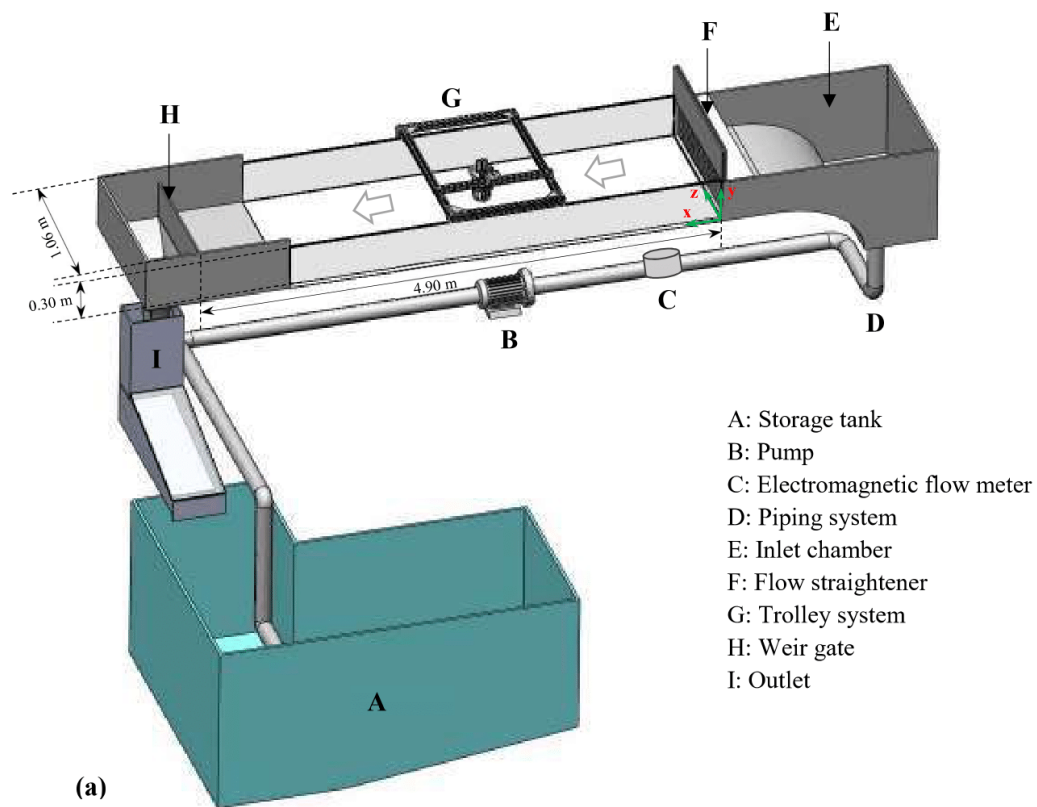
dense solutions, respectively. The primary reason for selecting these fluids is that this fluid pair exhibits negligible variation in refractive index (allowing measurement techniques involving optics e.g. *PIV*) within the range of  $\frac{\Delta\rho}{\rho_a} \times 100\% = 1.95 - 5.51\%$  and are miscible. Furthermore, the solution pair has been shown to simulate downburst-like events successfully within the range of  $\frac{\Delta\rho}{\rho_a} \times 100\% = 1.95 - 5.51\%$  (Babaei, 2018). The following table summarizes the characteristics of the solution pair:

**Table 3-1 Physical properties of the ambient and dense solution pair**

<b>Aqueous Solution</b>	<b>Density (<math>\rho</math>)  (<math>kg / m^3</math>)</b>	<b>Density difference  <math>\left(\frac{\Delta\rho}{\rho_a} \times 100\right) (\%)</math></b>	<b>Dynamic Viscosity  (<math>\mu</math>) (<math>mPa.s</math>)</b>	<b>Dynamic Viscosity difference  <math>\left(\frac{\Delta\mu}{\mu_a} \times 100\right) (\%)</math></b>	<b>Refractive- index difference  (<math>\Delta n</math>)</b>
Glycerol (ambient)	1014.4	3.37	1.20	3.89	0.0001
Potassium dihydrogen phosphate (dense)	1048.6		1.16		

### 3.3 Hydraulic flume

The hydraulic flume is a closed-circuit recirculating liquid open channel. Under normal operating conditions, a flow velocity ranging from  $2.8 \text{ cm/s}$  –  $7 \text{ cm/s}$  is achievable over a smooth wall test section. A fluid storage tank (A) (Refer to figure (3.1)) capable of containing a volume of  $3\text{m}^3$  acts as an underground reservoir for the re-circulating liquid (ambient fluid). The metal gates covering the storage tank allow easy access to the reservoir for preparing the aqueous glycerol solution used as an ambient fluid in this case. An Armstrong pump (4380 series; 1800 RPM) mounted on a strong foundation on the floor is used to draw the glycerol solution from the reservoir to the inlet chamber of the flume (E). The piping system has an inside diameter =  $10 \text{ cm}$ ; length=  $4\text{m}$  with a metal plate covering at the end (attached with holes on each side) allowing the flow to exit freely. A uniform distribution of flow is therefore achieved inside the inlet chamber. A uniform distribution of flow is therefore achieved inside the inlet chamber.



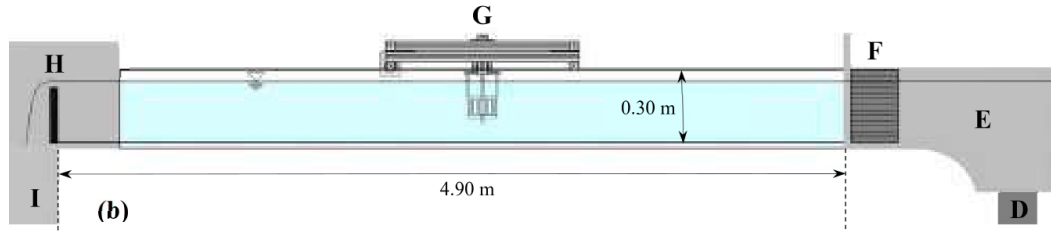


**Figure 3.1 Schematic diagram of the hydraulic flume system a) 3-D view; b) 2-D view (adapted from Babaei, 2018; published with author's permission)**

Further flow uniformity distribution inside the flume is achieved with a mesh stand installed right above the inlet point. The mesh screen was designed by combining a perforated plate with a wire mesh that partially breaks any large-scale turbulent motion generated by the pump leading the flow to the inlet chamber through a 4 m long pipe. The side walls and bottom wall of the contraction section with a projected length of  $L_c$  located in the inlet chamber of the flume can be represented by a cubic (equation 3.1) and elliptical equations (equations 3.2 & 3.3), respectively, preventing rapid pressure drop and flow separation. The following equations representing the contraction chamber use the distance  $x_c$  as the distance from the reference point set as the upstream end where the contraction starts (Babaei, 2018).

$$y_L = 352.4 \sqrt{1 - \left( \frac{x_L}{L_c} - 1 \right)} \quad (3.1)$$

$$z_L = 1.581 \times 10^{-6} x_L^3 \quad 0 \leq x_L \leq 0.6L_c \quad (3.2)$$

$$z_L = 188.8 + 3.5 \times 10^{-6} (x_L - L_c)^3 \quad 0.6L_c \leq x_L \leq L_c \quad (3.3)$$

At the end of the inlet chamber lies an aluminum flow straightener with honeycomb shaped cell sections (length = 15 cm; cell size= 0.5 cm approximately) which serves as the entry point for the flow into the flume section.

The flume working section is rectangular in shape with dimensions  $4.5m \times 1.06m \times 0.30m$  representing the length, width, and depth, respectively. It is made up of clear tempered glass sections (thickness =  $1.5\text{ cm}$ ) allowing optical access up to  $3.5\text{ m}$  downstream from the inlet, whereas a further  $1.5\text{ m}$  is made of stainless-steel sections. A weir gate at the end of the test section allows controlling of the flow depth in the flume, allowing a maximum flow depth of  $28\text{ cm}$  without spillages from the free surface of the channel flow. The flow continuing to move over the weir is transported back to the storage tank through a rectangular conduit which completes the flow circuit. The system is equipped with a flow control valve and air vent at the entrance of the pump which allows priming of the pump before usage.

### 3.4 Release cylinder

The current approach of downburst simulations employing the density-driven approach uses a release cylinder mechanism equipped with two irises at the top and bottom end of the cylinder separating the dense and ambient fluids when in the closed position. As shown in figure (3.2) the cylinder walls contain 12 uniformly spaced cavities containing cylindrical pins with cavities matching up with that of the main cylinder. (porosity = 25%) (elaborated in Section 2.5). During the normally closed state the two irises and the cylinder wall pins close completely to seal the dense fluid inside the release mechanism. The key operations of the release mechanism, such as the opening of the two irises and the rotation of the cylindrical pins, are driven by an Oriental stepper motor (CSK266-AT) where the gears in mesh with the irises are driven by a pinion driven by a shaft from the motor and the cylindrical pins rotate from a cam shaft mechanism driven by gears surrounding the irises. The stepper motor is installed over a supporting structure holding the release cylinder system with long enough bars to keep the stepper motor above the free surface of the ambient fluid. A cylindrical tube passing through the centre of the cylinder extending from the bottom iris all the way above the stepper motor helps sealing the cylinder as the irises close against the central pin surrounded by rubber seals. This cylindrical tube has holes at the bottom which allows filling the cylinder with the dense solution from the top end of the tube through a funnel. The swift opening operation (0.5

seconds) (opening of the two irises and rotation of the cylindrical pins) is controlled through a LABVIEW program.

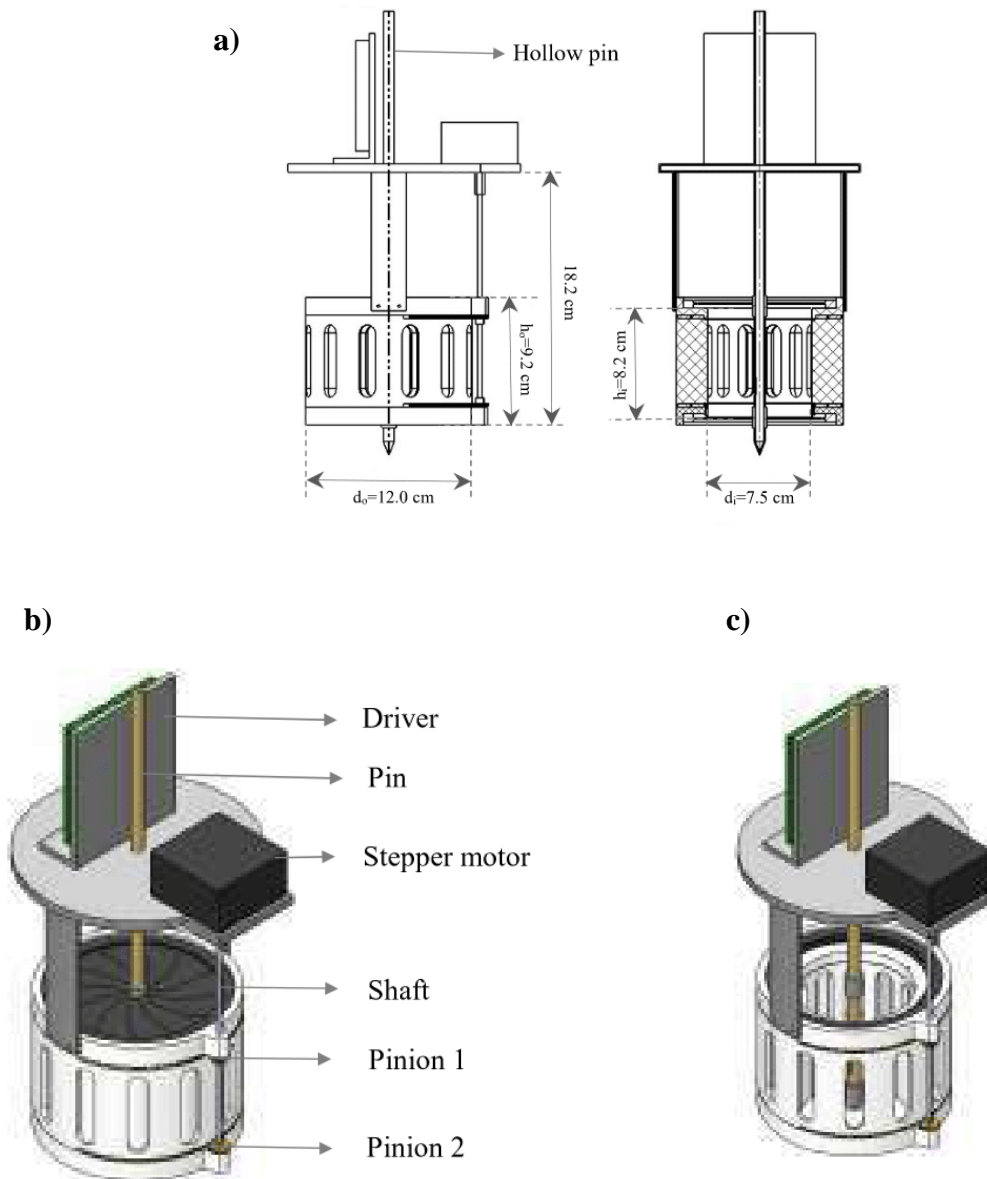


**Figure 3.2 Downburst release cylinders, a) sectional view of the release cylinder b) closed position; c) open position (adapted from Babaei, 2018; published with author's permission)**

### 3.5 Traverse system

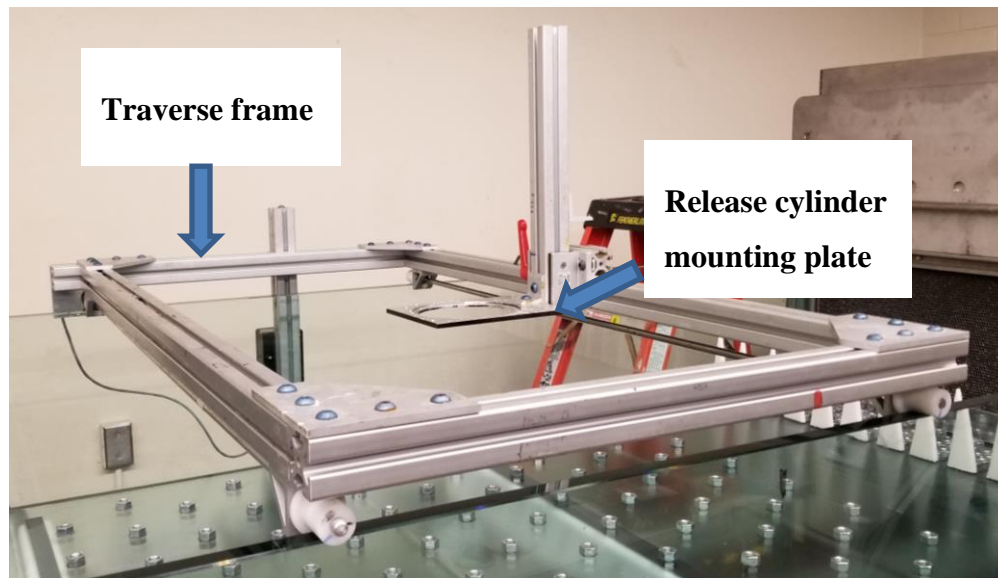


**Figure 3.3 Traverse system mounted over the flume side walls containing the release cylinder mounting component**

The translating downburst event is achieved by mounting the release cylinder into a hollow opening on a L-sectioned plate which can be mounted to the trolley system. The trolley mechanism is a square frame made up of aluminum extrusions attached over plastic wheels that can roll without slipping over the edges of the glass walls of the flume working section (figure 3.3). The trolley system is driven by a LABVIEW controlled DC gearmotor. Moreover, a linear encoder attached on the frame of the trolley system track the distance travelled by the trolley, which in turn permits repeatable release experiments at a specified downstream location from the flume inlet.

### 3.6 Generation of atmospheric boundary layer at model scale:

The *ABL* prevailing over Earth's surface extends up to 1000 m from the ground (refer to Section 1.2). The *ABL* formed over a region depends on the wind speed, terrain roughness (upstream as well as at the region where boundary layer depth is considered) and the Coriolis parameter at the location. Experimental simulation of an adiabatic *ABL* over a limited length of fetch in a wind tunnel or an open channel requires the installment

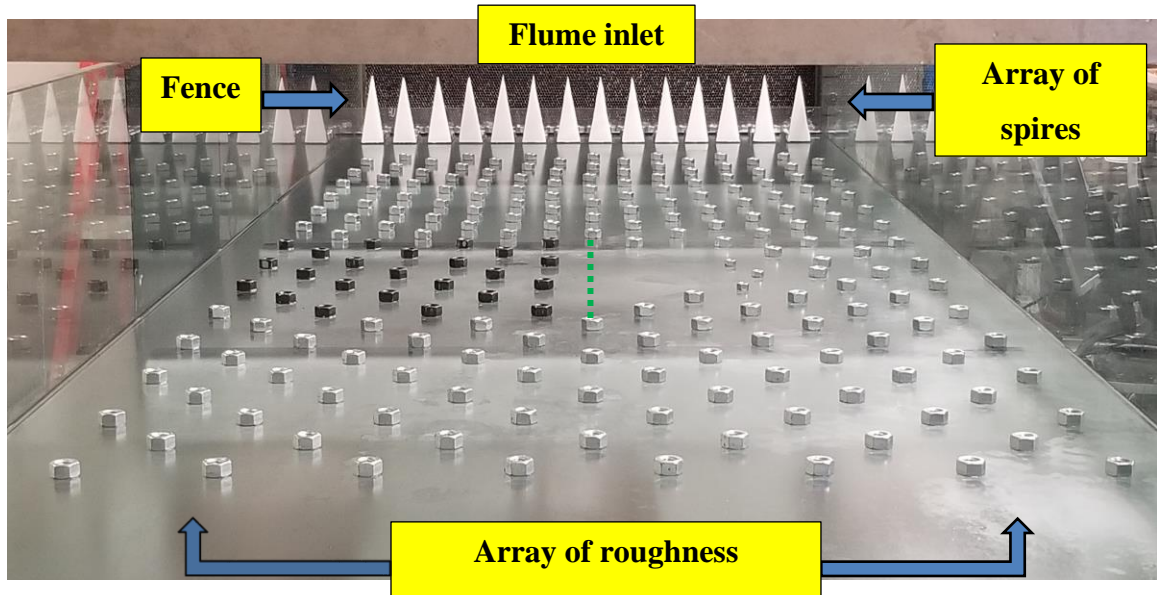
of passive turbulence generating devices over the flow bed (Counihan,1973). The present work is restricted to simulating the adiabatic *ABL* and, hence, neglecting the considerations of the thermal gradients affecting the *ABL*. The current work adopts a combination of mixing devices like spires, fence, and an array of roughness elements (hexagonal nuts) for simulating *ABL* flow inside the working section of the hydraulic flume (open channel).

The boundary layer characteristics for the smooth wall boundary layer over the hydraulic flume were characterized by Babaei (2018), where a laminar boundary layer thickness of 2.35 cm and free stream turbulence intensity of approximately 20% was obtained at the highest pump flow rate ( $Q_p$ ) of 19.10 L/s. Concerns about the high freestream turbulence levels in the flume system and non-uniform entry of fluid in the inlet chamber of the flume a mesh stand was designed by the present author and installed as an addition to the facilities to allow uniform entry of the fluid into the inlet chamber and reduce the freestream turbulence levels. A scaling ratio of 1:16000 was adopted by Babaei, (2018) for modelling the stationary travelling downburst event and, hence, the initial calculations pertaining to the selection of the roughness elements were based on using this scaling ratio due to the same release cylinder apparatus being used for the present study. It should be noted that the final scaling ratio for the combined simulation of the *ABL* and downburst events is discussed in Chapter 4.

An *ABL* can be regarded to as a turbulent boundary layer at model scale considering the similarities that exist among the two entities. Hence, an objective of simulating the *ABL* in the flume was to ensure that transition from laminar to turbulent boundary layer should occur to enhance the shear in the flow. The average depth of the urban and rural boundary layer can be considered as 600m as summarized by an extensive review of adiabatic boundary layer parameters (Counihan, 1975). Hence, the downscaled urban/rural type boundary layer in the current experiment can be taken as 37.88mm. In order to achieve this boundary layer profile over the available fetch (4.5m) of the flume an array of roughness elements (hexagonal nuts of 12mm thickness), a barrier, and mixing devices (spires) are used. (Counihan, 1968; Cook, 1978). The selection criteria

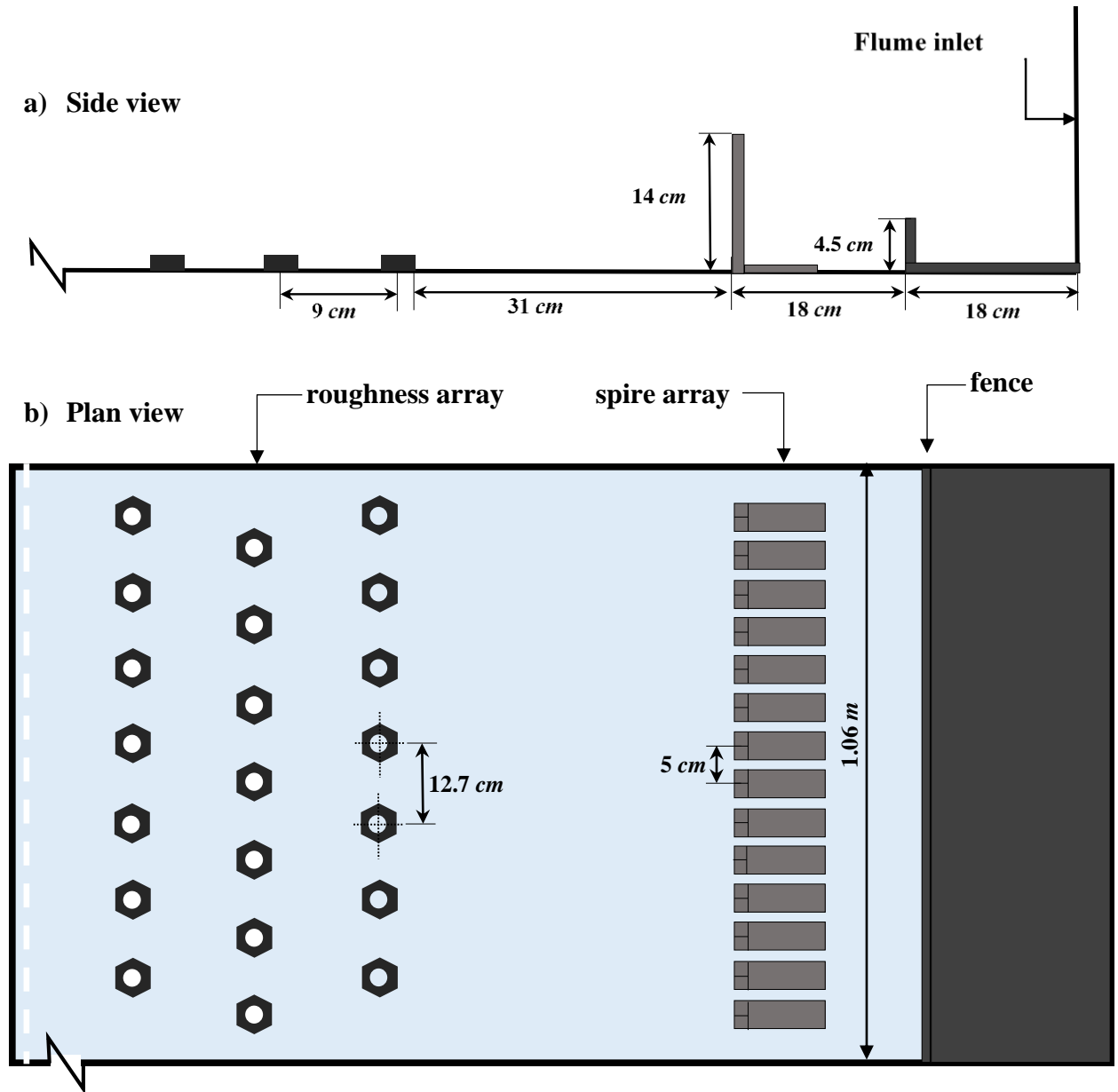
considered for the roughness elements (hexagonal nuts) and spires is elaborated in Appendix(A).

Figure (3.4) illustrates the arrangement of the turbulence generators (fence and spires) and the roughness elements. A staggered configuration of roughness array is implemented to achieve a higher shear in the flow (Macdonald *et al.*, 1998). The arrangement of the staggered roughness array in figure (3.4) gives a plan area density ( $\lambda_p = A_p / A_0$ ),  $\lambda_p = 3.0\%$ . The measurement plane is highlighted in figure (3.4) with a hatched green line and is located at the centre of the flume's width. Also, to avoid distortion of the *PIV* laser sheet by the roughness elements a narrow space where the laser sheet passes through the glass bottom was kept empty by skipping a line of roughness elements. Also, roughness elements in front of the measurement plane obstructing the field of view for capturing the *PIV* images were removed until the field of view was clear which caused no effect on the boundary layer development in the central measurement plane. Moreover, the roughness elements situated near the laser sheet were painted black to avoid any reflections in the *PIV* images from the polished steel bodies of the nuts.



**Figure 3.4 Setup of turbulence mixing devices over the flume bed to generate ABL flows.**





**Figure 3.5** A schematic of arrangement of the roughness configuration at the inlet of the flume to generate ABL flows.

### 3.7 Experimental parameters

The boundary layer experiments for the *ABL* simulation were performed over the hydraulic flume system. A fluid depth of 28 *cm* was maintained for all the experiments. The identifiers defining the boundary layer experiments are introduced using Table (3.2). The ‘Rough wall’ in Table (3.2) indicates that the same setup of an array of roughness elements, fence, and spires was adopted as shown in figure (3.4 & 3.5).

**Table 3-2 Details of experimental runs for boundary layer case for *ABL* flows.**

Identifier	Flume bed condition	Pump flow rate, $Q_p (L/s)$	Free stream Velocity, $U_\infty (cm/s)$
R-A	Rough wall	9.15	3.04
R-B	Rough wall	19.10	6.65

**Table 3-3 Details of experimental runs for downburst release experiments**

Identifier	DB-1-A	DB-1-B	DB-2-A	DB-2-B
Release height ( $H_0$ )( <i>cm</i> )	10.5	10.5	14.5	14.5
$H_0 / R_0$ ( $R_0 = 4.42cm$ )	2.38	2.38	3.28	3.28
Ambient <i>ABL</i> simulation	R-A	R-B	R-A	R-B
Free stream velocity ( $U_\infty$ )( <i>cm/s</i> )	3.04	6.65	3.04	6.65

The parameters defining the downburst release experiments are as shown in Table (3.3). The release height of the cylinder from bottom wall defines the various cloud base heights from the ground in reality. In Table (3.2) ‘R’ in the identifier column depicts

rough wall condition, respectively within the hydraulic flume. In Table (3.3) the lettering scheme for the identifiers is defined as “(DB-stands for downburst)-(1/2stands for the various release heights)-(A/B refers to the pump flow rate ( $Q_p$ ))”. In order to model the travelling downbursts, the release cylinder is translated with the corresponding freestream velocities for the R-A and R-B case.

### 3.8 Experimental procedure

The boundary layer experiments were sampled at 10 *Hz* frequency and, in total, 10,000 samples were acquired (16.67 minutes of flow time) for each case to achieve statistical convergence. Due to the limitations of the computer RAM a continuous experiment capturing 10,000 samples was not possible and, hence, 10 sets of data with a continuous sampling for 1,000 samples were obtained.

The boundary layer experiments with Identifiers: R-B and R-A represent the freestream velocities of 6.7 *cm/s* and 3.9 *cm/s*, respectively. Hence, the translational velocity of the release cylinder is matched with the freestream velocities by assigning the required duty cycle for the trolley system motor.

The dense solution (potassium phosphate solution) is prepared in batches and seeded with Silicon Carbide particles to achieve uniform seeding between the dense and the ambient fluid. The Silicon Carbide powder is added by careful judgement and the seeding density is checked by subsequent trials, with the seeding concentration adjusted if required.

The downburst release experiments start with first establishing the ambient flow in the flume with a working depth of 28 *cm*. At a reference point at 1.2 *m* from the flume inlet the release cylinder is filled, and the traversing starts from this fixed location. The release cylinder is filled with dense fluid ( $Q_c = 362ml$ ) slowly while simultaneously lowering it inside the ambient fluid to avoid trapping of air bubbles inside the cylinder. To minimize any leakage from the release cylinder the traversing is started immediately after the cylinder is filled and submerged by installing it beneath the trolley system. The release is controlled using a LABVIEW code and starts at 1.9 *m* from the flume inlet. The transient

event is sampled at 10 Hz by the *PIV* system until the cylinder is seen to have exited the field of view (400 samples). The constant recirculation of the ambient fluid disperses the dense fluid and allows the subsequent runs to be done one after the other without any significant time delay. Moreover, in a previous study the stationary and travelling downburst release experiments revealed no change in the density of the ambient fluid due to mixing of the dense fluid after a considerable number of subsequent downburst release runs. (Babaei, 2018).

### 3.9 Particle Image velocimetry (PIV)

*PIV* is a non-intrusive velocity measurement technique involving the addition of tracer particles into the flow. These tracer particles are illuminated by a high “pulse power” laser system and tracked by capturing time separated image pairs. For the current experiments the entire volume of the ambient solution (Volume = 3 m<sup>3</sup>) inside the storage tank was seeded with silicon carbide particles of approximately 2 μm mean diameter. The gravity induced free-settling velocity for the particles in motionless fluid can be calculated from the following equation derived from Stokes’ drag law (Raffel, 2018):

$$U_g = d_p^2 \left( \frac{\rho_p - \rho_a}{18\mu_a} \right) g \quad (3.4)$$

**Table 3-4 Fluid mechanical properties for various *PIV* seeding particles**

Seeding particles	Mean particle diameter ( $d_p$ )(μm)	Density ( $\rho_p$ )(g / cm <sup>3</sup> )	Free-settling velocity ( $U_g$ )(m / s)
Silicon Carbide	2	3.2	$3.97 \times 10^{-6}$
Titanium Dioxide	3	3.5	$1.01 \times 10^{-5}$
Hollow Glass Spheres (HGS)	10	1.1	$3.87 \times 10^{-6}$

As the silicon carbide powder exhibits low free-settling velocity (table (3.4)) in the ambient fluid and as the powder does not accumulate when dispersed into the solutions, it strongly follows the fluid motion and was selected as the seeding material. A New Wave Research Gemini dual pulse Nd:YAG laser (532  $nm$ ) system was setup on a foundation metal plate just below the bottom glass wall of the flume working section, and a combination of optics containing a cylindrical lens ( $f = -25\text{ mm}$ ) and spherical lens ( $f = 1000\text{ mm}$ ) was used to split the laser beam into a plane laser sheet (thickness= 2.69  $mm$ ). A TSI Charged Couple device (CCD) 8 MP (Megapixels) camera was used to capture the field of view illuminated by the *PIV* laser and was placed perpendicularly facing towards the laser sheet.

The Insight 4G (TSI) software was utilized to capture and store the *PIV* data. This software, in conjunction with the Laser Pulse synchronizer, controls the synchronization of the laser pulses with the image capturing by the *PIV* camera, where the *PIV* exposure time of 305  $\mu s$  and laser pulse delay of 300  $\mu s$  were set giving the best quality of image in terms of illumination of seeding particles. The *PIV* technique involves capturing an image pair (Frame A and Frame B) separated by  $\Delta t$ , the next image pair is separated by the sampling time  $t_s$  (figure 3.7). The selection of the time difference  $\Delta t$  between the Frame A and Frame B depends on a combination of factors like the flow speed and the feasible spatial resolution obtained for accurate velocity vector interpolation from the *PIV* raw data. For all the experiments the images were captured at 10  $Hz$  sampling frequency with a frame size of 3000×1000 pixels. For the boundary layer experiments (*ABL* simulation) a time gap between subsequent image pairs (Frame A &B) of  $\Delta t = 6000\text{ }\mu s$  was used, whereas for the downburst experiments a time separation of  $\Delta t = 750\text{ }\mu s$  was incorporated. These values for  $\Delta t$  illustrated optimum displacement (3-6 pixels) of seeding particles between the image frames for a progressive grid size of 64×64 pixels and 32×32 pixels for image processing, as explained further in this section.

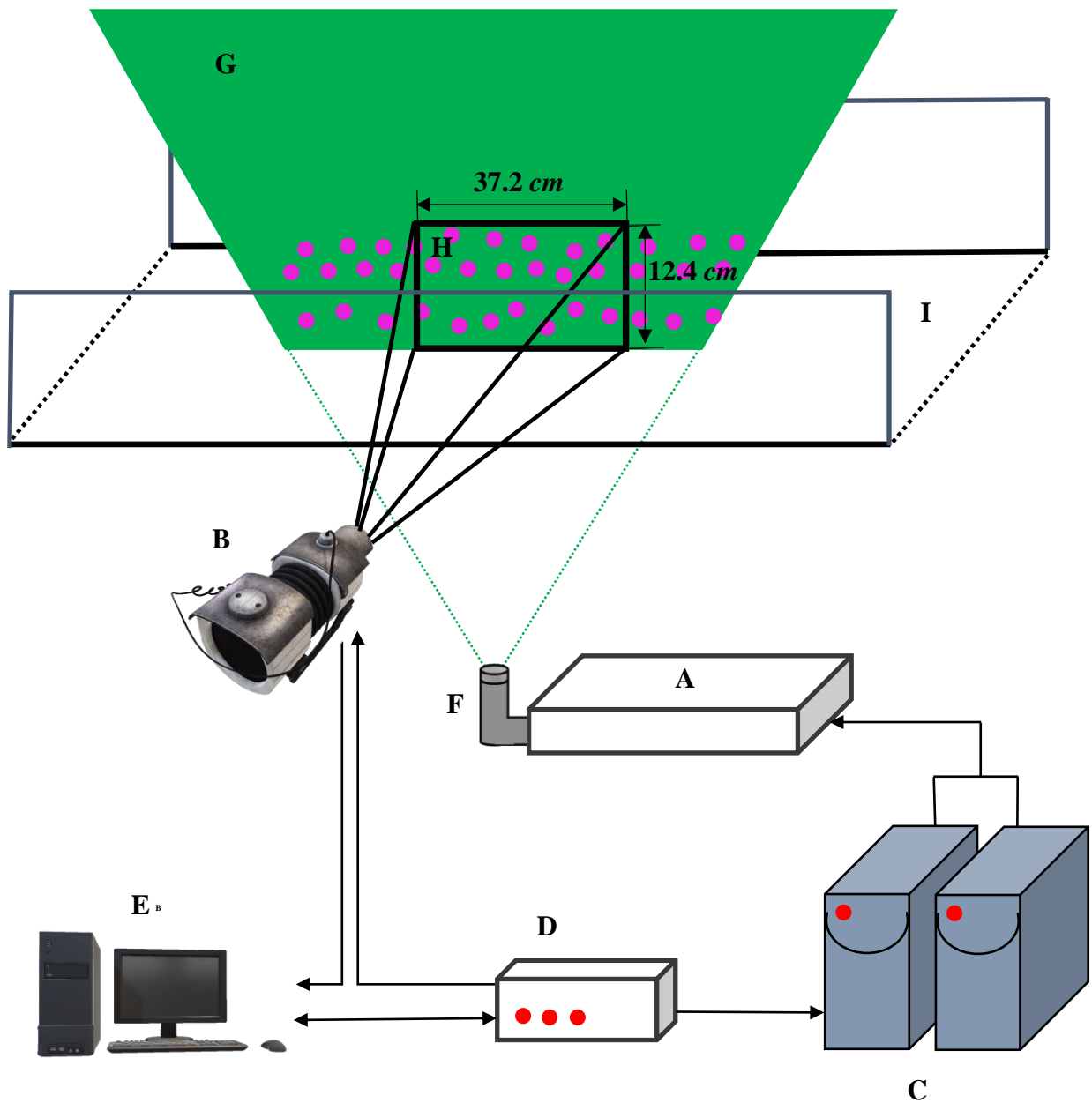


**Figure 3.6 PIV measurement system and the measurement plane displayed in the flume section (A: PIV Laser Unit, B: PIV Camera, C: Laser power units, D: Synchronizer, E: Computer system, F: Laser sheet optics, G: Laser sheet, H: Measurement plane, I: Flume section).**

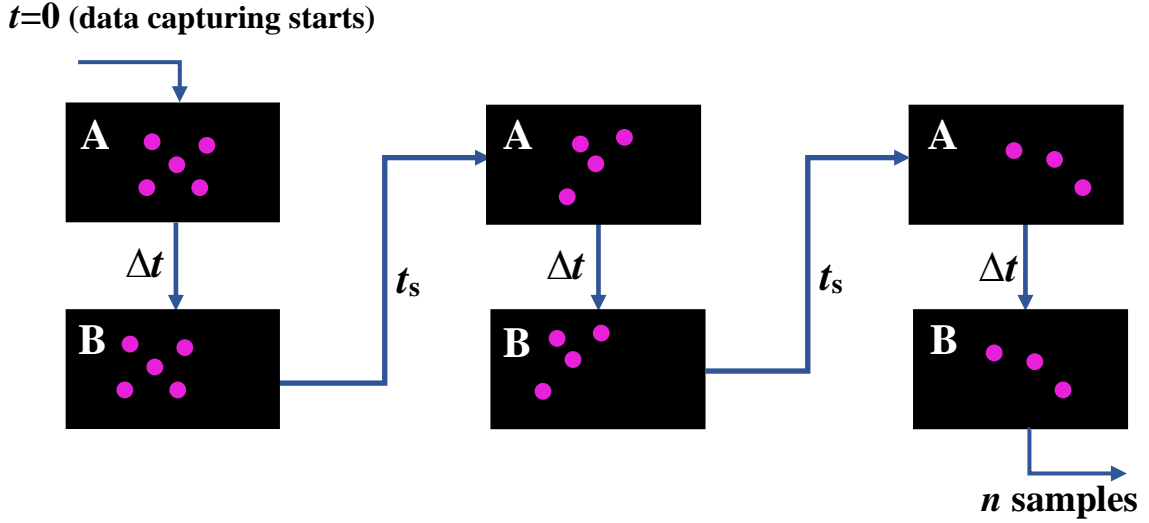


**Figure 3.7 A representation of the sequential PIV data capturing process for  $n$  number of samples with  $\Delta t$  as the time gap between Frame A and Frame B, and  $t_s$  as the sampling time between subsequent image pair.**

The velocity vectors from the *PIV* images was interpolated by tracking the displacement of a group of seeding particles in Frame A and Frame B having a time gap of  $\Delta t$ . The interpolation of the velocity vector field starts with dividing the entire field of view into equally sized square shaped interrogation spots. Assuming uniform motion of the particles enclosed by each interrogation spot, acts as a footprint identity for Frame A which is then searched for using an algorithm for its exact match in Frame B. This statistical pattern matching technique is performed by calculating the discrete cross-correlation function matrix in the frequency domain (Discrete Fourier transform (*DFT*)). The distinct peak of the function denotes the most probable displacement for that interrogation spot and, hence, the location of the peak from the centre of the interrogation spot gives the 2-D displacement vector ( $\vec{d}$ ) for the particular spot. Furthermore, the corresponding velocity vector at the spot is determined by velocity-time equation  $\left( \vec{v} = \frac{\vec{d}}{\Delta t} \right)$  (Raffel *et al.*, 2018; Thielicke *et al.*, 2014). Hence, the assemblage of the

velocity vectors from all the interrogation spots results in the velocity vector field associated with the *PIV* image pair.

For the *PIV* image processing for the boundary layer experiments and downburst experiments the PIVlab-Particle Image Velocimetry tool (MATLAB) is used. The image processing starts with dividing the *PIV* image of  $3000 \times 1000$  pixels into interrogation spots of  $64 \times 64$  pixels (Pass 1). Unlike the Direct Cross correlation (*DCC*) technique that calculates the correlation matrix in the spatial domain, a Discrete Fourier transform (*DFT*) approach is used that computes the correlation matrix in the frequency domain using a Fast Fourier transform. After computation of the displacement values in the X and Y directions for Pass 1 this displacement information is used to offset the search areas for a second pass having spot size of  $32 \times 32$  pixels (Pass 2). The *DFT* approach uses the same dimensions for the spot A and its search area spot B and, hence, there is some loss of information near the spot edges using this technique. However, in the *DCC* technique the search area for spot B can be larger than spot A, thus minimizing loss of information from particle displacement from spot edges. However, due to the high computational cost involved with the *DCC* method, the *DFT* technique can be adapted to minimize the loss of information by using multi-pass interrogation grids allowing a high-dynamic range for the velocity vector map (Thielicke *et al.*, 2014). An important limiting factor for the *DFT* technique is that the maximum displacement of the particles in a spot should mandatorily be smaller than 25% of the grid dimension to minimize background noise in the correlation matrix. Moreover, in real fluid flows the displacement of the group of particles of a spot may not be uniform considering rotation and shear motion of the fluid. To compensate for this effect, initially the displacement vector is computed at the centre of the spot (initial spot) ( $64 \times 64$  pixels). Subsequently, the grid framework is offset to allow a 50% overlap in such a manner that the four corners of the initial spot become the centre for the offset spots (refer to figure (3.8)) and, hence, now there is displacement information for 9 points for the initial spot and, therefore, using this displacement information a deformed search spot B is obtained which minimizes the loss of information (Thielicke *et al.*, 2014).



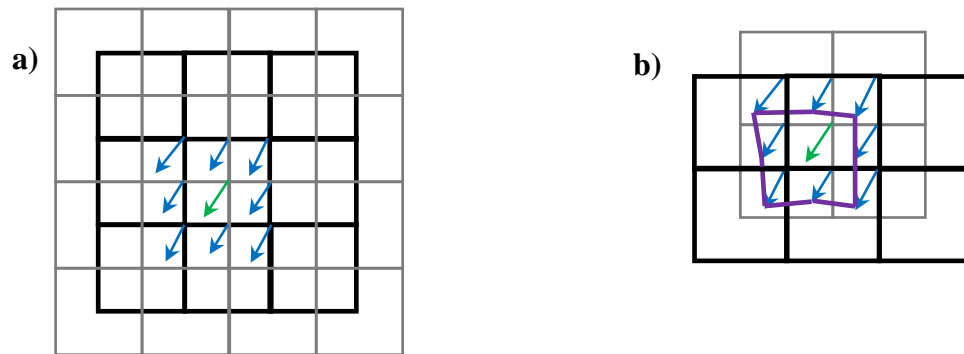


**Figure 3.8 a) an overlap (50%) of interrogation spots created by offset (grey gridlines) over the original grid (black gridlines); b) the vectors interpolated at 9 locations by grid offset used to deform the search area in Frame B (adapted from Thielicke *et al.*, 2014).**

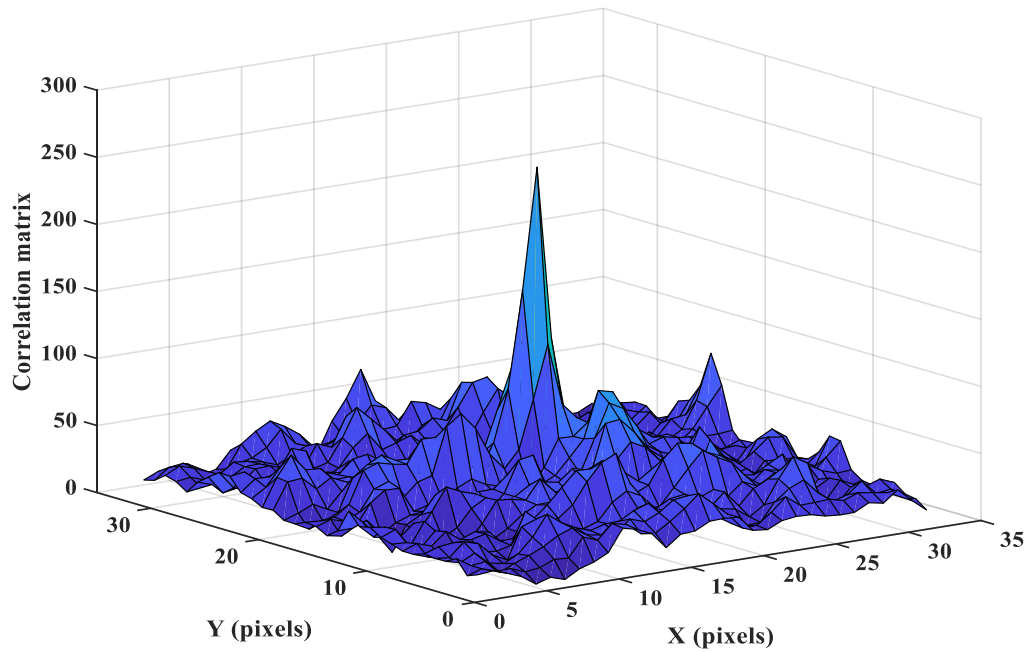


**Figure 3.9 Surface plot displaying the correlation matrix showing a distinct peak for the displacement in pixels in X and Y direction.**

The quality of the cross correlation from *DFT* is determined by low background noise and a high Signal to noise ratio (SNR) defined as the ratio of the peak intensity to the second highest peak intensity. Following the *PIV* processing procedure as mentioned above a SNR ratio above 1.5 was ensured for all the cases (figure (3.9)).

For accurately determining the displacement in pixels i.e. locating the peak of the correlation matrix with sub-pixel accuracy (rather than integers) a  $2 \times 3$  point Gaussian function is fitted separately in the x and y direction to give the final displacements with sub-pixel accuracy (Thielicke *et al.*, 2014). Lastly, a magnification factor calculated from a calibration grid is used to transform the measurements in pixels into SI units as a form of spatial calibration. The *PIV* processing setup adopted for the current study gives a spatial resolution of  $11.64 \text{ pixels/mm}$ . Also, the spatial resolution is  $0.089R_0$  when expressed in terms of the scaling radius for downburst release experiments. The experimental uncertainty related to *PIV* velocity measurements and processing for the *ABL* experiments was  $\pm 0.16 \text{ cm/s}$  (2.3%), and for the translating downburst experiments was  $\pm 1.36 \text{ cm/s}$  ( $0.11V_0$ ; 5.0%) (Appendix C).

### 3.10 Summary

Adapting the hydraulic flume to generate *ABL* flows which serves as the base simulation for further downburst release experiments is explained in detail in the current chapter. Turbulence mixing devices are used for the purpose of triggering the flow and to generate *ABL* flows over a very restrictive length of fetch. The downburst release experiments implementing the dense and ambient solutions pair are executed by matching the traverse speed with the freestream velocity of the base *ABL* experimental simulation. Particle image velocimetry (*PIV*) is used to characterize the velocity field of the events where the image processing technique employs a Discrete Fourier transform correlation method. The next chapter includes the analysis and validation of the experimentally generated *ABL* flows with full-scale *ABL* data.

## Chapter 4

### 4 Results and discussions

This chapter contains the discussions of the experimental studies generating *ABL* and translating downbursts in separate sections:

#### 4.1 Simulation of atmospheric boundary layer in hydraulic flume

This section presents the results of the boundary layer flow within the hydraulic flume system with varying ambient flow speed recorded using Particle Image velocimetry (*PIV*) technique. The data were captured at 10 *Hz* sampling frequency for 16.67 minutes (10,000 samples) while demonstrating successful convergence of statistics for the total sampling duration (Appendix B). The 2-D velocity field data interpolated by processing the *PIV* images (Section 3.9) served as raw data for further post-processing work elaborated in the current chapter.

##### 4.1.1 Boundary layer characteristics

The velocity data in the measurement section was time-averaged for 10,000 samples following a convergence check (Appendix B). The spatial variation of the mean velocity (*U*) profiles was found minimal which allows spatial averaging of the velocity data in the streamwise direction. In further analysis, the spatially averaged velocity data is used to determine the boundary layer characteristics.

Table (4.1) represents the boundary layer parameters for the two cases (R-A and R-B) cases. The free-stream velocity was taken as the average of the velocity magnitudes at all the points beyond the point when the percentage difference between the consecutive points was less than 1%. The boundary layer thickness was defined as the distance normal to the wall where the velocity magnitude attains 99% of the free-stream velocity. The momentum thickness ( $\theta$ ), displacement thickness ( $\delta^*$ ), and the Shape factor (*H*) are calculated using the following equations:

$$\theta = \int_0^{\delta} \frac{U}{U_{\infty}} \left( 1 - \frac{U}{U_{\infty}} \right) dy \quad (4.1)$$

$$\delta^* = \int_0^{\delta} \left( 1 - \frac{U}{U_{\infty}} \right) dy \quad (4.2)$$

$$H = \frac{\delta^*}{\theta} \quad (4.3)$$

**Table 4-1 Boundary layer characteristics for the *ABL* simulation**

Boundary layer parameters	R-A	R-B
Free-stream velocity, $U_{\infty}$ (cm / s)	3.04	6.65
Boundary layer thickness, $\delta$ (cm)	6.75	5.47
Momentum thickness, $\theta$ (cm)	0.61	0.50
Displacement thickness, $\delta^*$ (cm)	0.86	0.75
$H$	1.40	1.49
$Re_{\theta}$	156	281
$Re_x$	$5.47 \times 10^4$	$1.19 \times 10^5$

The Reynolds number based on the length of the flume section ( $Re_x$ ) lies in the laminar flow regime for the R-A case and the transition flow regime for the R-B case. The transition to turbulent boundary layer at low Reynolds number can be regarded to the high turbulence intensity observed in the freestream region of the flow ( $TI_u = 21\%$  for R-A, and  $TI_u = 18\%$  for R-B) (See Section 4.1.2).

The scaling parameters near the edge of the boundary layer can be defined by the boundary layer thickness ( $\delta$ ) and the free-stream velocity ( $U_\infty$ ) regarded as the outer layer scaling variables. However, near the wall ( $y = 0$ ) inner-layer scaling prevails which can be defined by the friction velocity as:

$$u_* = \sqrt{-(u'v')} \quad (4.4)$$

Alternatively, the log-law equation for aerodynamic roughness as stated in equation 4.5 can be used to obtain the friction velocity ( $u_*$ ), roughness length ( $z_0$ ), and displacement height ( $d_0$ ), which can be used as fitting variables. (fitting procedure explained in Appendix D)

$$\frac{u}{u_*} = \frac{1}{k} \ln \left( \frac{y - d_0}{z_0} \right) \quad (4.5)$$

**Table 4-2 Aerodynamic roughness parameters obtained by fitting procedure using the log-law equation**

Variables	R-A	R-B
$u_*(cm/s)$	0.14	0.35
$z_0(cm)$	$1.87 \times 10^{-3}$	$2.44 \times 10^{-3}$
$d_0(cm)$	0.06	$1.20 \times 10^{-3}$
$Re_{z_0}, \left( \frac{z_0 u_*}{\nu_a} \right)$	0.024	0.072

The displacement height is defined as the distance from the ground where the mean drag acts, thus defining the height of the zero-plane (shifted origin) from ground (Jackson, 1981). The roughness length ( $z_0$ ) is defined as the height above the zero-plane where hypothetically the velocity is zero as extrapolated from the log-law equation (equation (4.6)) (Counihan, 1971). These roughness parameters ( $z_0$ ) and ( $d_0$ ) play a key role in representing the average characteristics of the roughness array such as roughness density, height of the element, its shape and arrangement (MacDonald *et al.*, 1998).

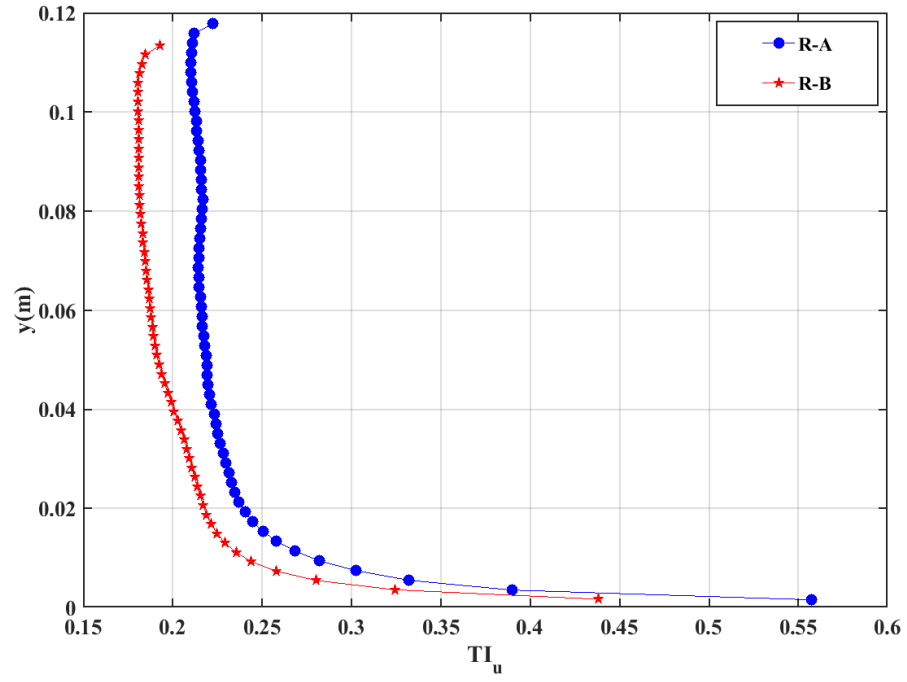
#### 4.1.2 Turbulence characteristics

In this section, the characteristics of the quantities associated with the Reynolds shear stress  $\left(-\overline{u'v'}\right)$  are discussed. The spatially averaged streamwise turbulence intensities

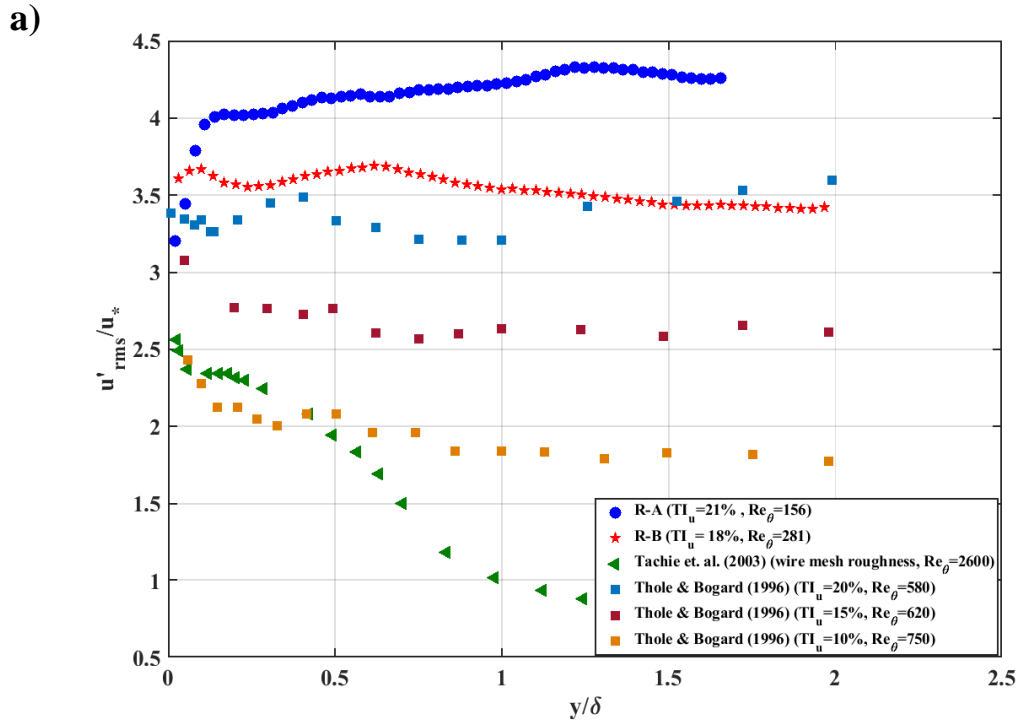
$\left(TI_u = \frac{u'_{rms}}{U}\right)$  shown in Figure (4.1) suggest that its relative magnitudes are relatively

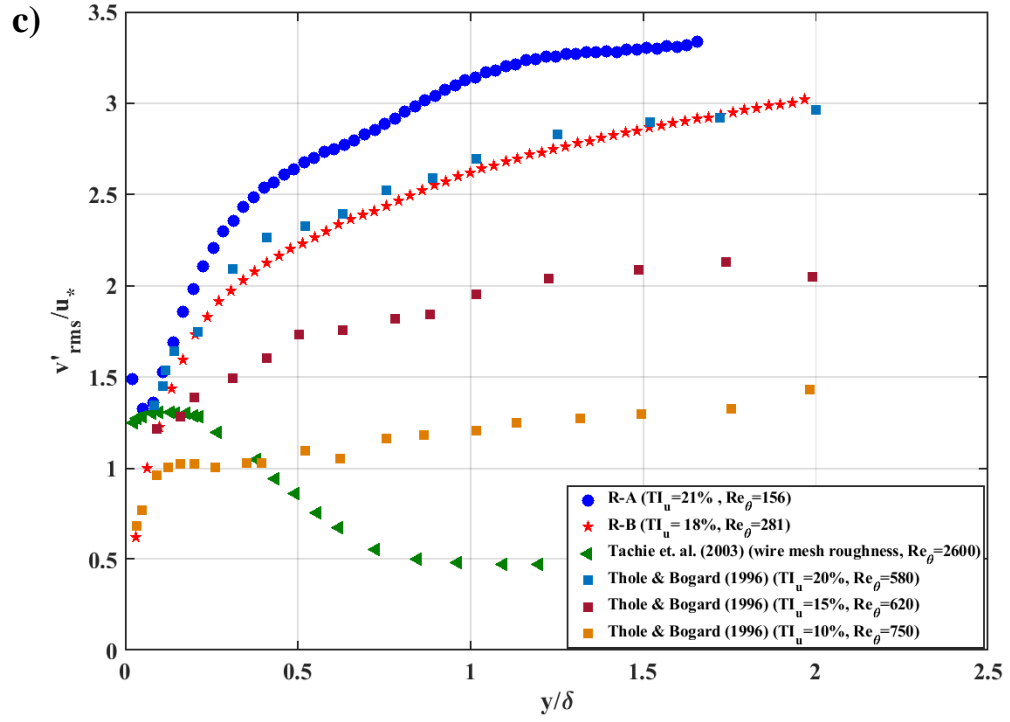
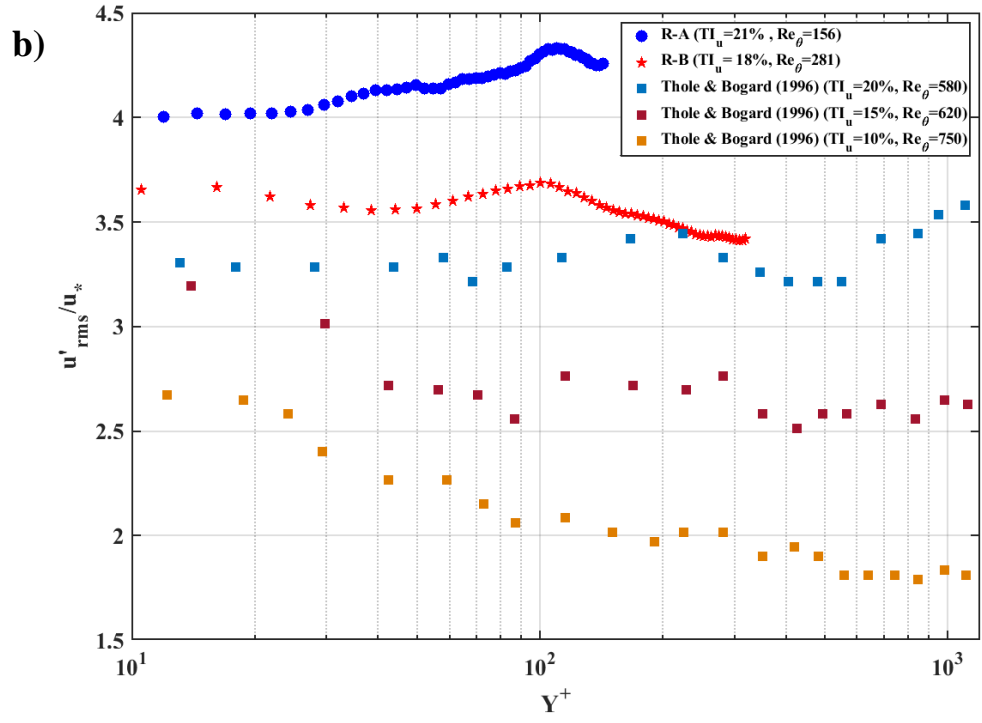
higher for low Reynolds number flow in this study. Such high turbulence intensities of 21% and 18% in the free-stream for cases R-A and R-B, are unusual and are most likely to be caused due to several factors for example short pipe length to the inlet chamber from the pump, restrictive length of contraction chamber and insufficient decaying of the large scales motion at the inlet chamber of flume.

Usually in a wind tunnel or open-channel flow the maximum turbulence intensity exists within the boundary layer near to the wall with a much smaller value in the free-stream corresponding to the turbulence in the free-stream region. This trend can be seen in Tachie *et. al.* (2003) in Figures 4.2, here turbulence intensity is defined by using friction velocity ( $u_*$ ) as the reference velocity. An attempt for validation of the turbulence intensity profiles using the inner and outer layer scaling is shown in the figures (4.2 (a to d)), however the turbulence characteristics show a poor validation with the studies.



**Figure 4.1 Spatially averaged streamwise turbulence intensities in the flume measurement section**







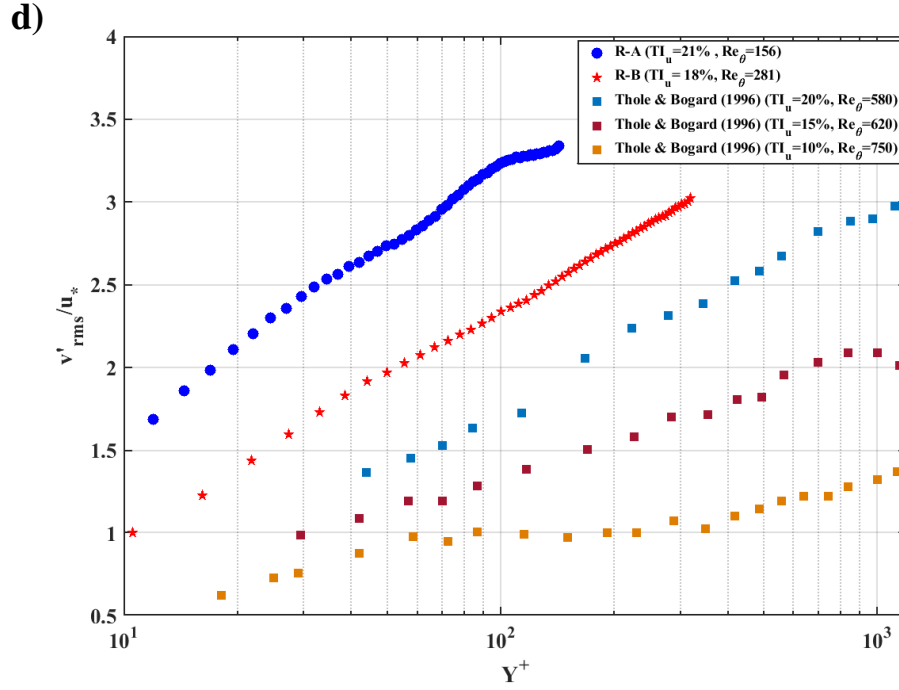


**Figure 4.2 Turbulence intensities in streamwise and vertical direction scaled using outer layer (a &c) and inner layer (b & d) scaling.**

The average size of the energy containing eddies also known as the integral length scale, can be estimated by temporal autocorrelation of the fluctuating velocity components and invoking Taylor's hypothesis of frozen turbulence. The temporal autocorrelation of the fluctuating velocity components and the corresponding integral length scale is given by

$$R(\tau) = \frac{\overline{u'(t)u'(t+\tau)}}{u'^2(t)} \quad (4.6)$$

$$L_u \approx \left( \int R(\tau) d\tau \right) * U \quad (4.7)$$

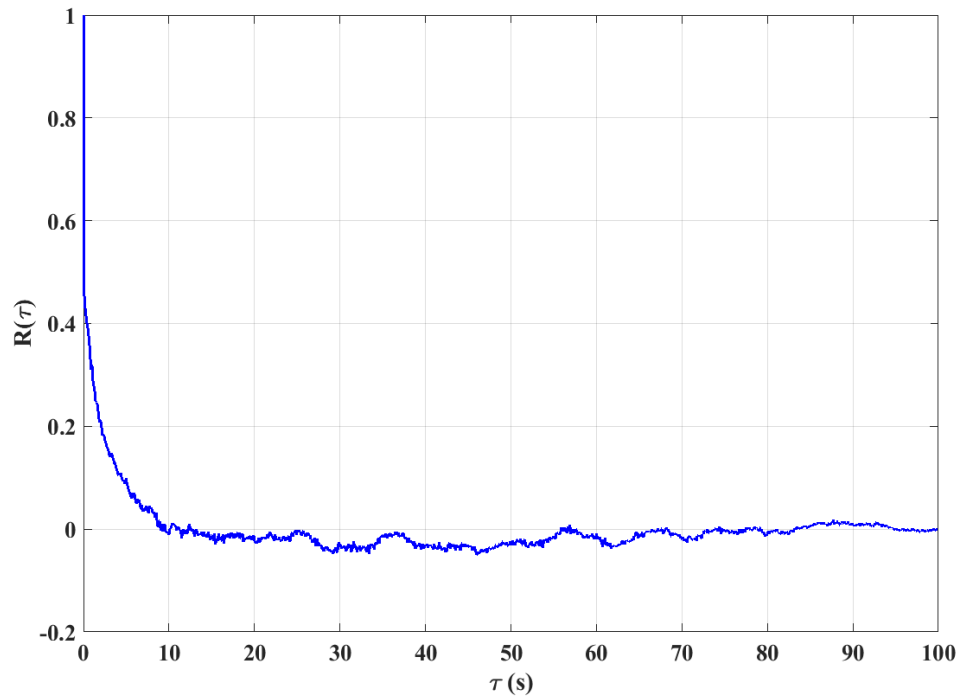


**Figure 4.3 Convergence of autocorrelation function for computing the integral time scales.**

The integral length scales can also be obtained from the energy spectra of the fluctuating velocity fitted against the full-scale ESDU data for *ABL*. Initially, the integral length scales obtained from the autocorrelation function are used to generate the non-dimensional plots of energy spectra, and later upon observing a mismatch between two curves (figure 4.4 (a)) the value of the length scale ( $L_u$ ) is fitted in order to match the ESDU curve as shown in figure(4.5 (b)) (Cook 1973). The length scales obtained from both the methods are plotted in the figure (4.5), however, the length scales obtained from the fitting procedure as being more accurate is used for further analysis.

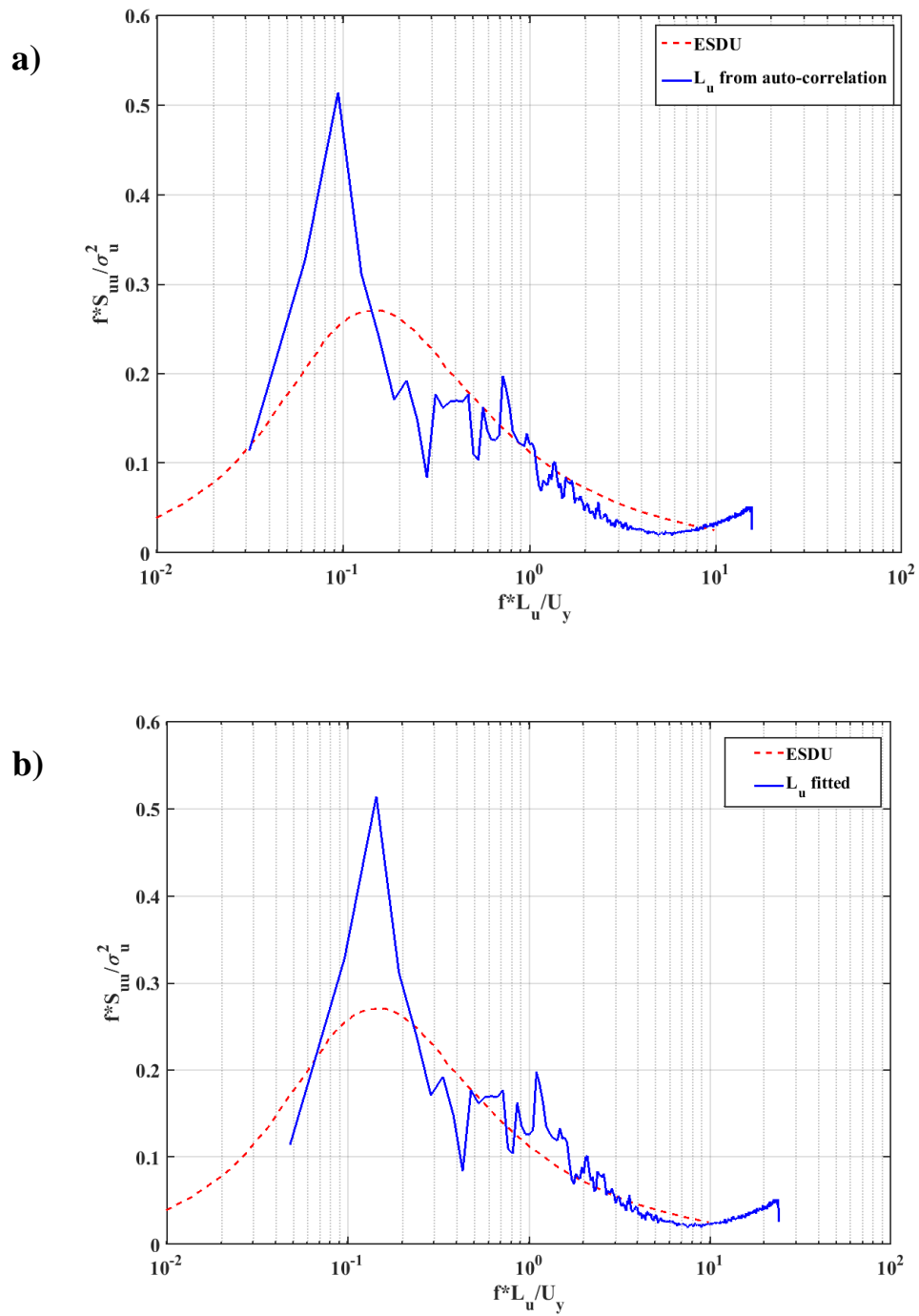


**Figure 4.4 Comparison of non-dimensional spectral energy plots with full-scale ESDU data (design curve) where the integral length scales are defined by: a) temporal autocorrelation b) fit to ESDU curve.**

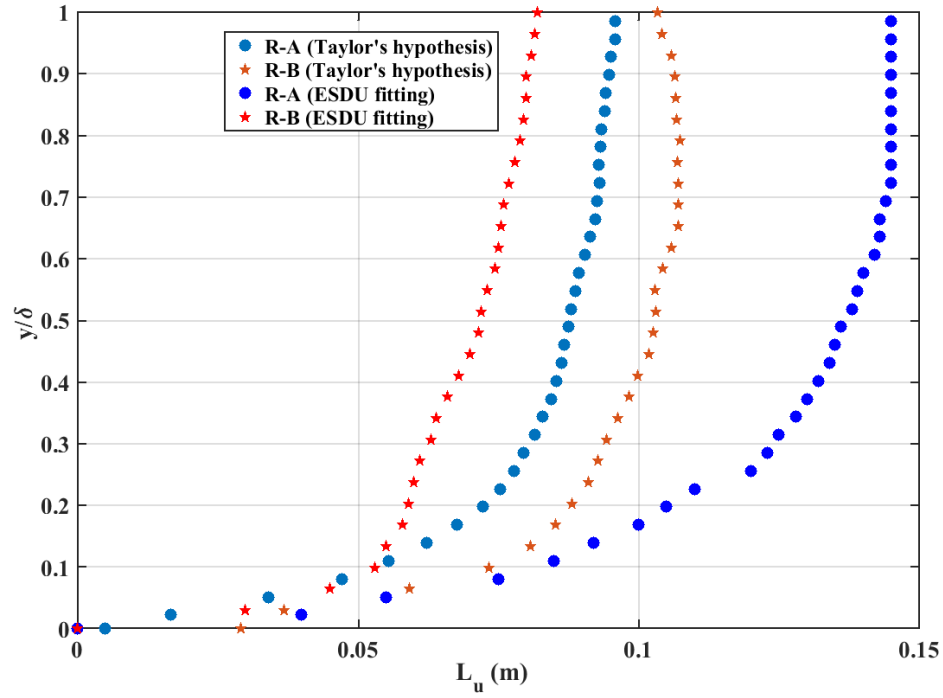


**Figure 4.5 Variation of spatially averaged integral length scales with wall normal distance.**

#### 4.1.3 Comparison with full-scale data

For accurate modelling of *ABL* within a flow-facility the simulated boundary layer should be scaled using geometric, kinematic, and dynamic similarity in an appropriate manner. The geometric similarity involves consistent scaling of the geometric dimensions at the model scale, whereas the kinematic similarity deals with scaling the velocity components, and the quantities obtained from temporal correlations of velocity such as integral length scales ( $L_u, L_v$ ). Dynamic similarity involves scaling of the forces involved, with Reynolds number being a relevant non-dimensional form. In the present work, the kinematic similarity is adopted to determine the model scale factor based on the mean and turbulent velocity characteristics. The boundary layer flow for the cases R-A and R-B falls in the transition regime and the flow is not independent of the Reynolds number. Therefore, discrepancies in matching of the *ABL* simulation from present work with the full-scale wind data can be expected.

The aim of scaling the model scale *ABL* is to determine a model scale factor which will represent the simulated *ABL* and the downburst simulation in a correct manner. The integral length scale based on the streamwise velocity component ( $L_u$ ) and the roughness length ( $z_0$ ) are the two key quantities useful in determining the model scale factor as both these quantities best represent the mean velocity and the turbulence characteristics, respectively (Cook, 1978). The empirical relation of the integral length scale in equation 4.8 can be used to obtain a model scale factor ( $S$ ) by substituting each full-scale quantity with its upscaled part (product of values at model scale with its model scale factor) resulting in equation 4.9. (Cook, 1978).

$$L_u = 25(z - d_0)^{0.35} z_0^{-0.063} \quad (4.8)$$

The model scale factor ( $S$ ) is given by:

$$S = \frac{91.3(y - d_0)_M^{0.491}}{L_{u_M}^{1.403} z_{0_M}^{0.088}} \quad (4.9)$$

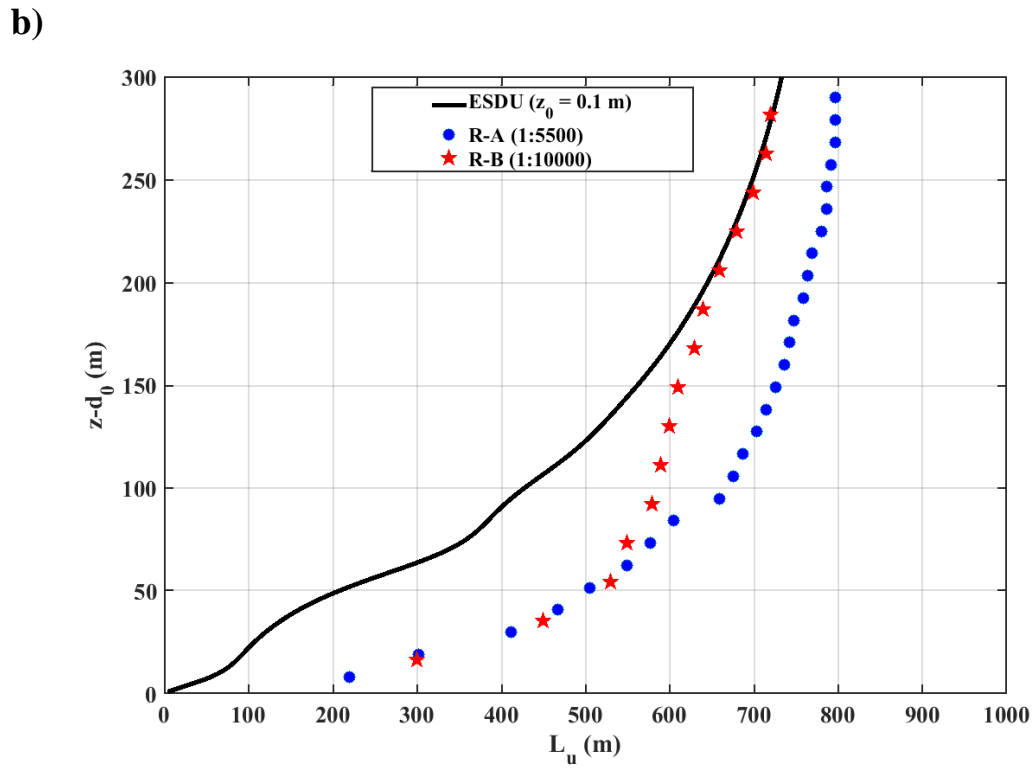
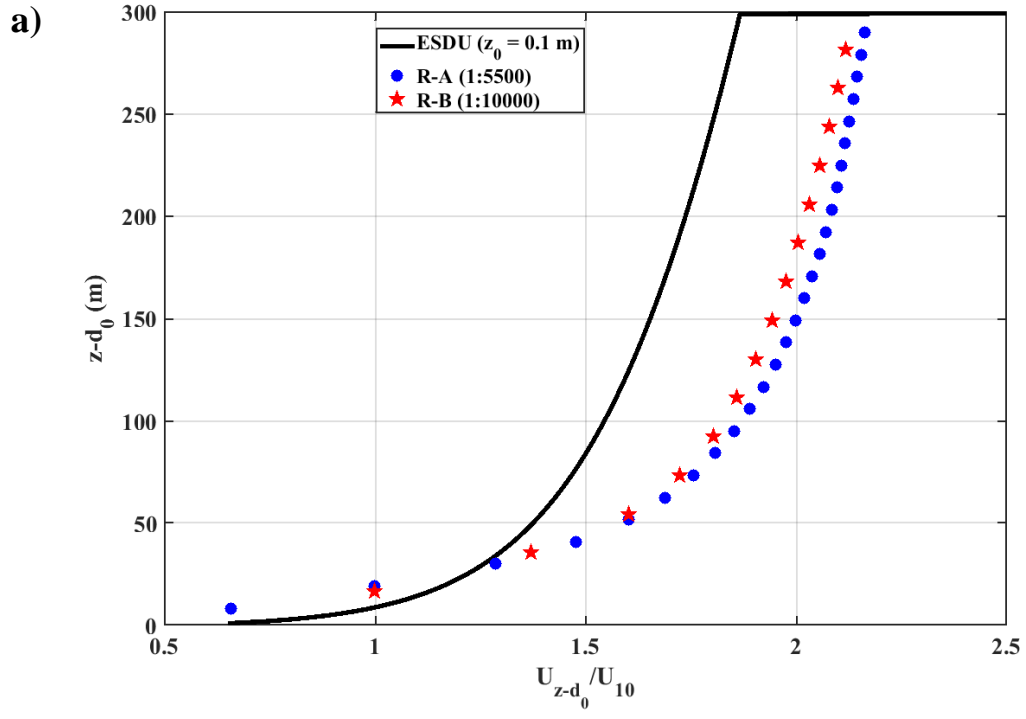
Using this approach,  $S = 2300$  and  $S = 4700$  for R-A and R-B, respectively. However, using these model scale factors result in inconsistencies in matching the mean velocity and turbulence parameters with ESDU data in terms of the roughness parameters and, therefore, this technique is only useful for estimating the model scale factor. Therefore, a more *ad-hoc* fitting trial approach is adopted which is elaborated further in this section.

A model scale factor corresponding to the *ABL* simulation can also be determined by comparing the mean and turbulent velocity characteristics with the full-scale wind velocity characteristics provided by ESDU correlations for a neutral atmospheric boundary layer. The model scale factor is obtained by finding the best fit of the velocity data profiles for the present *ABL* simulation data translated to full-scale data by using a range of trial model scale factors ( $S=100-16000$ ). A model scale factor is selected by conducting a comparative study where, upon matching of the upscaled quantities with the ESDU profiles representing a specific terrain type (represented by  $z_{0_f}$  and  $d_{0_f}$ ; subscript

' $f$ ' denotes values at full-scale) consistency is checked between the upscaled  $z_0$  and  $d_0$  values and the corresponding  $z_{0f}$  and  $d_{0f}$  at full-scale (figures 4.6 (a to d)). This results in a model scale factor of 1:5500 and 1:10000 for R-A and R-B flow cases, respectively (Table 4.3). These model scale factors result in relatively optimum match with ESDU data within a factor of 3 despite the limitations of the experimental setup such as restrictive fetch length, Reynolds number dependence, and short contraction section. Considering these experimental limitations, despite of poor scaling of the turbulence parameters in the boundary layer flow, the generation of a thicker shear layer (boundary layer) was achieved in the flume.

**Table 4-3 Comparison of the roughness parameters at full-scale obtained by using the selected model-scale factors.**

Variables	ESDU	R-A	R-B
Model-scale factor, ( $S$ )	-	1:5500	1:10000
Roughness length, ( $z_{0f}$ ) ( $m$ )	0.1	0.10	0.24
Displacement height, ( $d_{0f}$ ) ( $m$ )	0-2	3.3	0.12



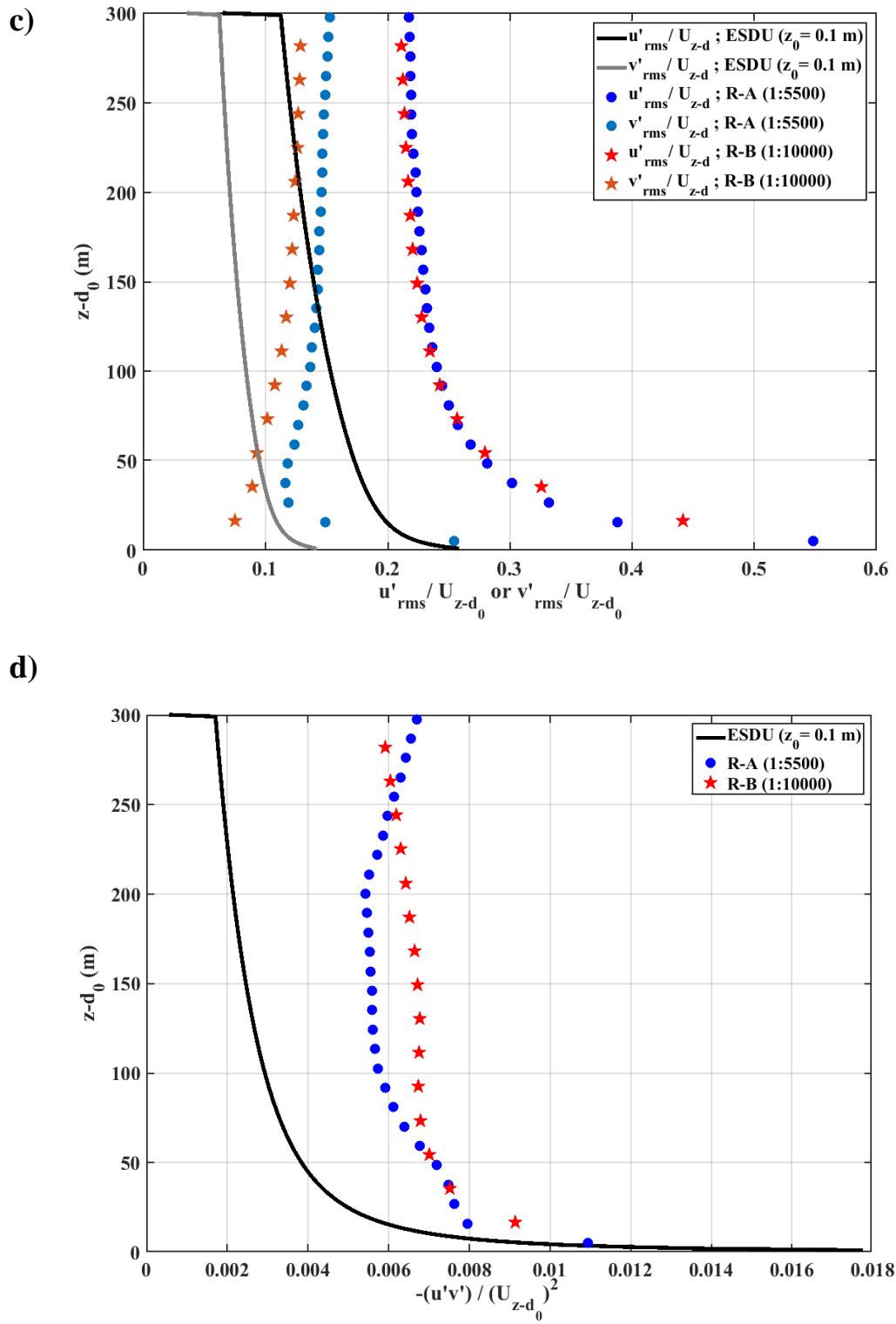


Figure 4.6 Mean velocity (a) and turbulence characteristics (b, c, &d) for the upscaled boundary layer compared against ESDU profiles.



## 4.2 Travelling downburst

This section discusses the findings from the experimental study involving the interaction of the density-driven translating downburst with the simulated atmospheric boundary layer in the hydraulic flume system with a model scale factor of the simulation as 1:5500 and 1:10,000. Using the *PIV* technique to estimate the velocity field of the event, the peak velocity and the vorticity characteristics are used to investigate the effect of shear from the boundary layer on the downburst outflows after impingement with ground. In this section the term ‘downburst’ implicitly refers to the translating downburst in the presence of ambient *ABL* flow, except the term ‘stationary downburst’ which refers to downbursts in a quiescent medium and the cylinder release occurring with no cylinder translation.

### 4.2.1 Velocity vector fields of travelling downbursts.

The present approach (density-driven model) for modelling downbursts produces three-dimensional flow fields. In the absence of any background forcing the stationary downburst can be conceptualized as an annular vortex ring formed due to baroclinic vorticity generation descending since the release has occurred and followed by impingement with the ground the outflow advances uniformly in all directions forming nearly symmetrical velocity flow field (Graat,2020). However, in the presence of the perturbation from the background *ABL* simulation (ambient flow) the downburst outflow gets convected in the direction of ambient flow forming a prominent leading edge (downstream side) and likewise a trailing edge (upstream side) is formed where the direction of downburst winds is opposite to that of the ambient. These discussed features of the downburst outflow are more clearly elucidated by observing the flow field inside a horizontal ( $x$ - $z$ ) plane as shown in figure (4.8 b).

The current study focuses on capturing the velocity characteristics in the vertical plane to characterize the transient aspects of the downburst outflow and hence the velocity measurements are conducted across a vertical ( $x$ - $y$ ) plane passing through the centre of the release cylinder (figure 4.7 (a,b)). As discussed in Chapter 3 (Section 3.8) the matching of the cylinder translation speed with that of the ambient flow was attempted,

however as the weight of the dense fluid was not taken into account while determining the speed of the traverse, the actual translation speed for the release cylinder was offset from that of the freestream velocity with the ratios as:  $U_{cyl} / U_{\infty} = 0.69$  for DB-1/2-A cases, and  $U_{cyl} / U_{\infty} = 0.63$  for DB-1/2-B cases, respectively. However, the possible effect of this velocity mismatch such as drag caused around and at the front end of the cylinder as the cylinder moves slower than the approaching ambient flow is found minimal as the boundary layer prevailing prior to the cylinder release operation corresponds to that from the boundary layer experiments within 10% (Appendix E).

The downdraft originating from a stationary downburst descends in a symmetrical manner where the outflow column touches the ground at the point coinciding with the centre of release cylinder (figure 4.8 a). In the present study as the cylinder containing the dense fluid is translating with the ambient fluid in the downstream direction, initially before the cylinder irises have opened the dense fluid has near zero relative velocity with reference to the ambient fluid motion in the free-stream region of the *ABL*. Later, since the release of the dense fluid is initiated the downburst outflow descends vertically downward and interacts with the ambient fluid. Physically, it can be conceptualized that the interaction of the downburst outflow with the simulated *ABL* occurs in two phases.

The first phase is where the outflow descends from the release cylinder in the free-stream region of the *ABL* where the downburst column experiences inertial fluid forces perpendicularly due to the approaching boundary layer flow, hence transferring the momentum to the downdraft in streamwise direction. Thereafter, the second phase of interaction starts where the downburst column enters the boundary layer at  $y=6.75 \text{ cm}$  for R-A case, and  $y=5.47 \text{ cm}$  for R-B, where it interacts with the velocity shear layer in addition to the inertial forces acting on the downflow until it touches the ground. The continuous interaction of the downdraft during the descending phase is complex which results in an asymmetrical outflow (in x-y plane) and the vortex ring in the plane of view is lifted up at the downstream side and is forced downwards at the upstream side as shown in figure (4.10). Also, the location where the downdraft impinges at the ground is shifted in the downstream direction from the cylinder centre (origin) (figure 4.8 b).

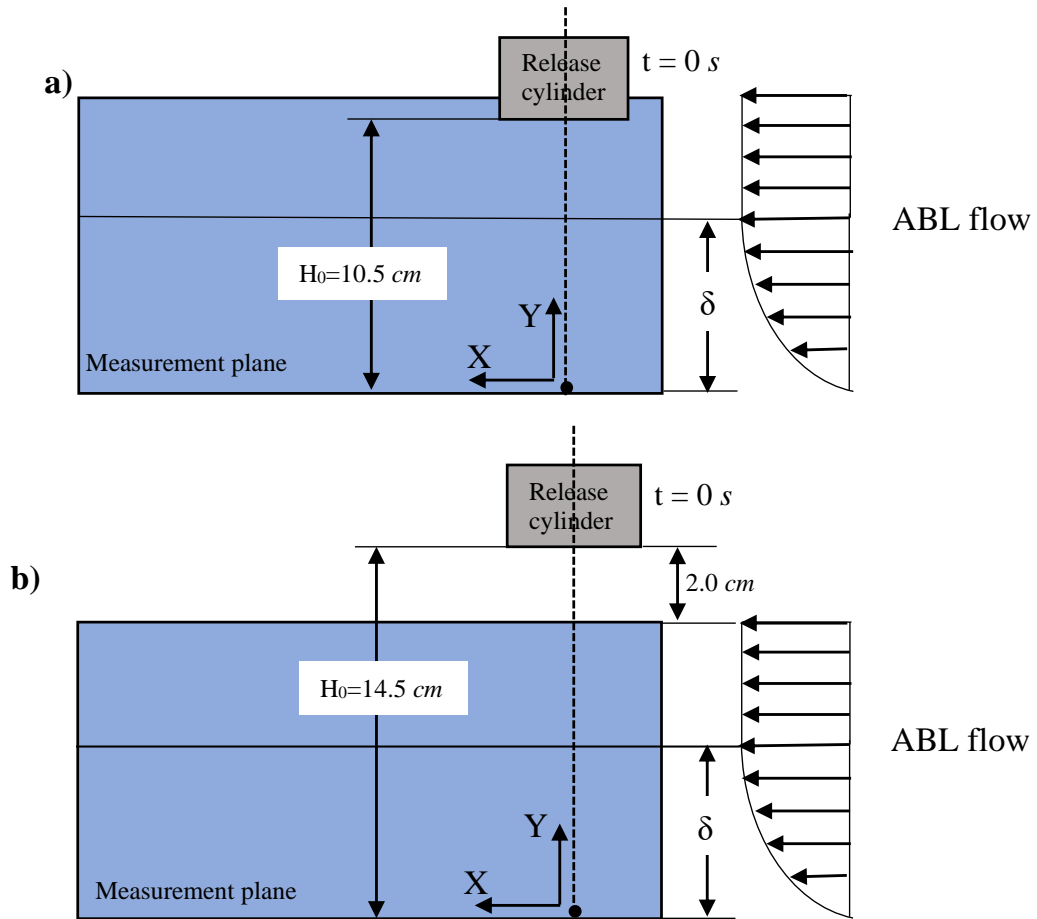


**Figure 4.7** Schematic showing the orientation of the *PIV* measurement plane relative to the release cylinder along with the reference origin used for the downburst cases  
a) For cases DB-1-A/B ; b) For cases DB-2-A/B

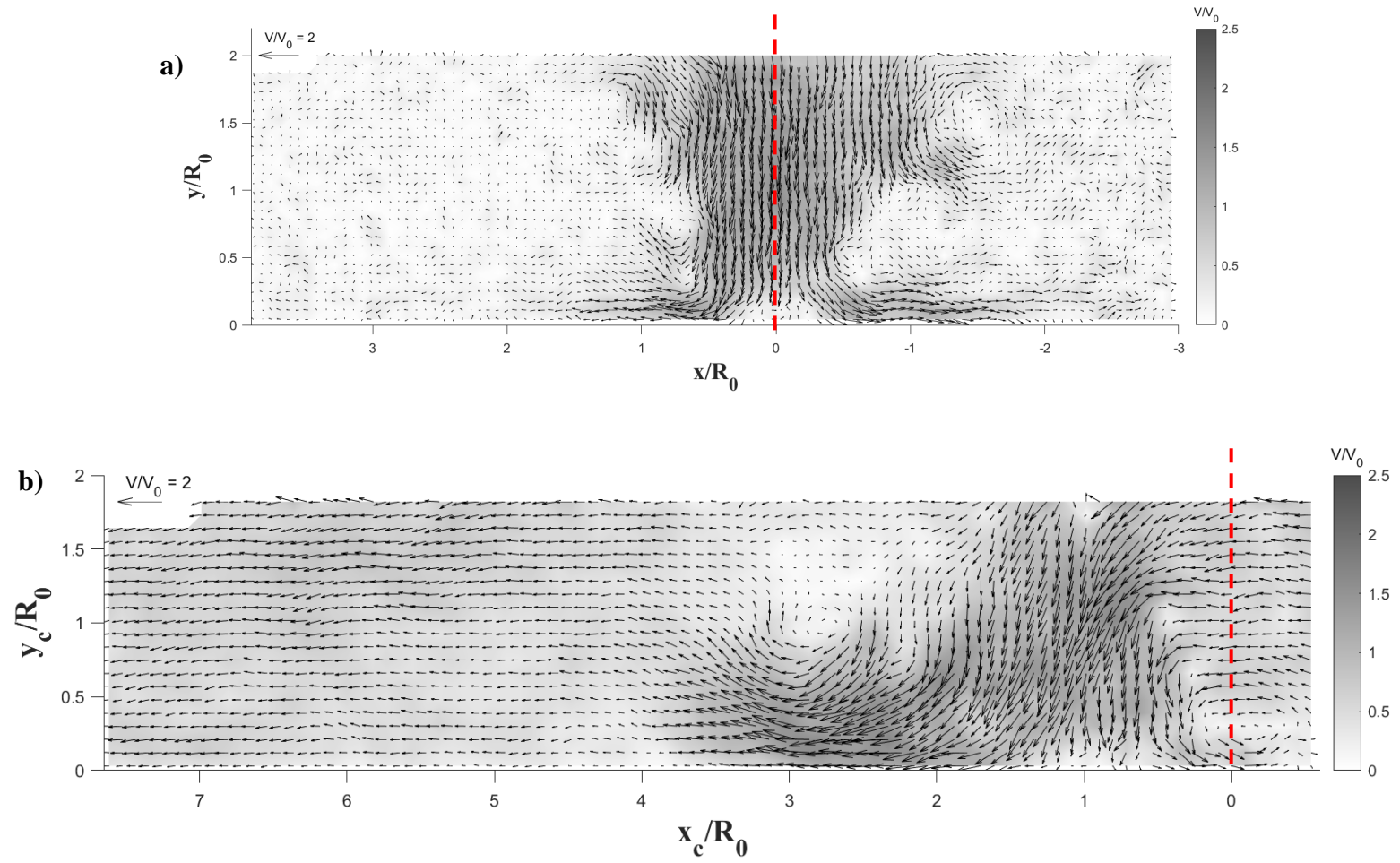


**Figure 4.8 Velocity vector fields and contour plots for a) stationary downburst (Graat,2020) b) DB-1-B at  $t/T_0 = 5.40$**

**Table 4-4 Outflow parameters at touchdown depicting the effect of the flow variables on the downburst column**

No.	Downburst Events	$\frac{t_{td}}{T_0}$	$\frac{t_{td} V_0}{H_0}$	$\frac{t_{td} U_\infty}{H_0}$	$x_{td} / R_0$
1	Stationary Downburst (Graat,2020)	4.70	1.54	-	0
2	DB-1-A ( $H_0/R_0=2.38$ ; R-A)	2.43	1.04	0.26	1.05
3	DB-1-B ( $H_0/R_0=2.38$ ; R-B)	3.51	1.50	0.82	1.23
4	DB-2-A ( $H_0/R_0=3.28$ ; R-A)	4.18	1.29	0.32	1.17
5	DB-2-B ( $H_0/R_0=3.28$ ; R-B)	4.59	1.37	0.78	2.87

The touchdown location as presented in Table (4.5) is estimated as the centre of downburst column touching the ground which can be approximated as the centre of a horizontal line segment having its endpoints as the primary vortex at the upstream and downstream side (figure 4.9). The touchdown time is visually estimated as the time frame wherein the velocity vectors of the downburst column starts diverging in the horizontal direction. The influence of the background *ABL* in convecting the downdraft downstream is evident in Table (4.5) as the touchdown location  $x_{td}$  is displaced further from the cylinder centre with the higher flow speed for the *ABL* for the cases with identical cylinder release height ( $H_0$ ) (rows 2&3, 4&5). This effect is more pronounced for the case with the higher release height as the downdraft is exposed to the *ABL* for momentum interaction for longer time until reaching the ground. Therefore, for the cases with the same *ABL* flow speed and with higher release height (rows 2&4, 3&5) larger displacement of the touchdown location can be observed. It should also be noted that the touchdown for the travelling downburst cases occurs earlier than for the stationary downburst event due to the momentum imparted by the *ABL* flow to the downburst downdraft as can be seen by larger magnitude of non-dimensional time  $\left( \frac{t_{td}}{T_0}; \frac{t_{td} V_0}{H_0} \right)$  for the

stationary downburst case in Table (4.5). For the travelling downburst cases a delay in touchdown is certain for the cases with the higher release height. Moreover, a delay in touchdown occurs for the case with the higher *ABL* flow speed as well (row 3 & 5 of table (4.5)). Hence, the influence of the increase in release height and *ABL* flow velocity

is cumulative as the higher release height augments the interaction of the downburst downdraft with the *ABL* flow.

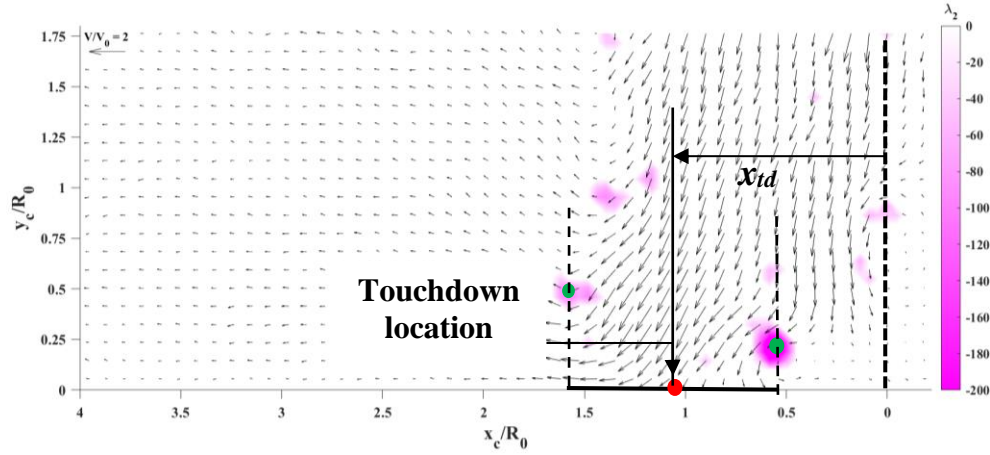


**Figure 4.9 Contours of  $\lambda_2$  criterion plotted with scaled velocity vectors at touchdown  $t/T_0=2.43$  for DB-1-A**

The velocity vector field is asymmetrically distributed about the point of impingement ( $x_{td}$ ) forming two distinct sections of outflow in the plane of view. The outflow propagating radially in the direction same as that of the *ABL* flow direction is termed as the “downstream side” (*DS*), and the radial outflow moving in the direction opposite to the *ABL* flow is termed as “upstream side” (*US*), as these outflows occur at the downstream and upstream sides of the location of touchdown of the downdraft, respectively. After the downdraft impinges on to the ground the stretching of the vortex takes place as the vertically progressing downburst column diverges into a horizontal radial outflow. This causes the vortex core to sink towards the ground at both the *DS* and *US* after touchdown. As the vortex outflow starts progressing radially it gets lifted as it gets further propelled by the remainder of the dense fluid from the downdraft column reaching the ground. During the rolling phase of the vortex its strength increases at the *DS* as it continuously entrains the ambient fluid from its surrounding in addition to the momentum forcing aiding its radial motion. Contrarily, at the *US* side after touchdown the vortex faces the oncoming *ABL* flow is directly opposing its radial propagation. After the downdraft edge has touched the ground the downdraft that has already emerged out

from the release cylinder and has a tilted structure. This causes the fluid from the *ABL* to get entrained inside the baroclinic vortices from the outflow still aloft and further forming vortices that coalesce with the primary vortex.

#### 4.2.2 Vorticity fields of the travelling downbursts outflows

The radially propagating vortex structures after the downburst reaches the ground is a prominent transient feature of these events as its evolution in time governs the downburst wind field formed near the ground. To detect the primary vortical structures for these outflows  $\lambda_2$  criterion is used which helps in differentiating the actual vortices from the shear motion and hence proving to be a robust technique compared to the vorticity function( $\omega$ ). Moreover, this method identifies the strong vortex structures by efficiently discarding weaker structures (Chen, 2015). The basic idea behind the  $\lambda_2$  criterion in a 2-D plane is that it is based on the conjecture that the vortical structures are related to local pressure minima. Hence, for the 2-D pressure Hessian derived from taking the gradient of the Navier-Stokes equation for incompressible flows (4.10) and further neglecting the viscosity and unsteady irrotational strain effects the 2-D pressure Hessian is reduced to equation (4.11) (Chen, 2015). Hence to satisfy the condition of local minimum pressure it requires the two eigen values of the 2-D pressure Hessian on the right-hand side of (eq (4.11)) to be positive which in turn requires the eigen values associated with left hand side of the equation to be negative. Furthermore, the negative eigen value associated with  $(S^2 + \Omega^2)$  can be computed for a 2-D velocity field from equation (4.12) (Chen, 2015). Hence, the vortex structures can be recognized as connected regions of the hence computed negative values for  $\lambda_2$ .

$$\frac{\partial \nabla V}{\partial t} + \nabla((V \cdot \nabla)V) = -\frac{1}{\rho} \nabla(\nabla p) + \nu \nabla^2(\nabla V) \quad (4.10)$$

$$(S^2 + \Omega^2) = -\frac{1}{\rho} \nabla(\nabla p) \quad (4.11)$$

$$\lambda_2 = \left( \frac{\partial u}{\partial y} \frac{\partial v}{\partial x} - \frac{\partial u}{\partial x} \frac{\partial v}{\partial y} \right) + \frac{1}{2} \left( \frac{\partial u}{\partial x} + \frac{\partial v}{\partial y} \right)^2 + \frac{1}{2} \left| \frac{\partial u}{\partial x} + \frac{\partial v}{\partial y} \right| \sqrt{\left( \frac{\partial u}{\partial x} - \frac{\partial v}{\partial y} \right)^2 + \left( \frac{\partial u}{\partial y} + \frac{\partial v}{\partial x} \right)^2} \quad (4.12)$$

Hence, in order to accurately capture the primary vortex structures during the transient event a threshold value of  $\lambda_2 = -20$  allows effective removal of the small-scale background structures in the flow field.

Identifying the primary vortex structures further allows tracking the vortex core centers in time domain. The vortex core centre is defined by the spatial location where the highest negative magnitude of  $\lambda_2$  occurs locally in the vicinity of the primary vortex structure indicating maximum vortex strength about that spatial location (figure 4.10). In the following figures (4.11 to 4.14) the vortex core trajectory of primary vortex core is presented. The horizontal location ( $x_c$ ) and time( $t$ ) on the abscissa of the plot is subtracted by the location and time corresponding to touchdown which allows all the vortex trajectories to start from the nearly similar locations. At the *DS* a sudden plunge in the elevation of the vortex core between  $(t - t_{td})/T_0 = 0-1$  is seen consistently for all the cases in figure (4.12). The disparity in the vertical elevations of the trajectories can be attributed to the influence of the *ABL* flow. The lift up of the vortex core at the *DS* starts at  $(t - t_{td})/T_0 = 1$  and the ascent is steeper for the cases with the R-B as the *ABL*. After the vortex cores reaches a maximum elevation the vortex core staggers at a constant elevation from ground before dissipating with the surrounding flow. The vortex core trajectories at the *US* as shown in figure (4.13) reveal that the vortex core travels vertically downward without significant variation in its horizontal location nearly until the point of minimum  $y_c/R_0$  as seen for each case in the plot showing its temporal evolution (figure 4.14). This occurs before the vortex core returns to a constant elevation and hence dissipates further.



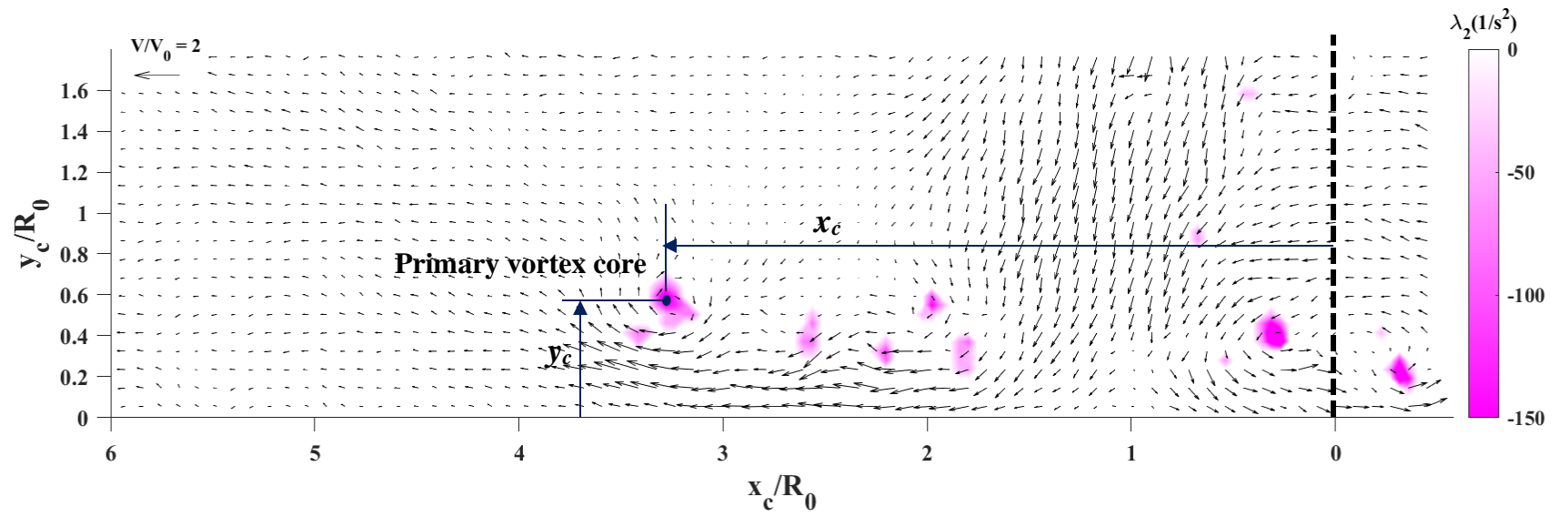
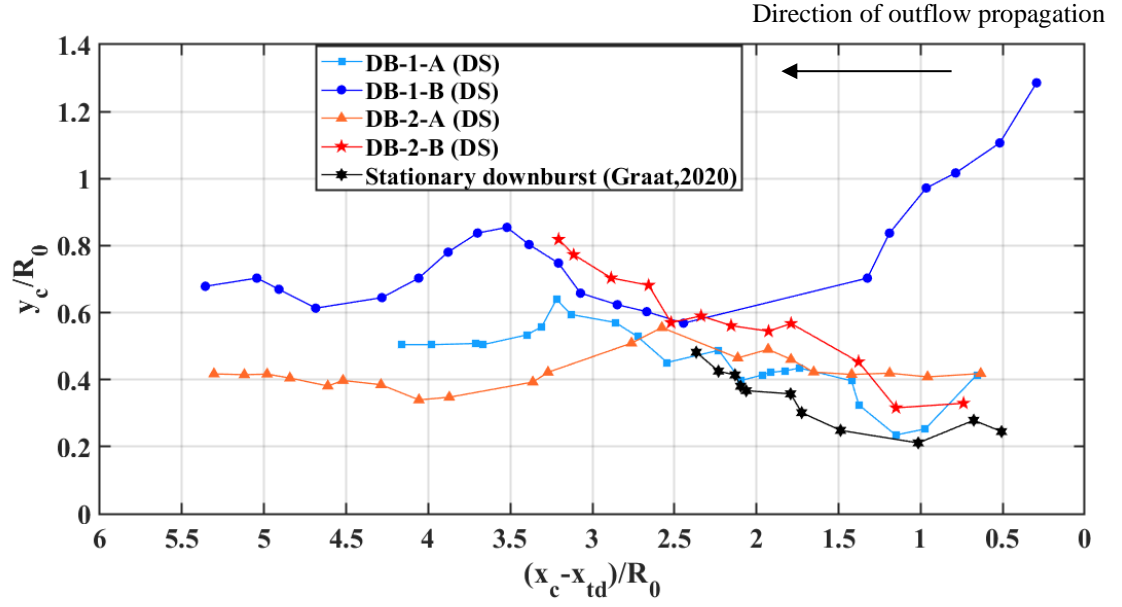
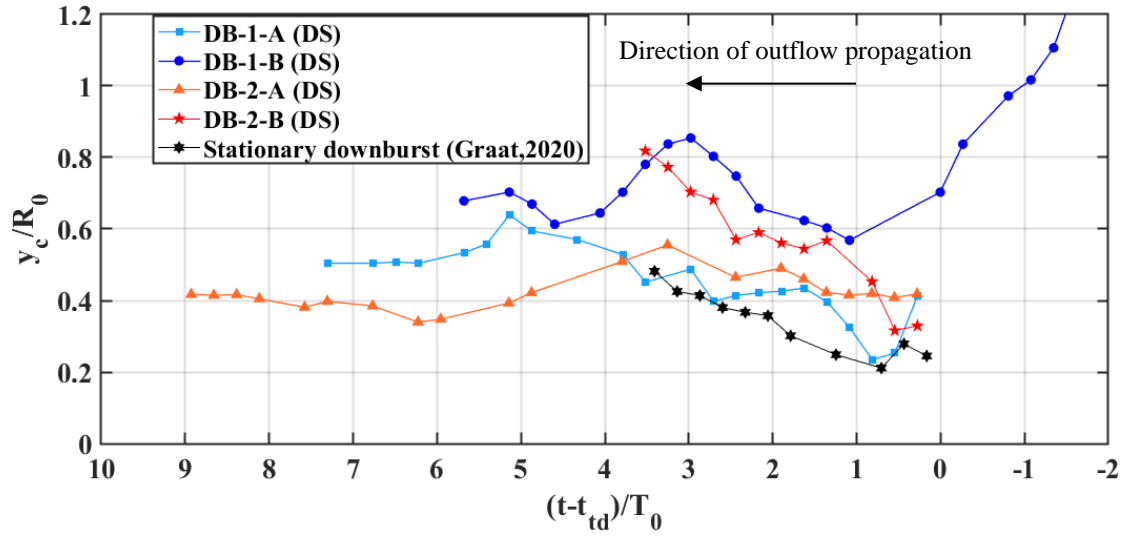


Figure 4.10 Definition of the vortex core using local maximum negative value of  $\lambda_2$  criterion for DB-1-A



**Figure 4.11** Trajectory of the primary vortex core in spatial domain during its evolution in time at the *DS*



**Figure 4.12** Temporal evolution of the height of the vortex core ( $y_c$ ) at *DS*

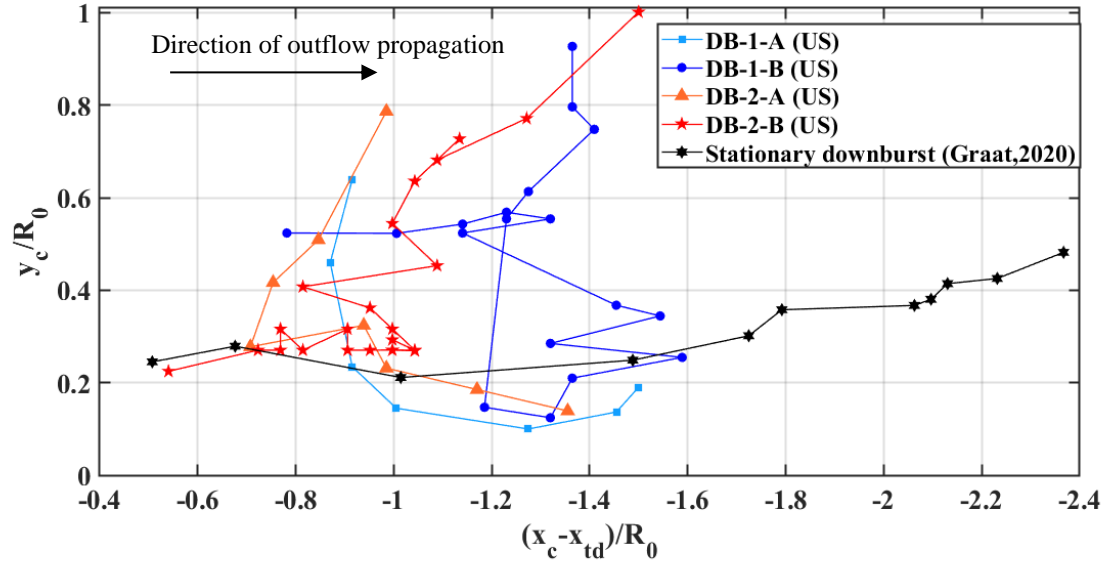


**Figure 4.13** Trajectory of the primary vortex core in spatial domain during its evolution in time at the *US*

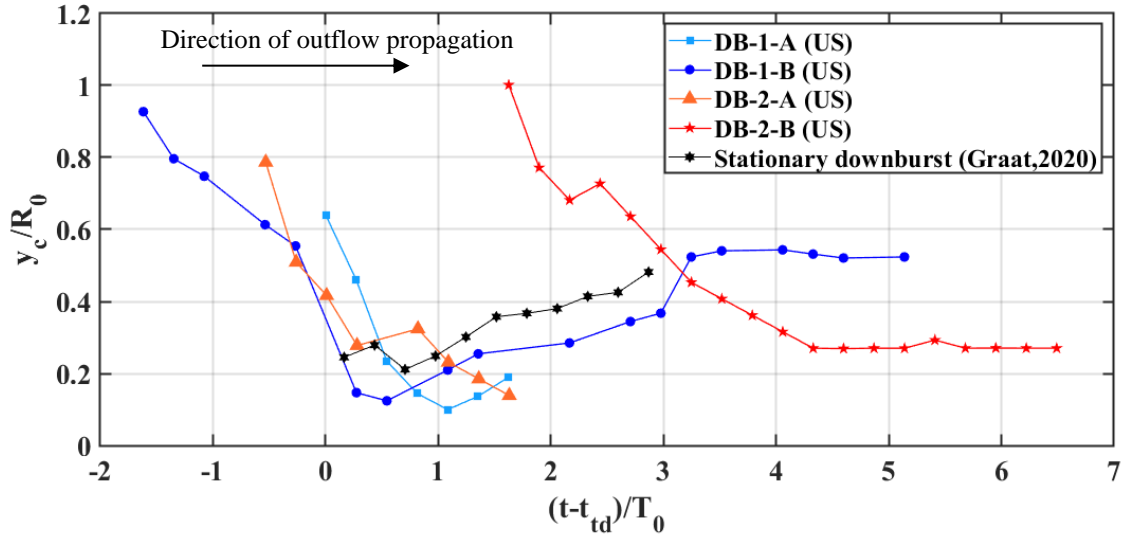


**Figure 4.14** Temporal evolution of the height of the vortex core ( $y_c$ ) at the *US*

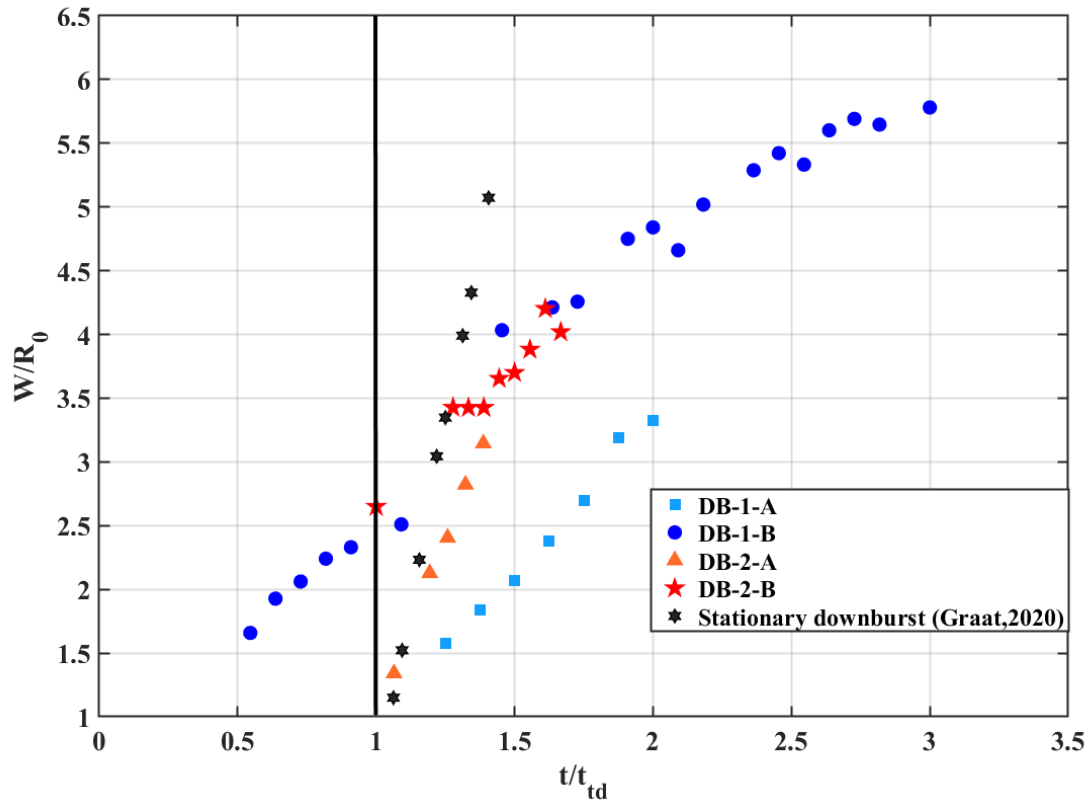


**Figure 4.15 Evolution of horizontal separation distance between the primary vortex core centers at the *DS* and *US***

The figure (4.15) shows the evolution of the horizontal separation distance ( $W$ ) between the primary vortex core centers at the *DS* and *US* with time since the downdraft touches the ground. At any time, the separation distance can be defined as the horizontal distance between the  $x$ -locations of primary vortex core centers at the *DS* and *US*. This gives an approximate realization of the spread of the outflow in the measurement plane. The separation distance ( $W$ ) shows a nearly linear trend for all the downburst events. For the stationary downburst event assuming symmetrical flow field on the either sides, the separation distance ( $W$ ) increases with a larger slope during the event. For the travelling downburst cases the vortex at *DS* side travels faster in radial direction compared to the vortex at the *US*. Also, the separation distance is commensurate with vortex strength at each side and intensity of the *ABL* flow. The downburst events DB-1-A and DB-2-A have a separation distance of approximately  $1.5R_0$  just after touchdown occurs. For DB-2-A the separation distance increases with nearly similar slope as for the stationary downburst

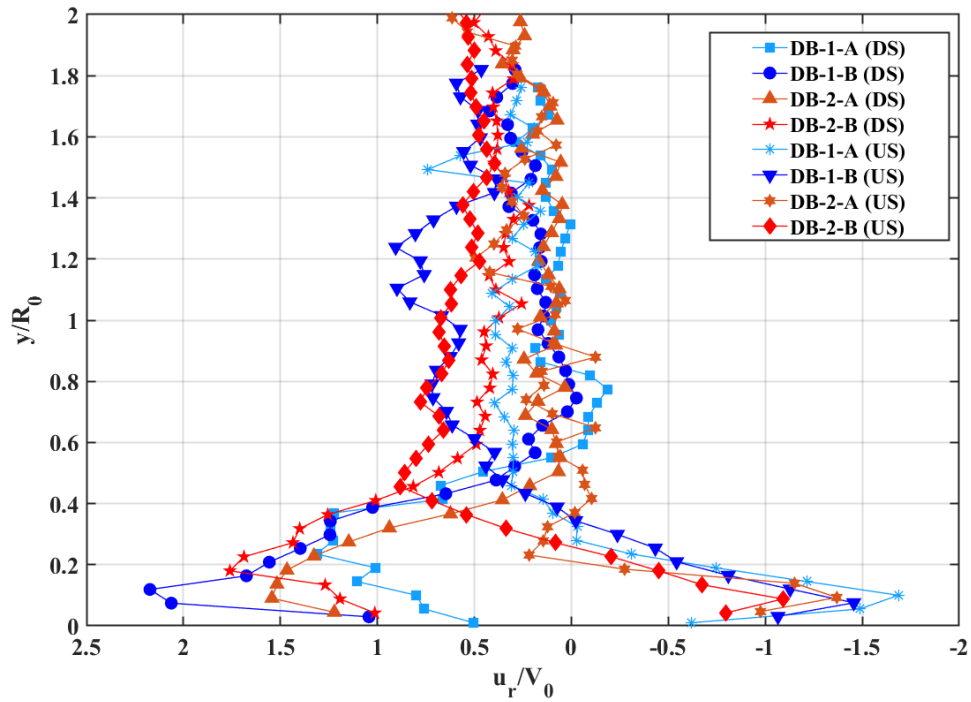
(symmetrical). The downburst events associated with the R-B *ABL* flow (DB-1-B and DB-2-B) display almost identical separation distances since the touchdown occurs, the separation distance starts from  $2.5 R_0$  at touchdown with a smaller slope as compared to the stationary downburst event. It should be noted that in order to obtain these separation distances the primary vortices need to exist at both *DS* and *US* at the same time instant, which further limits the number of data points obtained for the separation distances in time. Moreover, for the DB-1-A and DB-2-A events the primary vortex at *US* moves outside the measurement plane and hence becomes untraceable after that.

#### 4.2.3 Peak Velocity characteristics

Table (4.5) includes averaged peak instantaneous radial velocities observed during the course of the downburst events. The peak radial velocities were observed consistently below the core of the primary vortex and were determined by numerically scrutinizing the peak from the velocity field at the *DS* and *US* of the event. The peak velocity characteristics are averaged for 2 identical runs for each event case. The temporally ensemble averaged velocity vector field for two identical runs corresponding to discrete cases using an averaging window of  $t = 0.3 s$ , allows the instantaneous velocity profiles to be within 25% of the ensemble average for all the events giving an indication that the repetitions for the downburst cases have identical flow field (Appendix E). Moreover, the quantities relating to the peak velocity are normalized by the Lundgren scaling parameters as,  $R_0 = 4.42 cm$ ;  $V_0 = 12.09 cm/s$ ;  $T_0 = 0.37 s$ .

**Table 4-5 Peak radial velocity characteristics for travelling downburst**

Travelling Downburst cases			$\frac{u_p}{V_0}$	$\frac{x_p}{R_0}$	$\frac{y_p}{R_0}$	$\frac{y_p}{H_0}$	$\frac{t_{\max}}{T_0}$	$\frac{u_{r,p(DS)}}{u_{r,p(US)}}$
1	DB-1-A (Averaged)	DS	1.87	3.57	0.30	0.13	6.08	1.10
		US	1.69	-0.45	0.10	0.04	4.73	
2	DB-1-B (Averaged)	DS	2.17	3.78	0.12	0.05	6.68	1.48
		US	1.46	0.20	0.07	0.03	5.54	
3	DB-2-A (Averaged)	DS	1.75	2.39	0.16	0.05	5.81	1.27
		US	1.37	-0.19	0.09	0.03	5.81	
4	DB-2-B (Averaged)	DS	2.00	4.04	0.13	0.04	6.08	1.83
		US	1.09	1.70	0.09	0.03	7.36	
5	Stationary DB (Graat, 2020)	LH	1.96	1.22	0.11	0.04	5.95	1.00
		RH	1.95	-2.13	0.21	0.07	7.84	

**Figure 4.16 Peak horizontal velocity profiles for the DS and the US side of the downburst outflow normalized using Lundgren scaling parameters**

In general, for all the downburst cases higher peak radial velocities occurred at *DS* compared to the corresponding peaks at *US* as depicted by the ratio  $\frac{u_{r,p(DS)}}{u_{r,p(US)}}$  in table (4.5) (figure 4.16). This is an overall effect of amplification in the momentum of the outflow at the *DS* and the loss of momentum at the *US* since the outflow and *ABL* flow in opposite flow direction. Moreover, this effect is more pronounced for the cases with the R-B as the background flow (DB-1/2-B) and for the cases with the higher release height (DB-2-A/B).

#### 4.2.4 Comparison of the peak radial velocities at the downstream side (DS):

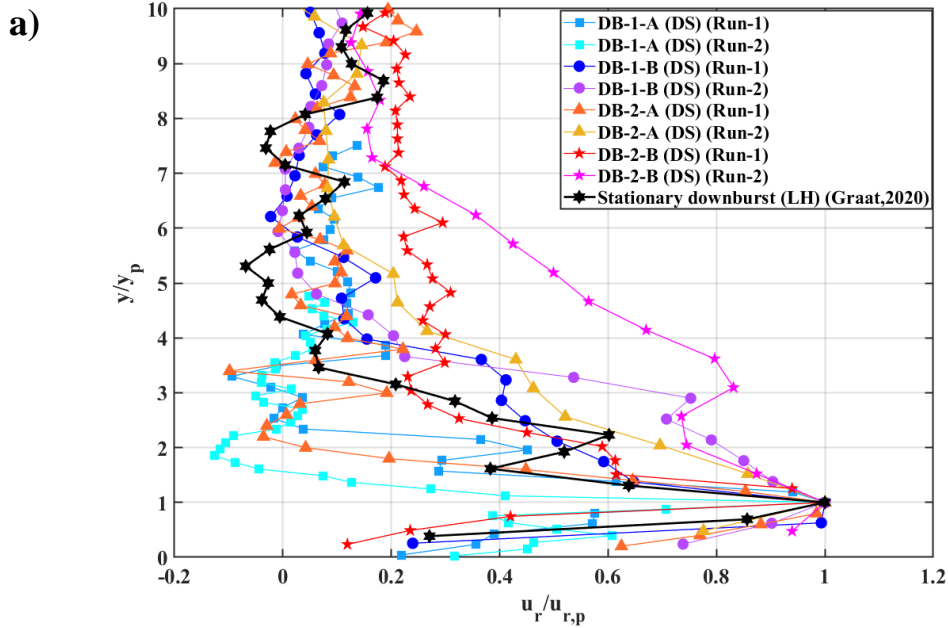
The DB-1-B(*DS*) event produced the highest peak velocity among all the cases at the downstream side (*DS*) of the event. The effect of the higher flow velocity associated with the cases having R-B ( $U_\infty = 6.65 \text{ cm/s}$ ) as the *ABL* simulation produced higher peaks compared to the cases with the R-A ( $U_\infty = 3.04 \text{ cm/s}$ ) *ABL* flow case. While comparing the peak radial velocities for the cases with identical release height and variable *ABL* flow cases, an increase in the peak by 16.2% ( $0.30V_0$ ) from DB-1-A to DB-1-B, and by 14.6% ( $0.25V_0$ ) from DB-2-A to DB-2-B was seen. Furthermore, the comparison of the downburst events with varying release height revealed that the outflows produced a lower peak radial velocity for the cases pertaining to the higher release height ( $H_0=14.5 \text{ cm}$ ) with the same background flow, and hence the downburst events with the lower release height ( $H_0=10.5 \text{ cm}$ ) DB-1-A and DB-1-B generated increased peaks by 7.15% ( $0.12V_0$ ) and 8.64% ( $0.17V_0$ ) when compared to DB-2-A and DB-2-B, respectively. This feature can be attributed to the loss of momentum associated with the vertical velocities of the downdraft emerging from the cylinder at a higher release height before touchdown, hence weakening the downdraft and producing a weaker outflow after touchdown.

For the downburst events with the release height of  $H_0=14.5 \text{ cm}$  (DB-2-A(*US*) & DB-2-B(*US*)) the peak radial velocity is observed at  $4.64T_0$  and  $3.21T_0$  time units after touchdown, whereas the peaks occur at  $5.03 T_0$  and  $5.45 T_0$  time units after touchdown for the DB-1-A & DB-1-B, respectively. The peaks for the DB-2-A/B cases occurs right

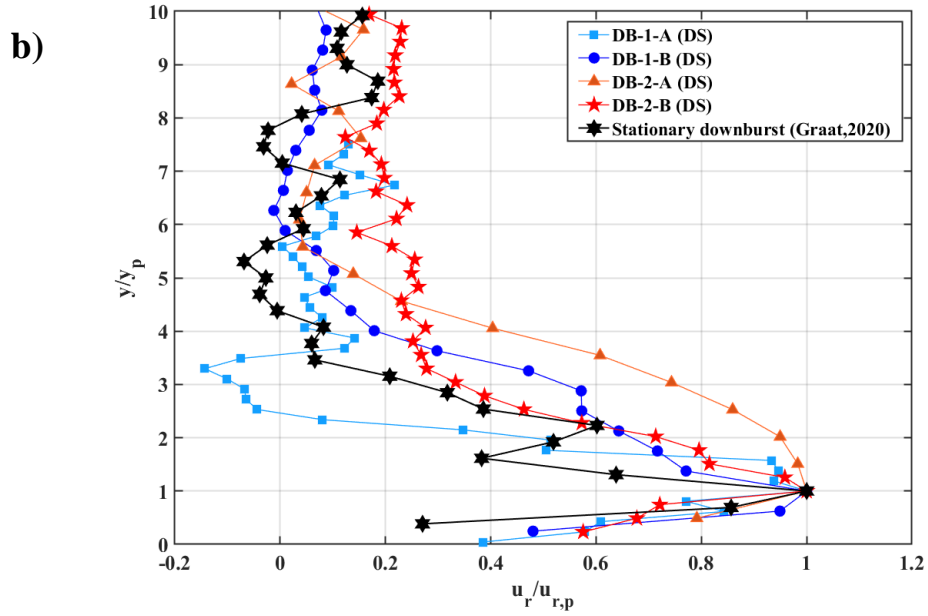
after touchdown when the vortex takes a dip in elevation during the stretching phase of the vortex structure in the radial direction. While for the DB-1-A/B cases the peaks are seen while the vortex structure is well formed and propagating radially with nearly constant elevation from ground.

#### 4.2.5 Comparison of the peak radial velocities at the upstream side (US):

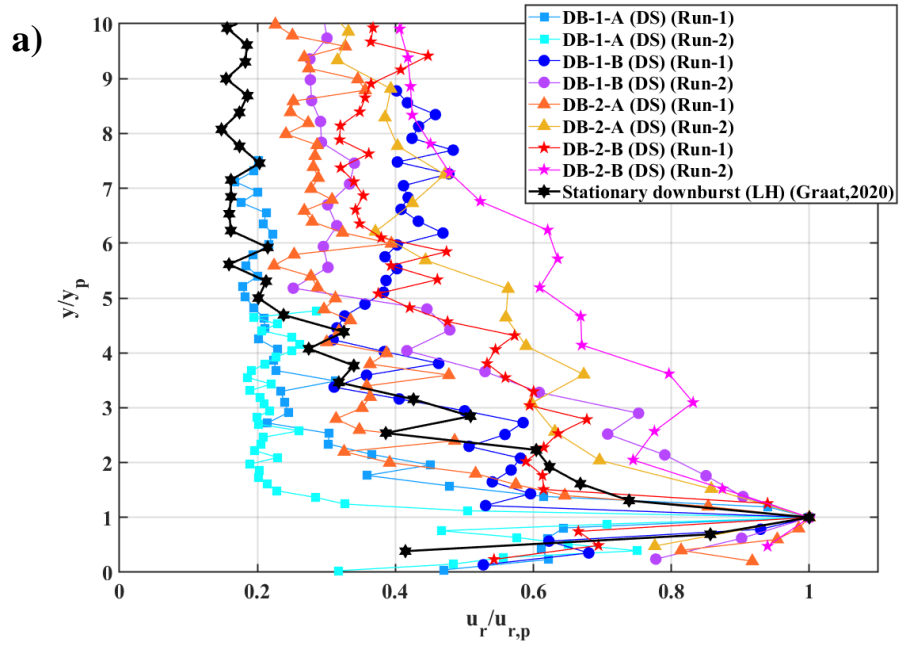
With the vortex outflow travelling in opposite direction to the *ABL* flow at the *US* side the downburst cases with R-A ( $U_\infty = 3.04 \text{ cm/s}$ ) as the *ABL* generated peak radial velocity of higher magnitude compared to the downburst cases with R-B ( $U_\infty = 6.65 \text{ cm/s}$ ) for the same release heights. An increase in the peak radial velocity appeared for the DB-1-A(US) and DB-2-A(US) by 15.7% ( $0.23V_0$ ) and 25.6% ( $0.28V_0$ ) compared to the respective cases with the same release height DB-1-B(US) and DB-2-B(US). Similar to the influence of the release height for the peak at the *DS* of the outflow peaks larger in magnitude occurred for the cases with release height  $H_0 = 10.5 \text{ cm}$ .

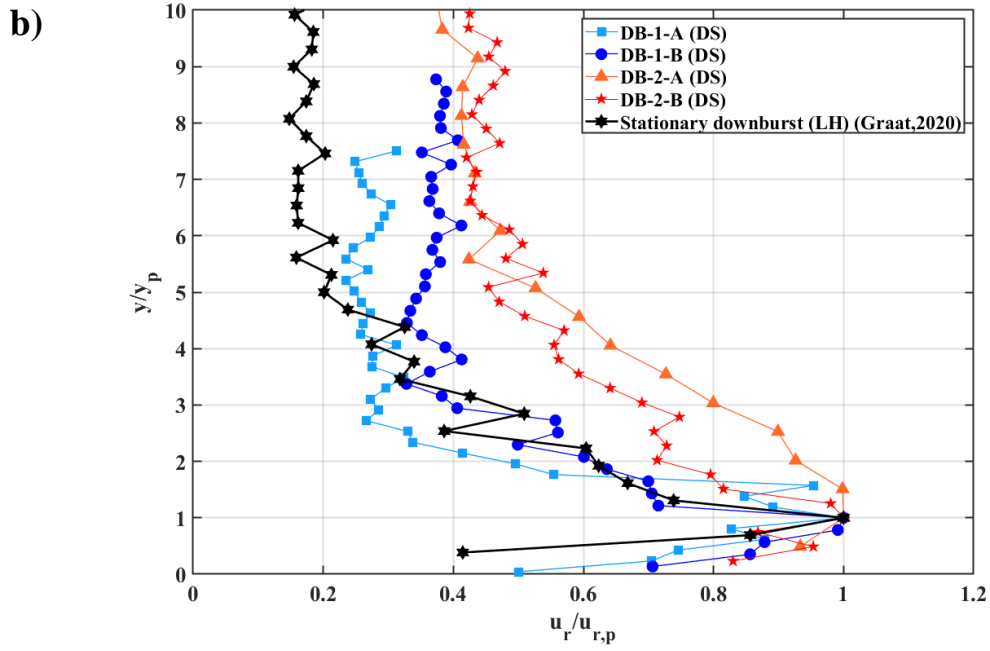




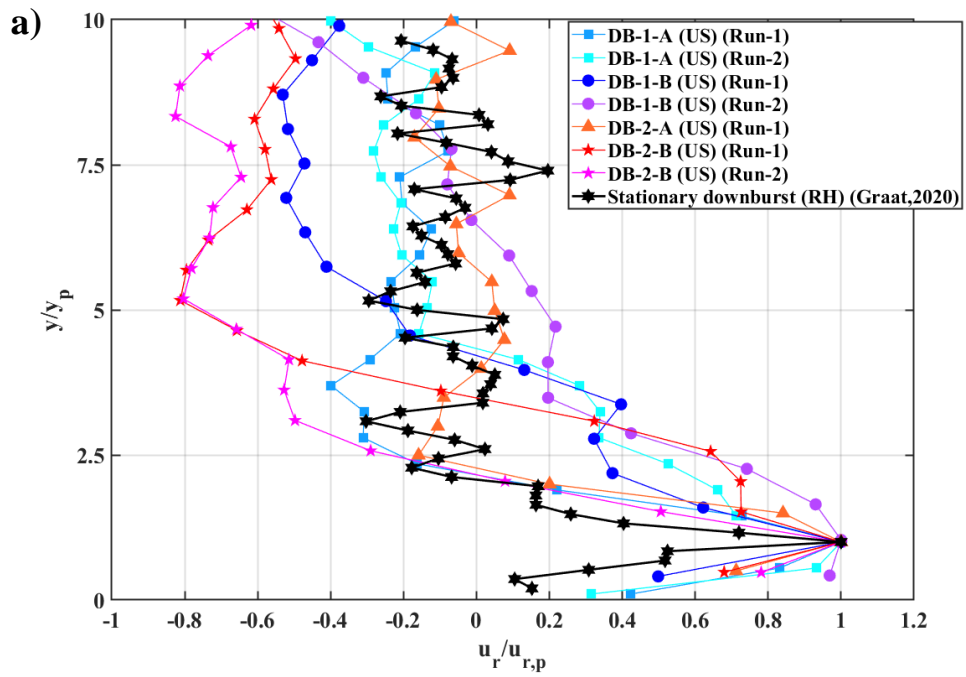


**Figure 4.17** Instantaneous peak horizontal velocity profiles for the downburst outflows at the downstream side normalized using the maximum values a) distinct runs b) averaged for two runs





**Figure 4.18 Enveloped peak horizontal velocity profiles for the downburst outflows at the downstream side normalized using the maximum values a) distinct runs b) averaged for two runs**



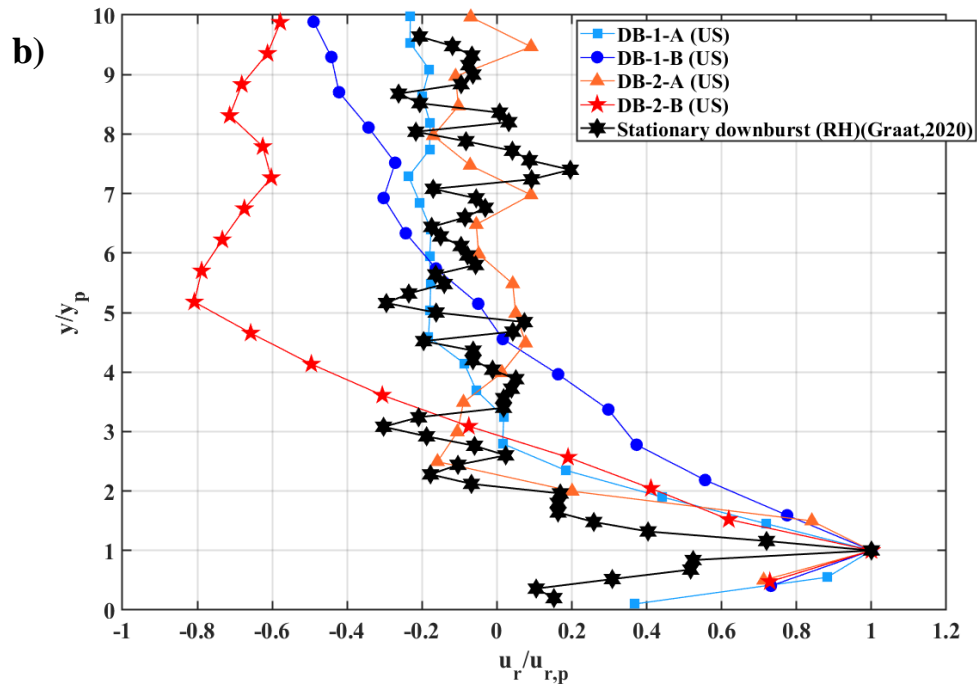


**Figure 4.19** Instantaneous peak horizontal velocity profiles for the downburst outflows at the upstream side normalized using the maximum values a) distinct runs  
b) averaged for two runs

#### 4.2.6 Comparison with stationary downburst release experiment

The downburst release experiments conducted by Alahyari (1995) revealed that the vortex characteristics and the peak velocity characteristics after touchdown were not sensitive to the change of cylinder release height. This allows comparison of the stationary downburst release experiment ( $H_0/R_0=3.08$ ) from Graat (2020) with the travelling downburst cases in the present study. Moreover, the same experimental apparatus and release mechanism as Graat (2020) is used in the present study allowing reliable comparison between both cases. The peak radial velocity characteristics are listed in table (4.6) following to its discussion in this section.

**Table 4-6 Peak radial velocity characteristics for travelling downburst compared against the stationary downburst event**

Travelling Downburst cases			$\frac{u_p}{V_0}$	% Diff. from Stationary DB	$\frac{x_p}{R_0}$	$\frac{y_p}{R_0}$	$\frac{y_p}{H_0}$	$\frac{t_{\max}}{T_0}$
1	<b>DB-1-A (Averaged)</b>	DS	1.87	4.59%	3.57	0.30	0.13	6.08
		US	1.69	13.3%	-0.45	0.10	0.04	4.73
2	<b>DB-1-B (Averaged)</b>	DS	2.17	10.8%	3.78	0.12	0.05	6.68
		US	1.46	25.1%	0.20	0.07	0.03	5.54
3	<b>DB-2-A (Averaged)</b>	DS	1.75	10.9%	2.39	0.16	0.05	5.81
		US	1.37	29.7%	-0.19	0.09	0.03	5.81
4	<b>DB-2-B (Averaged)</b>	DS	2.00	2.04%	4.04	0.13	0.04	6.08
		US	1.09	44.1%	1.70	0.09	0.03	7.36
5	<b>Stationary DB</b>	LH	1.96	-	1.22	0.11	0.04	5.95
		RH	1.95	-	-2.13	0.21	0.07	7.84

An increase in instantaneous peak radial velocity at the downstream side (*DS*) was only observed for the case of DB-1-B by  $0.21V_0$  (10.8 %) when compared to the peak of the stationary downburst case (Table (4.6)). However, the peak for the stationary downburst was similar to DB-1-A (*DS*) & DB-2-B (*DS*) case where the percentage change from the stationary case was lower than the total experimental uncertainty and hence it can be deemed to have no difference in peak radial velocity magnitude. The peak radial velocities at the upstream side (*US*) for all the travelling downburst cases were found to be lower compared to the stationary case due continuous momentum loss from the radial outflow due to the oncoming *ABL* flow. The shape of the peak velocity profile for the stationary downburst case and the travelling downburst event (figures 4.17-4.19) apparently seem to have a similar structure, however, low spatial resolution using the *PIV* technique limits this proposition.

#### 4.2.7 Peak wind speeds at full-scale and comparison with previous studies and field data

The downbursts modelled in the present study are embedded inside a scaled *ABL* and hence the full-scale quantities for the downburst event are governed with the same model scale factor as that of the *ABL* in flume. For the model scale factors (1:5500 and 1:10,000 for R-A and R-B, respectively) the peak velocity data for the present study can be converted to full-scale realization using the approach of kinematic similarity by applying Froude number  $\left(\frac{V^2}{gL}\right)$  scaling (applicable to environmental flows). Applying this model similarity for the downburst cases associated with R-A and R-B *ABL* flow, the maximum peak radial velocities observed at the *DS* translate to 16.8 m/s (at 73.4m AGL and 1.5min after touchdown) for DB-1-A , and 26.2 m/s (at 52.5m AGL and 2.3min after touchdown) for DB-1-B. This corresponds closely with the maximum wind speeds observed at 2min after touchdown during the DL- 191 airplane crash (Lundgren,1992). The *JAWS* and *NIMROD* field study experiments recorded a large number of downbursts having peak windspeed in the range of 12-14m/s (Fujita,1985). A maximum peak wind speed of 32m/s at the height of 50m above ground was recorded in *NIMROD* field study, while the peaks can range to higher magnitudes going up to 67m/s recorded at Andrews AFB at 4.9m from ground (Fujita,1985). Moreover, more recent studies observed wind speeds of 15-18m/s at 20m AGL during the downburst event at Livorno, Italy (Burlando *et al.*, 2017). Moreover, implementing these model scale factors to the source parameters for the travelling downburst simulation results in the scaling of downbursts as displayed in Table 4.7. A model scale factor of 1:16000 was used in the previous studies of stationary and travelling downbursts implementing the similar cylinder release mechanism used in present work (Babaei, 2018; Graat, 2020).

**Table 4-7 Full scale values of Lundgren scaling parameters representing the travelling downburst simulation in present work**

Downburst parameters (full-scale)	Present study				Babaei (2018); Graat (2020)
	1:5500		1:10000		1:16000
	DB-1-A	DB-2-A	DB-1-B	DB-2-B	-
$H_0(km)$	0.57	0.79	1.05	1.45	1.7/2.3
$R_0(km)$	0.24		0.44		0.7

The range of cloud base heights for the downbursts recorded during *JAWS* field experiments ranged from 2-3.5 *km* (Hjelmfelt, 1987). The full-scale estimations of the release height ( $H_0$ ) for all the downburst events except DB-1-A corresponds to the cloud base heights in actual downbursts within a factor of 2. It should be noted that the full-scale release height of 0.57*km* for the DB-1-A event is far from being realistic. However, experimental and numerical studies implementing the impinging jet model as the downburst modelling technique do not confirm if the source parameters (downdraft diameter and nozzle height) used resemble reasonable full-scale events and rather focus on scaling of the near ground characteristics (Elawady *et al.*, 2017; Romanic & Hangan, 2020). It should be noted that the current study incorporates a check on the scales generated in the downburst event as well as for the generated *ABL* and the upscaled quantities lie within a factor of 2, which is novel and encouraging for such small-scale simulations.

Further, comparison of the peak velocity profiles by implementing various scaling methods is discussed. Impinging jet models use the nozzle diameter as the characteristic length scale of the downburst event. Hence, figure 4.20 shows the peak velocity profiles at the *DS* plotted against relevant past studies incorporating background *ABL* flow (Mason *et al.*, 2010; Romanic & Hangan, 2020) and field study (Fujita, 1981). This simplified scaling approach is found to be inefficient for comparison with relevant

studies. The limited temporal resolution (0.1s) in the present study is not sufficient in measuring the actual peak wind speed near ground. It is highly probable that the actual peak velocity occurred at a time instant between the sampled data points in time domain. Hence any scaling method involving usage of peak wind speed (figure (4.20 & 4.21)) results into inconsistent scaling and hence is not useful for the present case.

Lundgren scaling can be applied to buoyancy-driven dense liquid release models and use the properties of the downburst source as a form of scaling ( $R_0$ ,  $T_0$ , and  $V_0$ ). However, since the velocity outflow in the present study was significantly influenced by the background *ABL*, Lundgren scaling approach does not prove to be efficient either as it does not account for background forcing and translation (figure (4.22)). Furthermore, limited number of studies incorporating such realistic approach limits the comparison that can be made further in this section. However, a new scaling approach needs to be defined incorporating the source variable and background forcing altogether.

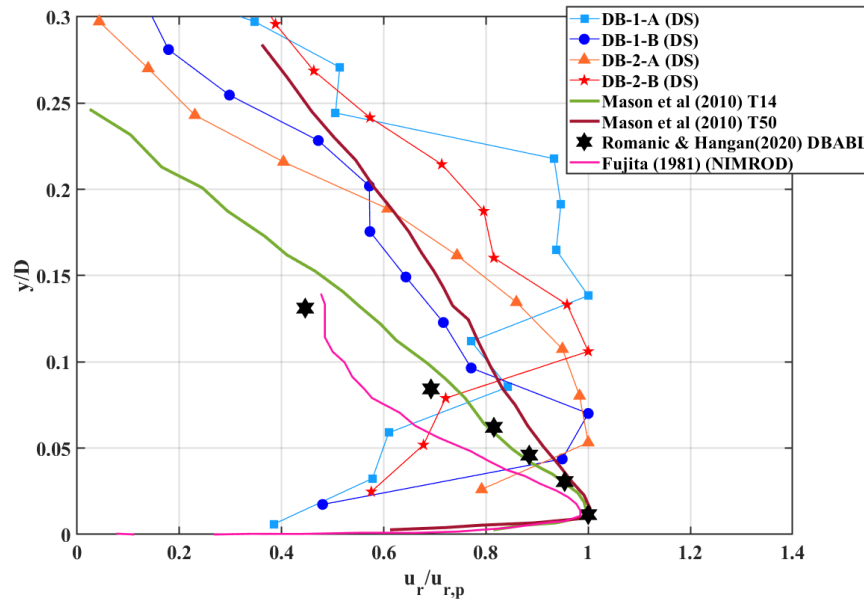


**Figure 4.20 Vertical profile of peak radial velocity employing cylinder diameter scaling**

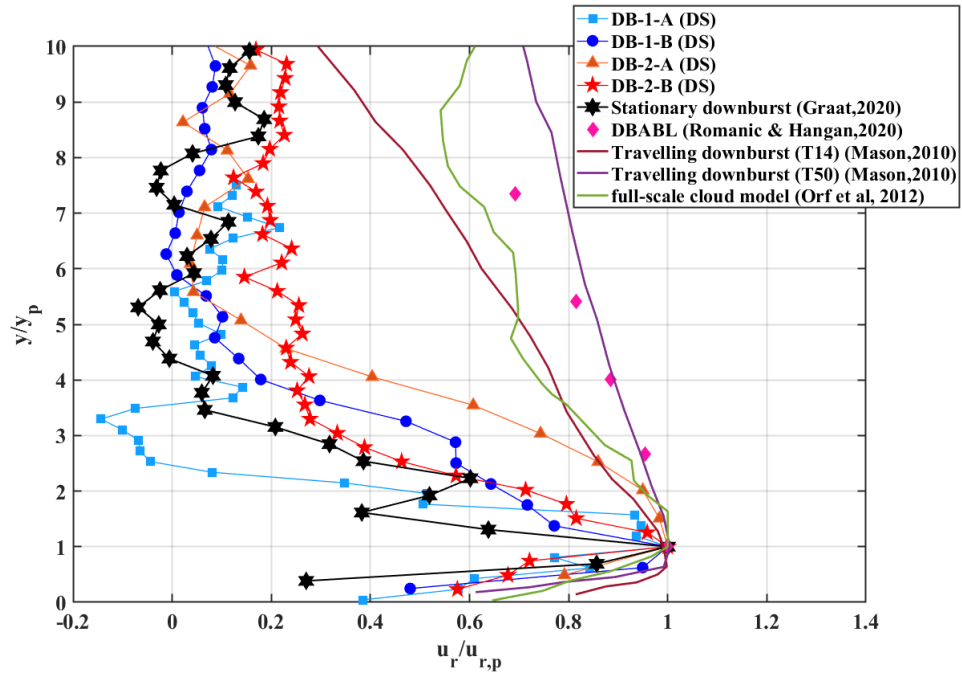


**Figure 4.21 Vertical profile of peak radial velocity normalized by corresponding peak quantities**

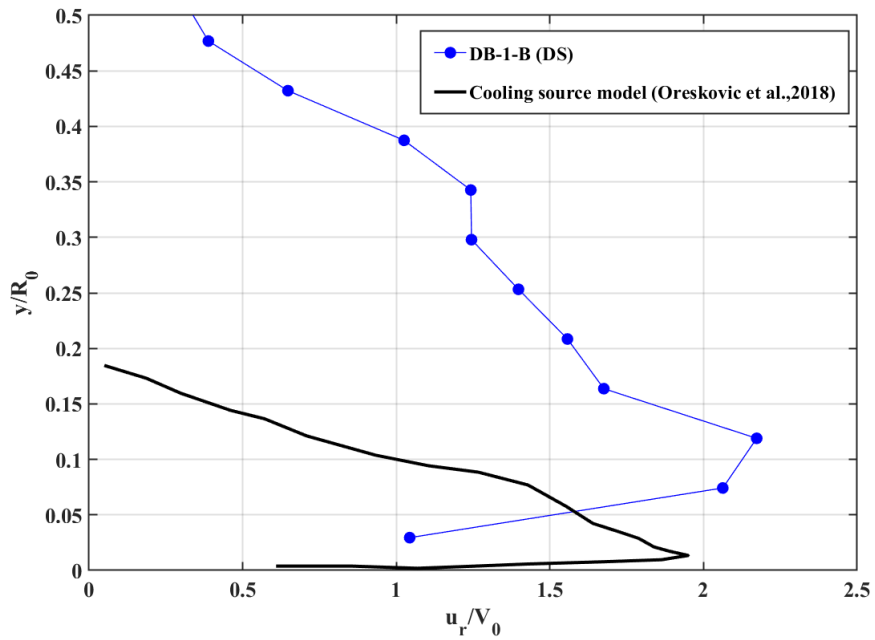


**Figure 4.22 Radial velocity profiles scaled using Lundgren Scaling parameters and compared against Cooling source model**



### 4.3 Summary:

The *ABL* simulation designed in the present study using passive turbulence generating devices proved to be partially reasonable in generating scaled *ABL* flows in an open channel flow system. The credibility of the scales generated in the *ABL* was further checked by scaling the velocity mean and turbulence characteristics with full-scale *ABL* flows. For the same roughness arrangement, the two *ABL* flow cases with varying flow speed produced *ABL* with a model scale factor of 1:5500 and 1:10,000, respectively. The translating downburst events displaying realistic transient flow-fields unequally distributed across either side of release. The peak velocities recorded allows to understand the effect of increase in background flow speed and decrease in release height is to produce stronger wind speeds in the downbursts event. However, due to the limited spatial and temporal resolution the comparison of peak velocities near ground with preexisting studies was not possible.

## Chapter 5

### 5 Conclusions and recommendations

#### 5.1 Conclusions

This research study was focused on experimentally simulating realistic density-driven (buoyancy driven) thunderstorm downbursts by embedding the translating downburst event inside a scaled atmospheric boundary layer (*ABL*). The scaled *ABL* was generated experimentally within a hydraulic flume (open channel) system by adapting the work of Standen (1972), Counihan (1973) and Cook (1978) concerning the implementation of passive turbulence generating devices such as a fence, spire array and a staggered array of roughness element over a restrictive fetch of the flow facility. The generated *ABLs* have a model scale factors of 1:5500 and 1:10,000, representing a rural type of terrain conditions (full-scale  $z_0 = 0.1m$ ;  $d_0 = 0 - 2m$ ). The downburst event adopting the density-driven model was modelled using the cylinder release mechanism as previously implemented by Babaei (2018) and Graat (2020) for studying travelling and stationary downbursts, respectively. The characterization of the velocity-field of the realistic downburst events was carried out using Particle Image Velocimetry (*PIV*) within a single vertical plane elucidating the vertical cross-section of the 3-D downburst field in the streamwise direction. The downburst release experiments were conducted by varying the cylinder-base release height ( $H_0$ ) source parameter for two normalized heights as  $H_0 / R_0 = 2.38$  and  $H_0 / R_0 = 3.28$  to understand the influence of variable source heights on the generated outflows.

The key findings from this research work are as stated:

- 1) The asymmetry (lifting of the downstream edge and contraction of the upstream end near ground) observed at the downstream and upstream side of the outflow was as observed in realistic downburst events with strong environmental perturbation.
- 2) The influence of the background *ABL* and its shear on the touchdown of the downburst outflow was observed with the downburst outflow touching the ground at a farther distance from the release reference locations, hence forming a tilted

outflow. Similar effect was seen with the increase in release height and it should be noted that the effect of increasing the release height was cumulative along with the effect of the *ABL* flow.

- 3) The downstream side of the downburst outflow produced the strongest peak radial wind speeds for all the translating downburst events compared to wind speeds at the upstream side. The highest velocity recorded was  $2.17V_0$  which translates to 26.2 m/s at full-scale.
- 4) The influence of stronger *ABL* flow and a decrease in release height was found to increase the peak velocity observed at the downstream side. Moreover, with the increase in the *ABL* flow speed and the release height the unequal momentum distribution among the downstream and upstream side was accentuated.
- 5) The previously established scaling approaches involving the only source parameters such as the downdraft diameter (Romanic *et al.*, 2020), release height, and Lundgren scaling parameters (Lundgren *et al.*, 1992) prove to be ineffective for the downburst events embedded inside a pre-existing *ABL* flow with the fact that the flow field of the downburst outflow in the present study was found significantly affected by the *ABL* flows.

## 5.2 Contributions

The experimental implementation of the density-driven downburst model translating within an *ABL* is novel and characterizes the downburst flow-field with a realistic approach for the first time. This study mainly focuses on adapting the true physics involved in a downburst event i.e., the density difference between the parent cloud and its surrounding and is devoid of any artificial forcing. This study serves as a starting point in combining the density-driven downburst modelling technique with scaled *ABL* flows to generate realistic downburst events.

## 5.3 Limitations and Challenges

The simulation of the *ABL* in the present study lacks consistent scaling of the velocity and turbulence characteristics with the full-scale studies. This is a consequence of experimental constraints like short contraction chamber, short flume fetch, and the high

turbulence intensity in the mean flow at the flume inlet. Since, some of these limitations cannot be mitigated the designed ABL simulation is considered partially reasonable.

## 5.4 Future Recommendations:

1. Improving the spatial and temporal resolution for density-driven experiments conducted in the present study to refine the observations observed from the current study recorded with limited temporal and spatial resolution.
2. Implementing *PLIF* technique to characterize the scalar density fields of the density driven downbursts embedded in *ABL* flows elucidating the complex interaction of the downburst outflow with the *ABL* before touchdown in the vertical plane. Also, this will allow investigating the temporal evolution of the radial fronts of the realistic downburst event. This method can be employed to unravel the asymmetric flow-field of such realistic downburst events in a horizontal plane.
3. Characterizing the velocity field across a horizontal plane to understand the extent of asymmetry caused to the downburst outflow from variable *ABL* flow conditions and downburst source parameters.
4. Generating a scaled urban *ABL* within the hydraulic flume system to examine the translating downburst flow field within it. The urban type of boundary layer can be generated by increasing the density of the roughness elements.
5. Adding another release cylinder to create a multiple downburst (downburst-lines) event along with translation within rural and urban type *ABLs*.

## References

- Aboshosha, H. and El Damatty, A., (2015). Dynamic response of transmission line conductors under downburst and synoptic winds. *Wind and Structures*, 21(2), pp. 241–272.
- Alahyari, A. and Longmire, E.K., (1995). Dynamics of experimentally simulated microbursts. *AIAA journal*, 33(11), pp.2128-2136.
- Anabor, V., Rizza, U., Nascimento, E.L. and Degrazia, G.A., 2011. Large-eddy simulation of a microburst. *Atmospheric Chemistry and Physics*, 11(17), pp.9323-9331.
- Anderson, J. R., Orf, L. G., & Straka, J. M. (1992). A 3-D model system for simulating thunderstorm microburst outflows. *Meteorology and Atmospheric Physics*, 49(1-4), 125-131.
- Armitt, J., & Counihan, J. (1968). The simulation of the atmospheric boundary layer in a wind tunnel. *Atmospheric Environment (1967)*, 2(1), pp.49-71.
- Babaei Koli, R., (2018). Experimental Simulation of Density-Driven Thunderstorm Downbursts. *MESc. Thesis*, Western University, London, Ontario, Canada.
- Babaei, R., Graat, K., Chan, C., & Savory, E. (2021). Experimental simulation of stationary and traveling density-driven thunderstorm downbursts using the two-fluid model. *Journal of Wind Engineering and Industrial Aerodynamics*, 211, 104553.
- Bakke, P., (1957). An experimental investigation of a wall jet. *Journal of Fluid Mechanics*, 2(5), pp.467-472.
- Barry, R. G. and Chorley, R. J., (2010). *Atmosphere, weather & climate*. Routledge, New York, pp.1-516
- Bluestein H.B., (2013). *Severe convective storms and tornadoes. Observations and Dynamics*. Springer, Chichester, UK, pp.1-456.
- Bryan, G. H., & Fritsch, J. M. (2002). A benchmark simulation for moist nonhydrostatic numerical models. *Monthly Weather Review*, 130(12), 2917-2928.
- Bradshaw, P. and Love, E.M., (1959). The normal impingement of a circular air jet on a flat surface.
- Burlando, M., Romanić, D., Solari, G., Hangan, H., & Zhang, S. (2017). Field data analysis and weather scenario of a downburst event in Livorno, Italy, on 1 October 2012. *Monthly Weather Review*, 145(9), 3507–3527.
- Cebeci, T. (2012). *Analysis of turbulent boundary layers*. Elsevier.

Cengel, Y., & Cimbala, J. (2014) Fluid Mechanics: Fundamentals and Applications, 2014. ISBN-13: 9780073380322.

Chay, M.T., Albermani, F. and Wilson, R., 2006. Numerical and analytical simulation of downburst wind loads. *Engineering Structures*, 28(2), pp.240-254.

Chay, M. T., & Letchford, C. W. (2002). Pressure distributions on a cube in a simulated thunderstorm downburst—Part A: stationary downburst observations. *Journal of Wind Engineering and Industrial Aerodynamics*, 90(7), 711-732.

Chen, Q., Zhong, Q., Qi, M., & Wang, X. (2015). Comparison of vortex identification criteria for planar velocity fields in wall turbulence. *Physics of Fluids*, 27(8), 085101.

Choi, E.C., (2004). Field measurement and experimental study of wind speed profile during thunderstorms. *Journal of wind engineering and industrial Aerodynamics*, 92(3-4), pp.275-290.

Cook, N. J. (1973). On simulating the lower third of the urban adiabatic boundary layer in a wind tunnel. *Atmospheric Environment* (1967), 7(7), 691-705.

Cook, N.J., (1978). Wind-tunnel simulation of the adiabatic atmospheric boundary layer by roughness, barrier and mixing-device methods. *Journal of Wind Engineering and Industrial Aerodynamics*, 3(2-3), pp. 157-176.

Cook, N. J. (1978). Determination of the model scale factor in wind-tunnel simulations of the adiabatic atmospheric boundary layer. *Journal of Wind Engineering and Industrial Aerodynamics*, 2(4), 311-321.

Counihan, J. (1971). Wind tunnel determination of the roughness length as a function of the fetch and the roughness density of three-dimensional roughness elements. *Atmospheric Environment* (1967), 5(8), 637-642.

Counihan, J. (1973). Simulation of an adiabatic urban boundary layer in a wind tunnel. *Atmospheric Environment* (1967), 7(7), pp. 673-689.

Counihan, J.O., (1975). Adiabatic atmospheric boundary layers: a review and analysis of data from the period 1880–1972. *Atmospheric Environment*, 9(10), pp. 871-905.

Craft, T.J., Graham, L.J.W. and Launder, B.E., (1993). Impinging jet studies for turbulence model assessment—II. An examination of the performance of four turbulence models. *International Journal of Heat and Mass transfer*, 36(10), pp. 2685-2697.

Das, K.K., Ghosh, A.K. and Sinhamahapatra, K.P., 2010. Investigation of the axisymmetric microburst flow field. *Journal of Wind Engineering*, 7, pp.1-15.

Dempsey, D. and White, H., (1996). Winds wreak havoc on lines. *Transmission and Distribution World*, 48(6), pp.32-37.

Djenidi, L., Elavarasan, R., & Antonia, R. A. (1999). The turbulent boundary layer over transverse square cavities. *Journal of Fluid Mechanics*, 395, 271-294.

Durañona, V., Sterling, M. and Baker, C.J., (2007). An analysis of extreme non-synoptic winds. *Journal of wind engineering and industrial aerodynamics*, 95(9-11), pp.1007-1027.

Doviak, R. J., Ray, P. S., Strauch, R. G., & Miller, L. J. (1976). Error estimation in wind fields derived from Dual-Doppler Radar measurement. *Journal of Applied Meteorology*, 15(8), 868–878.

Eilts, M.D. and Doviak, R.J., (1987). Oklahoma downbursts and their asymmetry. *Journal of Applied Meteorology and Climatology*, 26(1), pp.69-78.

Elawady, A., Aboshosha, H., El Damatty, A., Bitsuamlak, G., Hangan, H. and Elatar, A., (2017). Aero-elastic testing of multi-spanned transmission line subjected to downbursts. *Journal of Wind Engineering and Industrial Aerodynamics*, 169, pp.194-216.

ESDU (1985). Characteristics of atmospheric turbulence near the ground. Part II: single point data for strong winds (neutral atmosphere. Data Item 852020, *Engineering Sciences Data Unit International*

ESDU (1993). Strong winds in the atmospheric boundary layer. Part 1: mean-hourly wind speeds. Item No. 82026, ESDU International, London. pp. 1-61.

Fage, A., & Preston, J. H. (1941). On transition from laminar to turbulent flow in the boundary layer. *Proceedings of the Royal Society of London. Series B, Biological Sciences*, 178(973), 201.

Fujita, T. T., and Srivastava, R. C., (1977). Project NIMROD (First report): University of Chicago, pp. 1-12.

Fujita, T.T., (1981). Tornadoes and downbursts in the context of generalized planetary scales. *Journal of Atmospheric Sciences*, 38(8), pp.1511-1534.

Fujita, T.T., (1985). The downburst: Microburst and macroburst. SMRP Research Paper 210, University of Chicago, 122 pp. [NTIS PB85-148880].

Fujita, T.T., (1992). The mystery of severe storms. WRL Research Paper 239, University of Chicago, 298 pp. [NTIS PB 92-182021].

Gast, K.D., Schroeder, J.L., (2003). Supercell rear-flank downdraft as sampled in the 2002 Thunderstorm Outflow Experiment. In: *Proceedings of the 11th International Conference on Wind Engineering*, Lubbock.

Geerts, B., (2001). Estimating downburst-related maximum surface wind speeds by means of proximity soundings in New South Wales, Australia. *Weather and forecasting*, 16(2), pp.261-269.

Glauert, M.B., (1956). The wall jet. *Journal of Fluid Mechanics*, 1(6), pp.625-643.

Graat, Kyle, "Experimental Modelling of Downburst and Downburst line Outflows" (2020). *MESc. Thesis*, Western university, London, Ontario, Canada.

Grass, A. J. (1971). Structural features of turbulent flow over smooth and rough boundaries. *Journal of Fluid Mechanics*, 50(2), 233–255.

Guo, X., Niino, H. and Kimura, R., 1999. Numerical modeling on a hazardous microburst-producing hailstorm. In *Towards Digital Earth, Proceedings of the International Symposium on Digital Earth*, pp. 383-398.

Hjelmfelt, M. R. (1987). The microbursts of 22 June 1982 in JAWS. *Journal of the Atmospheric Sciences*, Vol. 44, 1646–1665.

Hjelmfelt, M. R. (1988). Sturcture and life cycle of microbursts outflows observed in Colorado. *Journal of Applied Meteorology*, 27, 900–927.

Hjelmfelt, M.R., Roberts, R.D., Orville, H.D., Chen, J.P. and Kopp, F.J., (1989). Observational and numerical study of a microburst line-producing storm. *Journal of the Atmospheric Sciences*, 46(17), pp.2731-2744.

Hoxey, R., Robertson, A., Toy, N., Parke, G.A.R. and Disney, P., (2003). Design of an experimental arrangement to study the wind loads on transmission towers due to downbursts. *Transactions on The Built Environment*, 71, pp. 1-10.

Jackson, P. S. (1981). On the displacement height in the logarithmic velocity profile. *Journal of Fluid Mechanics*, 111, 15-25.

Järvi, L., Punkka, A.J., Schultz, D.M., Petäjä, T., Hohti, H., Rinne, J., Pohja, T., Kulmala, M., Hari, P. and Vesala, T., (2007). Micrometeorological observations of a microburst in southern Finland. In *Atmospheric Boundary Layers*, Springer, New York, NY. pp. 187-203.

Kaimal, J.C. and Finnigan, J.J., (1994). Atmospheric boundary layer flows: their structure and measurement. Oxford University Press, New York, pp.1-290.

Khadivi, Taravat, "Experimental and Numerical Study of Flow Structures Associated with Low Aspect Ratio Elliptical Cavities" (2012). *Electronic Thesis and Dissertation Repository*. 462.

Kim, J. and Hangan, H., (2007). Numerical simulations of impinging jets with application to downbursts. *Journal of Wind Engineering and Industrial Aerodynamics*, 95(4), pp.279-298.



- Knowles, K. and Myszkowski, M., (1995). The Turbulent, Radial Wall Jet: Effect of Impinging Jet Conditions. *In Advances in Turbulence V*, Springer, Dordrecht. pp. 271-275.
- Knupp, K.R., (1989). Numerical simulation of low-level downdraft initiation within precipitating cumulonimbi: Some preliminary results. *Monthly Weather Review*, 117(7), pp.1517-1529.
- Letchford, C. W., & Chay, M. T. (2002). Pressure distributions on a cube in a simulated thunderstorm downburst. Part B: moving downburst observations. *Journal of Wind Engineering and Industrial Aerodynamics*, 90(7), 733-753.
- Li, C., Li, Q.S., Xiao, Y.Q. and Ou, J.P., (2012). A revised empirical model and CFD simulations for 3D axisymmetric steady-state flows of downbursts and impinging jets. *Journal of Wind Engineering and Industrial Aerodynamics*, 102, pp.48-60.
- Lin, W.E. and Savory, E., (2006). Large-scale quasi-steady modelling of a downburst outflow using a slot jet. *Wind & Structures*, 9(6), pp.419-440.
- Lin, W.E., Orf, L.G., Savory, E. and Novacco, C., (2007). Proposed large-scale modelling of the transient features of a downburst outflow. *Wind and Structures*, 10(4), pp.315-346.
- Lundgren, T. S., Yao, J., & Mansour, N. N. (1992). Microburst modelling and scaling. *Journal of Fluid Mechanics*, 239, 461-488.
- Macdonald, R. W., Griffiths, R. F., & Hall, D. J. (1998). An improved method for the estimation of surface roughness of obstacle arrays. *Atmospheric Environment*, 32(11), 1857-1864.
- McCarthy, J. and Wilson, J.W., (1986). Classify, locate and avoid wind shear (CLAWS) project at Denver's international airport: operational testing of terminal weather hazard warnings with emphasis on microburst wind shear. *American Institute of Aeronautics and Astronautics Monographs*, 32, pp.17-26.
- McCarthy, P. and Melsness, M., (1996). Severe weather elements associated with September 5, 1996 hydrotower failures near Grosse Isle, Manitoba, Canada. Manitoba Environmental Service Centre, Environment Canada.
- McCann, D.W., (1994). WINDEX—A new index for forecasting microburst potential. *Weather and forecasting*, 9(4), pp.532-541.
- McConville, A. C., Sterling, M., & Baker, C. J. (2009). The physical simulation of thunderstorm downbursts using an impinging jet. *Wind and structures*, 12(2), pp.133-149.
- Mason, M. S., Letchford, C. W., & James, D. L. (2005). Pulsed wall jet simulation of a stationary thunderstorm downburst, Part A: Physical structure and flow field

characterization. *Journal of Wind Engineering and Industrial Aerodynamics*, 93(7), 557-580.

Mason, M.S., Wood, G.S. and Fletcher, D.F., (2009). Numerical simulation of downburst winds. *Journal of Wind Engineering and Industrial Aerodynamics*, 97(11-12), pp.523-539.

Nechaj, P., Gaál, L., Bartok, J., Vorobyeva, O., Gera, M., Kelemen, M., and Polishchuk, V., (2019). Monitoring of low-level wind shear by ground-based 3D lidar for increased flight safety, Protection of Human Lives and Health. *International Journal of Environmental Research and Public Health*, 16, pp. 1–26.

Nicholls, M., Pielke, R. and Meroney, R., (1993). Large eddy simulation of microburst winds flowing around a building. *Journal of Wind Engineering and Industrial Aerodynamics*, 46, pp.229-237.

Ohno, H., Suzuki, O., Nirasawa, H., Yoshizaki, M., Hasegawa, N., Tanaka, Y., Muramatsu, Y. and Ogura, Y., (1994). Okayama Downbursts on 27 June 1991 Downburst Identifications and Environmental Conditions. *Journal of the Meteorological Society of Japan*. Ser. II, 72(2), pp.197-222.

Oreskovic, C. (2016). Numerical investigation of full scale thunderstorm downbursts: A parametric study and comparison to meteorological model. *MESc. Thesis*, Western University, London, Ontario, Canada.

Oreskovic, C., Orf, L. G., & Savory, E. (2018). A parametric study of downbursts using a full-scale cooling source model. *Journal of Wind Engineering and Industrial Aerodynamics*, 180, 168-181.

Orf, L.G., Anderson, J.R. and Straka, J.M., (1996). A three-dimensional numerical analysis of colliding microburst outflow dynamics. *Journal of the Atmospheric Sciences*, 53(17), pp.2490-2511.

Orf, L.G. and Anderson, J.R., (1999). A numerical study of traveling microbursts. *Monthly Weather Review*, 127(6), pp.1244-1258.

Orf, L., Kantor, E., & Savory, E. (2012). Simulation of a downburst-producing thunderstorm using a very high-resolution three-dimensional cloud model. *Journal of Wind Engineering and Industrial Aerodynamics*, 104, 547-557.

Orville, H.D., Farley, R.D., Chi, Y.C. and Kopp, F.J., (1989). The primary cloud physics mechanisms of microburst formation. *Atmospheric Research*, 24(1-4), pp.343-357.

Orwig, K.D., Schroeder, J.L., (2007). Near-surface wind characteristics of extreme thunderstorm outflows. *Journal of Wind Engineering and Industrial Aerodynamics* 95, 565–584.

Poreh, M., and Cermak J.E., (1959). Flow characteristics of a circular submerged jet impinging normally on a smooth boundary. *In Proc. 6th Midwest Conference on Fluid Mechanics*, Austin, Texas, University of Texas, pp. 198-212.

Poreh, M., Tsuei, Y.G. and Cermak, J.E., (1967). Investigation of a turbulent radial wall jet. *Journal of Applied Mechanics, Transactions of ASME, Series E*, 34. 457-463.

Proctor, F.H., (1987). The terminal area simulation system (Vol. 1). *National Aeronautics and Space Administration, Scientific and Technical Information Branch*. Report 4046. DOT/FAA/PM-86/50,I.

Proctor, F.H., (1987). The terminal area simulation system (Vol. 2). *National Aeronautics and Space Administration, Scientific and Technical Information Branch Report* 4046.

Proctor, F.H., (1989). Numerical simulations of an isolated microburst. Part II: Sensitivity experiments. *Journal of Atmospheric Sciences*, 46(14), pp.2143-2165.

Proctor, F.H. and Bowles, R.L., (1992). Three-dimensional simulation of the Denver 11 July 1988 microburst-producing storm. *Meteorology and Atmospheric Physics*, 49(1), pp.107-124.

Proctor, F.H., (1993). Case study of a low-reflectivity pulsating microburst: numerical simulation of the Denver, 8 July 1989, storm. *17th Conference on Severe Local Storms American Meteorological Society*, 4-8 October, 17.2, pp. 677-680, St. Louis, Missouri.

Pryor, K.L., (2015). Progress and developments of downburst prediction applications of GOES. *Weather and Forecasting*, 30(5), pp.1182-1200.

Raffel, M., Willert, C. E., Scarano, F., Kähler, C. J., Wereley, S. T., & Kompenhans, J. (2018). *Particle image velocimetry: a practical guide*. Springer.

Romanic, D., & Hangan, H. (2020). Experimental investigation of the interaction between near-surface atmospheric boundary layer winds and downburst outflows. *Journal of Wind Engineering and Industrial Aerodynamics*, 205, 104323.

Rowcroft, J., (2011). Vertical wind shear profiles in downburst events and the insufficiency of wind turbine design codes. *In 14th Australasian Wind Engineering Society Workshop*. pp. 50-53.

Savory, E., Parke, G. A. R., Zeinoddini, M., Toy, N., & Disney, P., (2001). Modelling of tornado and microburst-induced wind loading and failure of a lattice transmission tower. *Engineering Structures*, 23(4), pp. 365–375.

Selvam, R.P. and Holmes, J.D., 1992. Numerical simulation of thunderstorm downdrafts. *Journal of Wind Engineering and Industrial Aerodynamics*, 44(1-3), pp.2817-2825.

Sengupta, A. and Sarkar, P.P., (2008). Experimental measurement and numerical simulation of an impinging jet with application to thunderstorm microburst winds. *Journal of Wind Engineering and Industrial Aerodynamics*, 96(3), pp.345-365.

Srivastava, R.C., (1987). A model of intense downdrafts driven by the melting and evaporation of precipitation. *Journal of Atmospheric Sciences*, 44(13), pp.1752-1774.

Standen, N. M. (1972). A spire array for generating thick turbulent shear layers for natural wind simulation in wind tunnels, *National Research Council of Canada, NAE Rep. LTR-LA-94*.

Straka, J.M. and Anderson, J.R., (1993). Numerical simulations of microburst-producing storms: Some results from storms observed during COHMEX. *Journal of Atmospheric Sciences*, 50(10), pp.1329-1348.

Stull, R. B. (2012). An introduction to boundary layer meteorology (Vol. 13). *Springer Science & Business Media*.

Sun L., Guo X., Sun Li., and Fu D., (2004). A numerical study of an airplane disasterproducing microburst on 22 June 2000 in Wuhan.Chinese. *Journal of Atmospheric Science*, 27(4), 307–323. (in Chinese).

Tachie, M. F., Bergstrom, D. J., & Balachandar, R. (2003). Roughness effects in low-Re  $\theta$  open-channel turbulent boundary layers. *Experiments in fluids*, 35(4), 338-346.

Thielicke, W., & Stamhuis, E. (2014). PIVlab–towards user-friendly, affordable and accurate digital particle image velocimetry in MATLAB. *Journal of open research software*, 2(1).

Thole, K. A., & Bogard, D. G. (1996). High freestream turbulence effects on turbulent boundary layers.

Vermeire, B. C., Orf, L. G., & Savory, E. (2011). Improved modelling of downburst outflows for wind engineering applications using a cooling source approach. *Journal of Wind Engineering and Industrial Aerodynamics*, 99(8), 801-814.

Vermeire, B.C., Orf, L.G. and Savory, E., (2011). A parametric study of downburst line near-surface outflows. *Journal of Wind Engineering and Industrial Aerodynamics*, 99(4), pp.226-238.

Wakimoto, R. M., (1982). The life cycle of thunderstorm gust fronts as viewed with doppler radar and rawinsonde data. *Monthly Weather Review*, 10, pp. 1060–1082.

Wakimoto, R.M. and Bringi, V.N., (1988). Dual-polarization observations of microbursts associated with intense convection: The 20 July storm during the MIST project. *Monthly Weather Review*, 116(8), pp.1521-1539.

White, F.M., 1979. *Fluid mechanics*. Tata McGraw-Hill Education.

Wilson, J. W., Roberts, R. D., Kessinger, C., and McCarthy, J. (1984). Microburst wind structure and evaluation of doppler radar for airport wind shear detection. *Journal of Climate and Applied Meteorology*, 23, 898–915.

Wilson, J.W., Moore, J.A., Foote, G.B., Martner, B., Rodi, A.R., Uttal, T. and Wilczak, J.M., (1988). Convection initiation and downburst experiment (CINDE). *Bulletin of the American Meteorological Society*, 69(11), pp.1328-1347.

Wolfson, M.M. and Iacono, M.J., (1987). A Comparison of PAM-II (Portable Automated Mesonet) and FLOWS (Federal Aviation Administration Lincoln Laboratory Operational Weather Studies) Mesonet Data during COHMEX (Cooperative Huntsville Meteorological Experiment). *MIT Lincoln Laboratory Report*

Wolfson, M.M., DiStefano, J.T. and Forman, B.E., (1987). The FLOWS (FAA-Lincoln Laboratory Operational Weather Studies) Automatic Weather Station Network in Operation. *MIT Lincoln Laboratory Report*, pp. 1-267.

Wolfson, M.M., DiStefano, J.T. and Fujita, T.T., (1985). Low-altitude wind shear in the Memphis, TN area based on Mesonet and LLWAS data. In: Preprints of the 14th Conference on Severe Local Storms, American Meteorological Society, Indianapolis.

Wolfson, M. M., (1988). Characteristics of microbursts in the continental United States. *The Lincoln Laboratory Journal*, 1, pp. 49–74.

Wood, G. S., Kwok, K. C., Motteram, N. A., & Fletcher, D. F. (2001). Physical and numerical modelling of thunderstorm downbursts. *Journal of Wind Engineering and Industrial Aerodynamics*, 89(6), 535-552.

[www.britannica.com/science/downburst](http://www.britannica.com/science/downburst) accessed on 10<sup>th</sup> October 2019.

[www.britannica.com/science/troposphere](http://www.britannica.com/science/troposphere) accessed on 16<sup>th</sup> December 2019.

[www.weather.gov/jetstream/wind\\_damage](http://www.weather.gov/jetstream/wind_damage) accessed on 12<sup>th</sup> October 2019.

[www.windalliance.org.au/south\\_australia\\_blackouts\\_the\\_facts](http://www.windalliance.org.au/south_australia_blackouts_the_facts) accessed December 2019.

Xu, Z. and Hangan, H., 2008. Scale, boundary and inlet condition effects on impinging jets. *Journal of Wind Engineering and Industrial Aerodynamics*, 96(12), pp.2383-2402.

Zhang, Y., Hu, H., & Sarkar, P. P. (2013). Modeling of microburst outflows using impinging jet and cooling source approaches and their comparison. *Engineering structures*, 56, 779-793.

## Appendices

### Appendix A: Design of ABL simulation

The governing parameters of flow over a roughness element are the height of obstacles, displacement height, wall shear stress, and flow velocity. As the fluid flow progresses over a surface a boundary layer is formed over the surface due to the no slip condition. In the case of the roughness elements, a smooth surface prevails when the roughness elements are submerged into the viscous sublayer (Cebeci, 2012). Certainly, when the roughness elements are considerably larger in height than the thickness of the viscous sublayer the flow experiences the effect of the roughness elements and the flow tends to produce turbulence due to the wake vortices produced by the separation at the backside of the roughness element. The transition to turbulent flow due to introduction of the roughness elements depends on the flow velocity, height of the roughness elements, roughness length ( $z_0$ ), distribution of the roughness elements, and Roughness Reynold's number. The height of the roughness elements is designed based on the highest pump flowrate setting for the flume to ensure transition to turbulent boundary layer by achieving the highest  $Re_k$  for a selected roughness element. From the smooth wall flume boundary layer experiments of Babaei (2018) the following parameters shown in table (A-1) can be calculated from the Blasius approximation for a smooth wall boundary layer.

**Table A1 Flow parameters for smooth wall flow over hydraulic flume (Babaei, 2018)**

<b>Pump flow rate, <math>Q_p(L/s)</math></b>	19.10
<b>Free-stream velocity <math>U_a(cm/s)</math></b>	6.42
<b><math>Re_{x@1.9m} = \frac{U_a x}{\nu}</math></b>	$1.21 \times 10^5$
<b>Skin friction coefficient, <math>C_f = \frac{0.664}{(Re_x)^{\frac{1}{2}}}</math> (White,1979)</b>	0.002
<b>Friction velocity, <math>u_*(cm/s)</math></b>	0.22

The non-dimensional parameters defining the transition to turbulent flow for  $k$  as the height of the roughness elements are defined as below:

$$Re_* = \frac{ku_*}{\nu} \quad (A1)$$

$$Re_k = \frac{ku_k}{\nu} \quad (A2)$$

Table (2) includes details on these above-mentioned criteria used by various studies and includes the proposed heights of the roughness elements approximated by implementing the corresponding criterions to the measurements from the smooth wall boundary layer case. Basically, these Roughness Reynolds numbers represent minimum non-dimensional wall normal distances to ensure higher to avoid the roughness elements extend beyond the viscous sublayer of the boundary layer.

**Table A-2 Proposed height of roughness elements**

<b>Literature</b>	<b>Criterion for Reynolds number for turbulent flow</b>	<b>Proposed height of roughness element <math>k(cm)</math></b>
Fage & Preston (1941)	$Re_k > 400$	1.17
Van Driest (1956)	$Re_* > 60$	3.23
Djenidi et. al. (1999)	$Re_* > 124$	6.68
Grass (1971)	$Re_* > 84.7$	4.56

Referring to table (A-2) the smallest height for the roughness element satisfying the criterion for the turbulent flow is selected due its feasibility in experiments for forming an array. Zinc plated 9/16-12 Hexagonal Nuts were used having a height of 1.2 cm. To initially trigger the flow at the inlet of the flume a wall barrier (fence) having the height of 4.5 cm was placed at 18 cm from the flume inlet. Moreover, turbulence generators in the shape of spires were made with a height of 14 cm and width of 5 cm. The standard half-width spire design constitutes the width of the spire as half the spire's height (Standen, 1972). However, for the present study the width of the spire was kept 5 cm for a spire height of 14 cm. Moreover, for generating an array of spires (14 spires) the spacing between the center of spires was kept 7 cm and the row of spires was placed 18 cm downstream from the fence. The above-mentioned method is an approximation to decide on the design of the roughness elements, spires, and the wall barrier. However, the optimization of this design for generating ABL flow within the flume was beyond the scope of present study. Nevertheless, the validity of this technique to generate ABL flow is checked in Chapter 4 (Section 4.1).



## Appendix B: ABL experiments: Convergence of statistics, velocity vector fields, Boundary layer profile

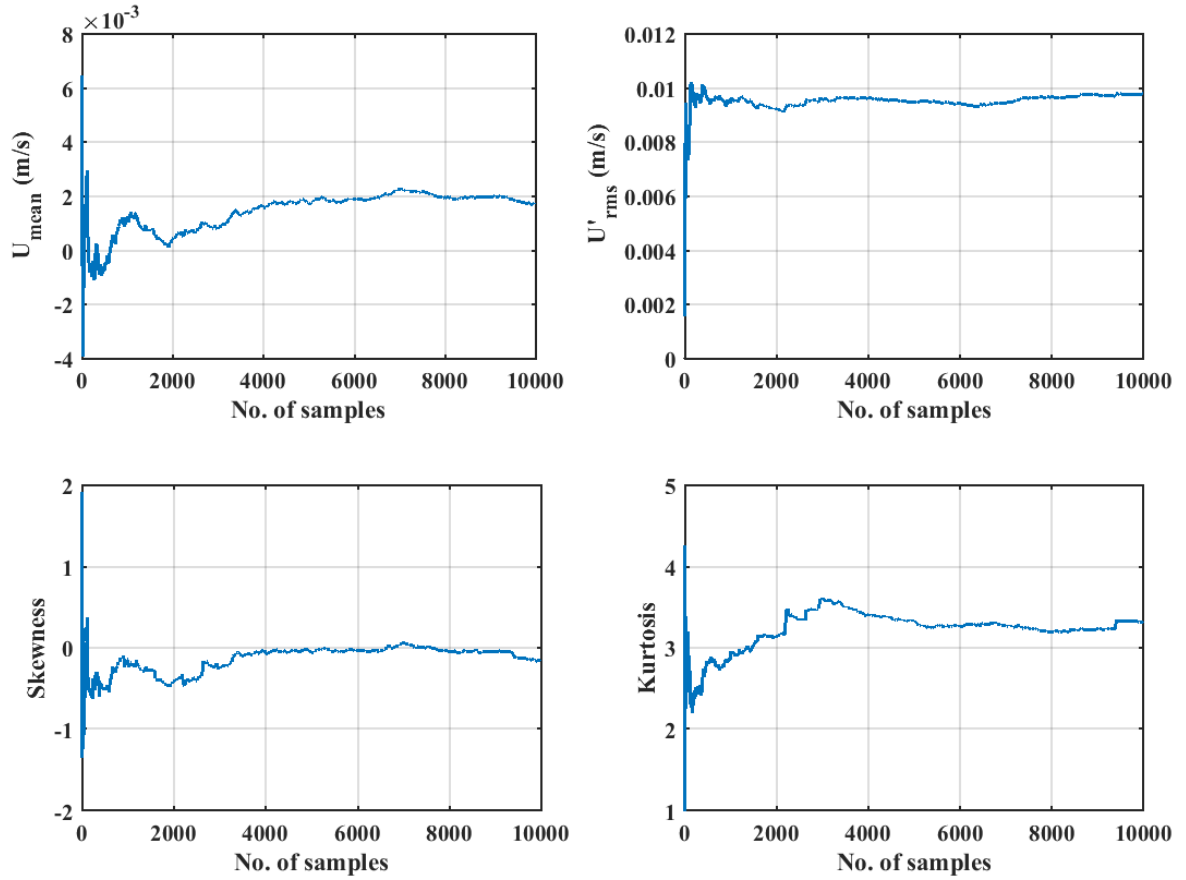


**Figure B1:** statistical convergence about a single point in the measurement domain

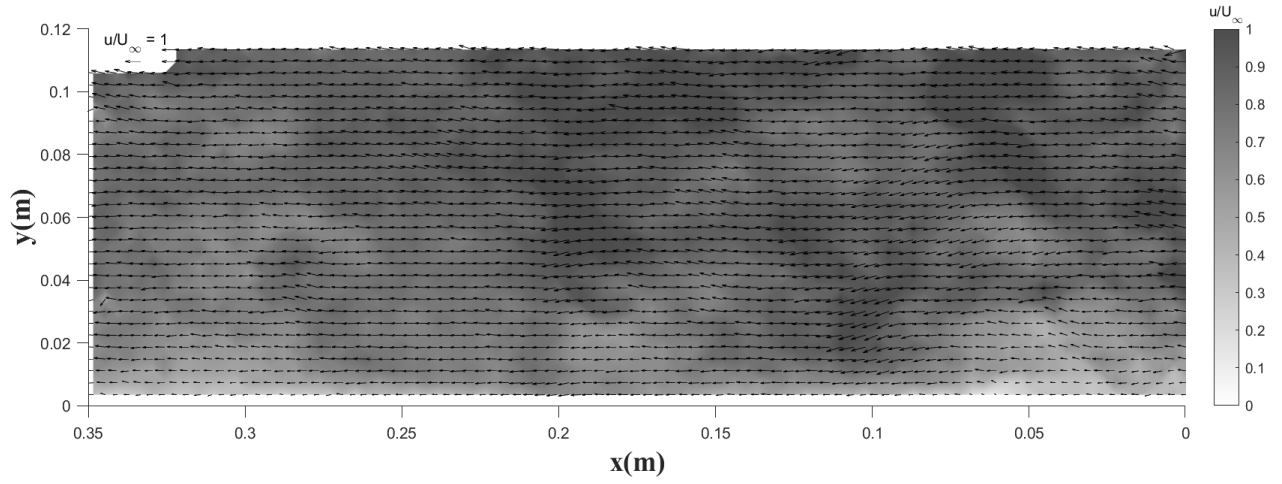


**Figure B2: Normalized instantaneous velocity vector field for the ABL flows for R-B**

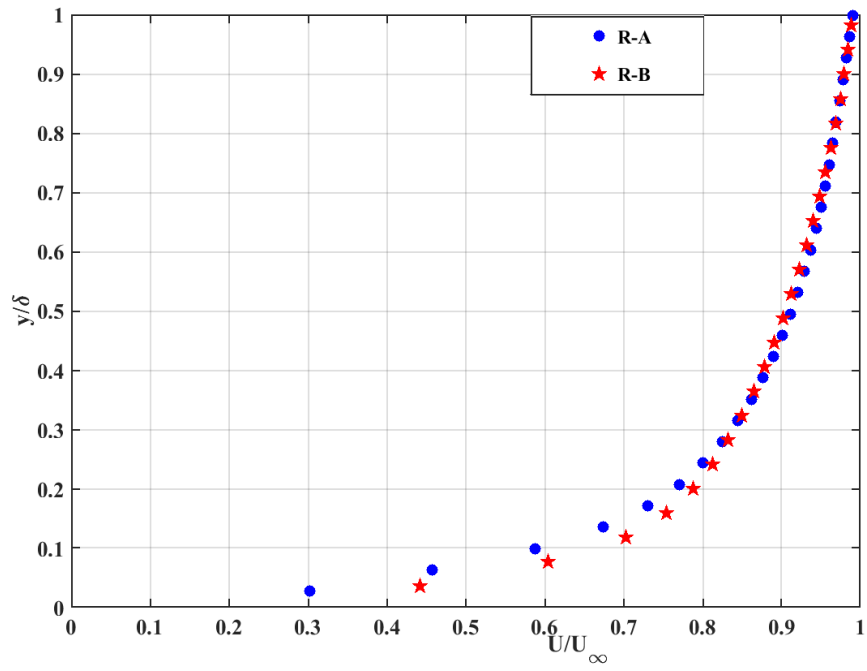


**Figure B3: Normalized velocity profiles for the ABL flows**

## Appendix C: Experimental uncertainty

The uncertainty associated with the usage of *PIV* experimental technique is computed in this section. The detailed procedure for computing the uncertainty considering various error sources such as velocity gradient bias, out-of-plane motion, peak locking, and error associated with interpolation is discussed in Graat (2020) and Khadivi (2012). The bias (mean) and random (rms) gradient errors and the interpolation errors are extracted from Thielicke (2014) for a seeding particle diameter of 3 pixels in the *PIV* images collected. The uncertainty was computed for the maximum observed velocities i.e., peak radial velocity for the downburst experiments, and free-stream velocity for the ABL experiments.

Error Sources	ABL experiments		Translating downburst events	
	Bias	Random	Bias	Random
Gradient error (pixels)	0	0.020	0.020	0.011
Interpolation error (pixels)	0.080		0.080	
Out of plane motion	0		0	
Total error (pixels)	$\pm 0.080$	$\pm 0.020$	$\pm 0.083$	$\pm 0.011$
Total error ( <i>cm/s</i> )	$\pm 0.16$	$\pm 0.039$	$\pm 1.36$	$\pm 0.183$
Absolute Error	$\pm 2.36\%$	$\pm 0.58\%$	$\pm 4.99\%$	$\pm 0.67\%$

## Appendix D: Extraction of roughness parameters by fitting log-law to velocity profiles:

The log-law equation (D1) can be modified in the following form:

$$u = \frac{u_*}{k} \ln(y - d_0) - \frac{u_*}{k} \ln(z_0) \quad (\text{D1})$$

The linear representation for  $u$  vs.  $\ln(y - d_0)$  plot is evident for neutral boundary layers in atmosphere (Stull, 1988). Hence, the displacement height ( $d_0$ ) in the above equation is determined by selecting a suitable value from  $0 - h_r$  (i.e. distance from ground to height of roughness element) which gives the best linear representation for  $u$  vs.  $\ln(y - d_0)$  plot. Thereafter, upon substituting the chosen value of  $d_0$  in the log-law equation the fitting variables  $u_*$  and  $z_0$  can be extracted from the slope  $\left(\frac{u_*}{k}\right)$  and intercept  $\left(\frac{u_*}{k} \ln(z_0)\right)$  of the linear curve (figure D-1).

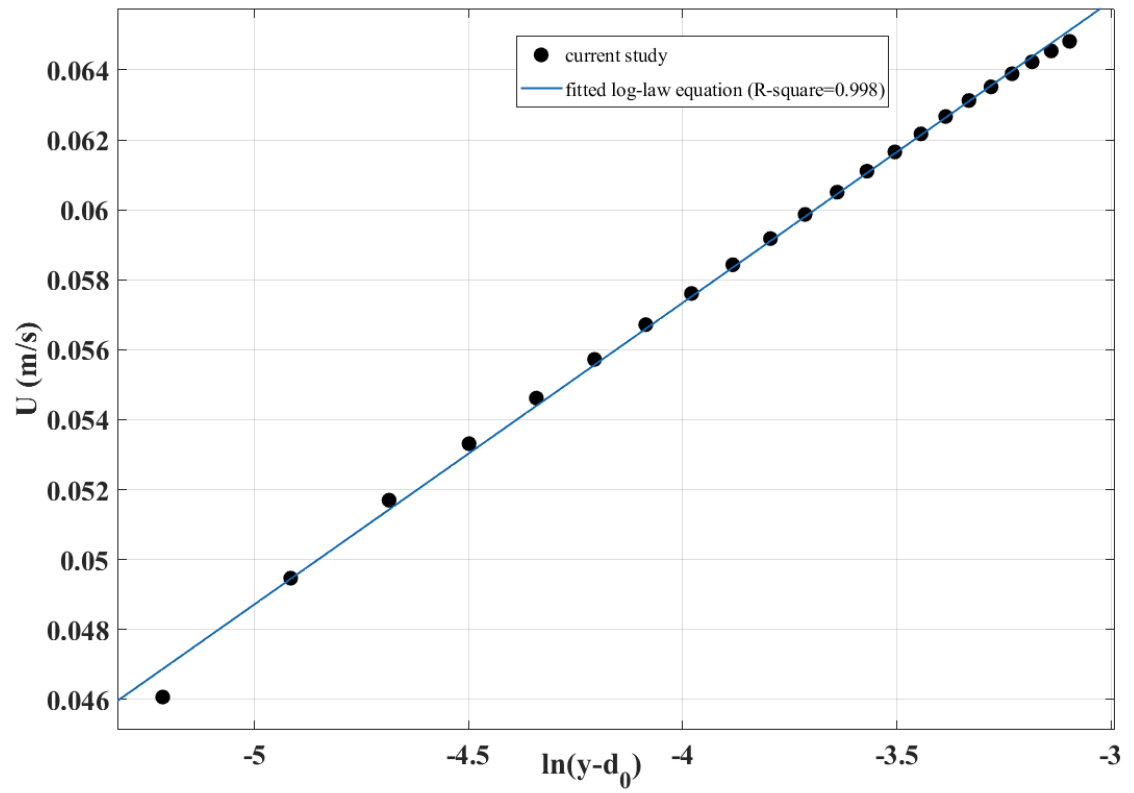


**Figure D-1: Log-linear representation of the spatially averaged velocity plotted to fit the log-law equation**

## Appendix E: Downburst experiments: Comparison of boundary layer before downburst event, Repeatability of the outflows

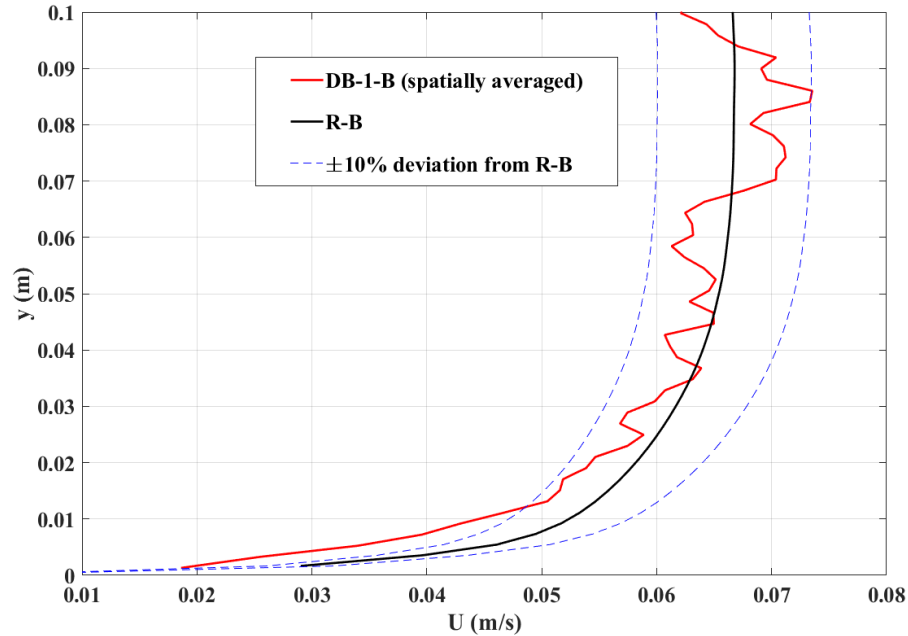


**Figure E-1: Comparison of the velocity profile for the boundary layer experiments with boundary layer prevailing before downburst event at  $t = -0.7s$**

### Repeatability of the translating downburst experiments:

The radial and vertical propagation for a stationary downburst outflow was found to be repeatable (Babaei *et al.*, 2021). With the present work the velocity timeseries (at a fixed spatial location) for two repeated runs display that the profiles are always within 25% of the ensembled mean with an averaging window of 0.3 s, and hence repeatable (figure E-2). With this it is also found that the trajectories of the vortex cores are repeatable, and hence the only the vortex trajectories containing a significant number of points for its tracking is used for discussions in section 4.2.2.

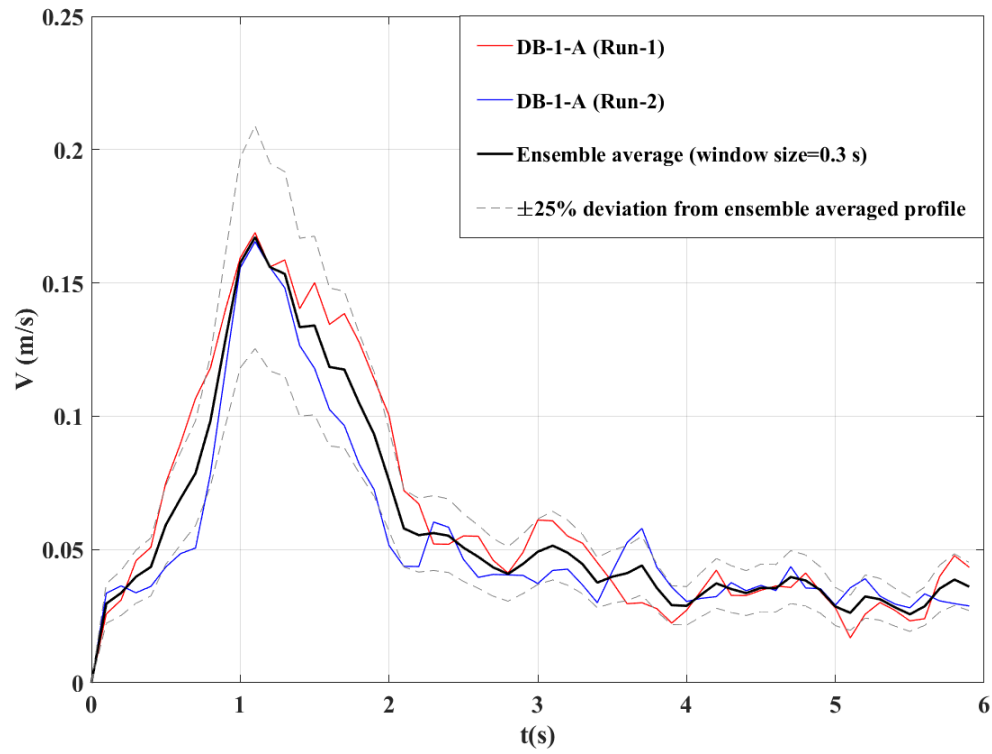


**Figure E-1: Comparison of the velocity timeseries for two repetitions about the ensemble average**

## Curriculum Vitae

<b>Name:</b>	Shivani Ashitkumar Jariwala
<b>Post-secondary Education and Degrees:</b>	<p>The University of Western Ontario London, Ontario, Canada 2017-2021 <i>Master of Engineering Science (Mechanical &amp; Materials Engineering- Thermofluids)</i></p> <p>Gujarat Technological University Gujarat, India 2013-2017 <i>Bachelor of Engineering (Mechanical Engineering)</i></p>
<b>Honors and Awards:</b>	Western Engineering Scholarship 2018-2019
<b>Related Work Experience</b>	<p>Teaching Assistant The University of Western Ontario 2018-2019</p> <p>Research Assistant The University of Western Ontario 2018-2021</p>